

# **JOINT INVERSION OF SATELLITE GRAVITY AND SEISMIC SURFACE WAVE DATA: A SYNTHETIC TEST AND ITS APPLICATION FOR BOTSWANA CRUST AND UPPER MOST MANTLE VELOCITY AND DENSITY MODELING**

GETNET AYALEW ASSEFA

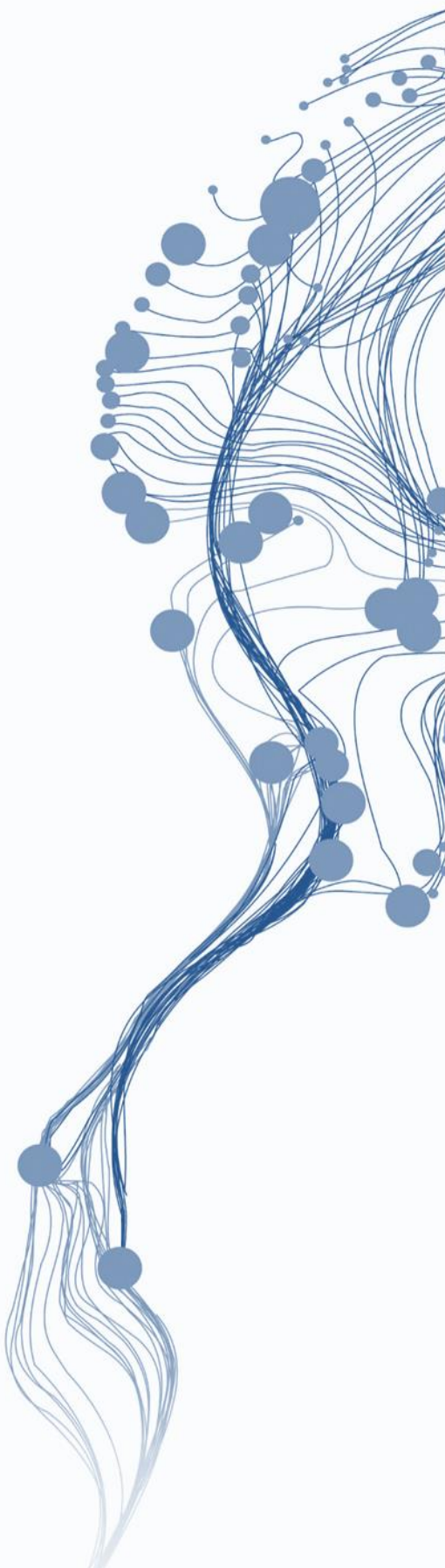
August 2022

SUPERVISORS:

Dr. Islam Fadel

Prof, Dr. Mark Van der Meijde





# **JOINT INVERSION OF SATELLITE GRAVITY AND SEISMIC SURFACE WAVE DATA: A SYNTHETIC TEST AND ITS APPLICATION FOR BOTSWANA CRUST AND UPPER MOST MANTLE VELOCITY AND DENSITY MODELING**

GETNET AYALEW ASSEFA

Enschede, The Netherlands, August 2022

Thesis submitted to the Faculty of Geo-Information Science and Earth Observation of the University of Twente in partial fulfilment of the requirements for the degree of Master of Science in Geo-information Science and Earth Observation.

Specialization: Applied Remote Sensing for Earth Sciences

## **SUPERVISORS:**

Dr. Islam Fadel  
Prof, Dr. Mark Van der Meijde

## **THESIS ASSESSMENT BOARD:**

Dr. Harald Van der Werff (Chair)  
Prof, Dr. Christine Thomas (external examiner,  
University of Muenster, Germany)  
Dr. Arjan Dijkstra (examiner)

#### DISCLAIMER

This document describes work undertaken as part of a programme of study at the Faculty of Geo-Information Science and Earth Observation of the University of Twente. All views and opinions expressed therein remain the sole responsibility of the author, and do not necessarily represent those of the Faculty.

# ABSTRACT

The joint inversion of geophysical observations has recently become an active research area to characterize the subsurface's physical properties. They are defined as the simultaneous optimization of two or more objective functions to estimate a model that describes all data sets simultaneously. Due to the constrained optimization of the subsurface model from different independent data sets, joint inversion can help to reduce the intrinsic non-uniqueness of the geophysical inverse problem. As a result, by merging different geophysical methods into a single inversion scheme, joint inversion approaches aim to reduce the number of acceptable models that fits different data set. Therefore, recently with the widespread geophysical data set available, it has become a topic of widespread active research area in large-scale lithospheric modelling or small-scale exploration studies by integrating different geophysical data sets in a joint inversion scheme.

In this research, a new methodology developed by Fadel. (2018) that efficiently integrates gravity field and its gradients with seismic surface wave data is tested and implemented for real data. The new methodology is based on parallel versions of the tesseroid forward solver for the gravity total field, and the 6-gradient components, and 3D surface wave dispersion forward solver. The Levenberg–Marquardt damped least-squares method is used for the joint inversion of the multiple data components to retrieve the directly-coupled shear-wave velocity and density structure of the subsurface using Brochure velocity-density relationships. However, the required computational cost of the approach was the main drawback of the method to apply for large scale regional modeling. That was due to the approximation of the Jacobian for the surface wave forward solver iterating through each cell of the 3D cube. Therefore, recent improvements were introduced to the method efficiency to approximate the Jacobian based on a 1D algorithm that operates over the 2D grid of the 3D model, which significantly improves the computational cost of the method. In this research, the new developments were first tested using two phases of synthetic regional case studies and then followed by real data application to test the method on a real case study and to improve our knowledge about the tectonics of Botswana.

The synthetic tests were conducted in three different scenarios of data integration to understand the added values of each data to the inversion. The results from the two phases of the synthetic tests prove that the performance of the method in terms of computational cost is greatly improved by approximately 80 % after improvements and show that shear wave velocity and density are retrieved accurately when the two data sets are integrated than the surface wave only and gravity only inversion, respectively. Furthermore, the added value of the unique GOCE gradient data for subsurface density modelling is analysed. As expected, the results suggest that the GOCE gravity gradients have added value to improve the resolving power of the inversion, especially for crustal to uppermost mantle depth ranges. After that depth range, it does not show an added value in the retrieved density and velocity model. Finally, the joint inversion approach is applied using real data measurements of gravity and seismic surface wave data to study the crust and upper mantle velocity and density structure of Botswana. The results of the real data case study highlight the limitations of the method and also show the first joint inversion velocity and density structure of Botswana which can be significantly improved in future studies.

Keywords: GOCE gravity gradients; seismic surface waves; least-squares optimization; geophysical inversion; joint inversion.

## ACKNOWLEDGEMENTS

First, I would like to thank the almighty “Allah” for the countless blessing, keeping me strong and healthy to finish this work.

I would also like to send my humble gratitude to the Netherlands government, the OKP scholarships program, and the Faculty of ITC for providing me with this life-changing opportunity to do my master’s degree here in the Netherlands. Because of this opportunity, I got the chance to meet amazing people worldwide whom I now call friends and supportive teachers.

I want to thank my supervisors Dr. Islam Fadel and Prof. Dr. Mark Van Meijed, for their endless support, patience, advice, feedback, and critical questions that helped me to understand and shape my research. Islam, thank you so much for believing in me from the beginning of this research, even when I couldn't believe in myself. Thank you for your patience and weekly meetings in developing and updating the code to make it work for the final implementation. It helped me acquire new technical skills in python programming and the development of an inversion scheme. Thank you for the unconditional effort you made for the completion of the thesis. You were there every step of the way, not only thesis related but even in my personal issues. I am humbled. Thank you. Mark, thank you so much for the critical decision you made on my thesis every time something seems to go wrong, or I am stuck, you always find a way to solve them. Your critical comments, quick response, and review of my thesis helped me a lot to finish this thesis. Thank you for the time we spent together to discuss even my personal circumstances.

My special thanks goes to Dr. Harald, my mentor. You were always there from the beginning of my master's program here at the ITC. I remain grateful for the continuous checkups on my course progress and thesis. I am truly grateful for your kindness, your support during my thesis, and that very welcoming smile of yours.

I would like to thank my external examiner, Prof, Dr. Christine Thomas for the critical question and lively discussions we had during my Défense, I really enjoyed the questions, thank you. Dr. Arjan (examiner), thank you for the appreciation and your time for the last talk we had at the end. I really appreciate it.

My gratitude also goes to Dr. Bio, Junior, and Stephen, for the discussion we had. I loved our time together and appreciate your help when I needed it. I would also like to thank prof. Dr. Jordi Julia, for following up on my internship even in an unusual virtual setup of weekly progress meetings. I remain grateful.

This work wouldn't have been complete without the availability of highly used computing resources from the ESA department. To this end, I would like to thank the ESA department for providing me with access to their computer machine.

My ITC friend, I cannot mention all of your names, but I am deeply grateful for all the support and great friendship we had over the years. If it wasn't for our friendship, I could only imagine what living miles away from home would be like. I really appreciated our time.

Finally, I would like to thank my family, who did everything for me to get into this position and have always been there for me when I needed them the most. Mom and Dad, all the love, support, motivation, and prayers have helped me. I am here because of you, and I am grateful to be yours.

The contribution and outcomes of this work would not have been possible without the constant guidance, support, and encouragement of all the people I mentioned above. After my time at ITC, I am sure this will continue to be a source of inspiration, motivation, and, most of all, a guide to my future.

# TABLE OF CONTENTS

---

## Contents

<b>1. Introduction</b>	<b>1</b>
1.1. Background	1
1.2. Problem statement	4
1.3. Research Objectives	4
1.3.1. Main Objectives	4
1.3.2. Sub-Objectives and Questions	4
1.4. Thesis Structure	5
<b>2. Study area and data set</b>	<b>6</b>
2.1. Study Area	6
2.1.1. Cratons	6
2.1.2. Mobile Belts	7
2.1.3. Nosop and Passarge Basins	9
2.2. Data set	9
2.2.1. Gravity data	9
2.2.2. Surface wave data	10
<b>3. Methodology</b>	<b>12</b>
3.1. Joint Inversion Method	12
3.1.1. Forward Solver and Sensitivity Kernel	12
3.1.2. Inversion Formulation	15
3.2. Joint Inversion Testing and Implementation	16
3.2.1. First Phase: Simple geologic model synthetic test	16
3.2.2. Second Phase: Complex geologic model synthetic test	17
3.2.3. Third Phase: Real data application of the joint inversion approach	17
3.2.4. Parameter Estimation	17
3.2.5. Model Visualization and Assessment	18
<b>4. Synthetic method test using a simple geologic model</b>	<b>19</b>
4.1. Introduction	19
4.2. Synthetic Model Design for Joint Inversion Implementation	19
4.2.1. Model Setup	19
4.2.2. Synthetic Data Forward Modelling (Data set)	21
4.3. Inversion Result	23
4.3.1. Scenario 1: Gravity-only inversion	24
4.3.2. Scenario 2: Surface wave-only inversion	24
4.3.3. Scenario 3: Joint inversion of Rayleigh wave group and phase velocity with the gravity measurements	26
4.4. Discussion	28
4.4.1. Evaluation of the Inversion Results	28
4.4.2. Model Misfit Analysis	29
4.4.3. Data Misfit Analysis	32
4.4.4. Method Performance Evaluation	34
<b>5. Synthetic complex model mimicking botswana geology</b>	<b>36</b>

5.1.	Introduction .....	36
5.2.	Model Setup.....	36
5.3.	Forward Modelling Results (Data sets) .....	38
5.3.1.	Gravity Data .....	38
5.3.2.	Surface Wave Data .....	39
5.4.	Inversion .....	41
5.5.	Result and Discussion.....	41
5.5.1.	Recovered density model.....	42
5.5.2.	Recovered velocity model .....	45
5.5.3.	Model misfit analysis .....	47
5.5.4.	Data misfit analysis.....	48
<b>6.</b>	<b>Real data applications.....</b>	<b>49</b>
6.1.	Data sets.....	49
6.2.	Surface wave Group and Phase velocity Dispersion Sensitivity Analysis .....	49
6.3.	3-D Joint inversion of surface wave and gravity data .....	50
6.3.1.	Model discretization .....	50
6.3.2.	3D inversion .....	51
6.4.	Result and Discussion.....	52
6.4.1.	Overview of the 3D velocity and density model of Botswana.....	52
6.4.2.	Sedimentary Basins.....	55
6.4.3.	Malatahohe Micro-Craton (MC) .....	56
6.4.4.	ORZ and the Extension of EARS in Central Botswana and its Relationship with the Epicenter of the 2017 April 3 <sup>rd</sup> 6.5 Mw Earthquake.....	57
6.4.5.	Bushveld Complex and Colesberg Magnetic Lineament.....	58
6.5.	Data misfit .....	58
<b>7.</b>	<b>Conclusions and recommendation .....</b>	<b>60</b>
7.1.	Conclusions .....	60
7.2.	Recommendations .....	62

## LIST OF FIGURES

---

Figure 1.1 Topographic map of Africa showing the location of Botswana outlined by its boundaries in southern Africa. The African Superswell in the southern Africa region, the east and west branches of EARS and Lake Kariba which is expected to be the last surface expression of the EARS are indicated by black arrows. ....	2
Figure 2.1: The tectonic map of Southern Africa with the outline of Botswana boundary at the center from Leseane et al. (2015) showing the Archean Cratons, orogenic Belts, and Sedimentary basins.....	6
Figure 2.2: The Precambrian tectonic map of Botswana from Leseane et al. (2015) that shows the Archean Cratons, Proterozoic orogenic Belts, and Sedimentary basins. The Okavango Rift Zone has a fault system shown by the white lines in the northwest of the map that trend in the northeast direction. The broken orange line indicates the kalahari sutue zones.....	7
Figure 2.3: Free air gravity data of Botswana area overlain by the tectonic units of Botswana. CC= Congo Craton; DB= Damara Belt; GCB= Ganzi-Chobe-Belt, PB= Passarge Basin, OB= Okwa Block, NB= Nosop Basin, KB= Kheis Belt; KC= Kalahari Craton, MB= Magondi Belt; LB= Limpopo Belt; ZC= Zimbabwe Craton. The white line boundary at the nothwestern part indictes the ORZ.....	9
Figure 2.4: The six-component gravity gradient data from GOCE satellite gravity data (a - f). with the tectonic boundaries on the top. CC= Congo Craton; DB= Damara Belt; GCB= Ganzi-Chobe-Belt, PB= Passarge Basin, OB= Okwa Block, NB= Nosop Basin, KB= Kheis Belt; KC= Kalahari Craton, MB= Magondi Belt; LB= Limpopo Belt; ZC= Zimbabwe Craton. The white line boundary at the nothwestern part indictes the ORZ. ....	10
Figure 3.1: The joint inversion scheme flow chart.....	12
Figure 3.2: The 3D mesh of the Earth Tesseroid model (a) and the resulting 3D mesh of the calculated group and phase velocities (b). The i, j, and k index are used to indicate the number of discrete steps each 1D depth model has, The number of 1D dispersion curve observation periods, and the number of 2D grid points, respectively. ....	14
Figure 3.3: The performance of the Tesseroids (A) and Rayleigh wave forward solver (B) using 1,2,4,8,16, and 32 processors. The analysis was done on Dell Tower 7910 machine with 196 GB RAM and 48 Xeon Gold 3.2GHz processors.....	15
Figure 4.1: Average 1D interpolated velocity from the global Ak135 reference velocity model (Kennett et al., 1995) were used to construct the 3D starting model for the synthetic method test. ....	19
Figure 4.2: Starting model used for the inversion. The Plot shows the interpolated depth slice at 17.5 km depth velocity model from the global AK135 and the cross-section along the profile lines A-A' & B-B'..	20
Figure 4.3: The true synthetic shear wave velocity, density, and density contrast model used to generate the synthetic data. (a), (b), and (c) shows velocity, density, and density anomaly depth maps at 12.5 km with positive and negative anomalies in the middle with the corresponding cross-sections along the profile line of A-A'.....	21
Figure 4.4: Random noise-contaminated gravity signal calculated at satellite altitude of 225 km from the true model density contrast shown in Figure 4.3, c. The gravity component includes the vertical gravity field (a) and the other six-component gradient data (b-g).....	22
Figure 4.5: The Rayleigh wave group (a) and phase velocity dispersion (b) at 17.5 s period with added random noise to simulate a real case scenario. The Profile lines A-A' depict the corresponding cross-section that shows the period extent of the dispersion curve up to 50 s periods.....	23
Figure 4.6: The calculated contaminated average group and phase velocity dispersion curves (a) of the 1D shear wave velocity of the true model (b) and its sensitivity analysis at 5, 10, 20, 30 & 45 s intervals, which	

demonstrates the depth that can be sampled by group and phase velocity up to 50 km and beyond (c and d, respectively).....23

Figure 4.7: Depth slice at 17.5 km and cross-section plot along profile lines A-A' of the retrieved density model from scenario-1 of gravity-only inversion. (a) vertical gravity field ( $g_z$ ) only inversion result, (b) joint inversion of the six components second order gradient data inversion result, (c) joint inversion of the  $g_z$  and second order vertical component gradient ( $g_{zz}$ ) data inversion result, and (d) joint inversion of  $g_z$  and all the six components gradient data inversion result.....25

Figure 4.8: The retrieved velocity model obtained after the inversion of the surface wave only Rayleigh group and phase velocity dispersion data with the corresponding 2D profile along lines A-A'.....26

Figure 4.9: Inverted velocity (a) and density (b) model from the inversion of Rayleigh wave group and phase velocity dispersion with the vertical gravity field data ( $g_z$ ). The plot shows the recovered velocity (a) and density (b) model with the corresponding cross-section along lines A-A' for each plot.....27

Figure 4.10: Inverted velocity and density model from the joint inversion of the Rayleigh group, and phase velocity dispersion data and all the gravity components ( $g_z + g_{all}$ ), The plot shows the recovered velocity (a) and density (b) model with the corresponding cross-section along lines A-A' for each plot.....27

Figure 4.11: Comparison of the density model obtained from the inversion of  $g_z$  only (a)  $g_z + g_{all}$  (b), surface wave +  $g_z$  (c), and surface wave +  $g_z + g_{all}$  (d). The black rectangle plotted on the image shows the boundary of the anomaly shown in the true model. Therefore, as it is shown from left to right (a to d), the inversion result improves retrieving the anomaly's shape and amplitude when we combine both data sets. ....30

Figure 4.12: The retrieved velocity model obtained from surface wave only inversion (a), joint inversion of surface wave and  $g_z$  gravity data (b) and joint inversion of surface wave and all gravity data ( $g_z + g_{all}$ ) data. ....31

Figure 4.13: Joint inversion approach computational cost evaluation before (a) and after (b) method improvement. ....35

Figure 5.1: Interpolated 1d velocity model based on AK135 reference global model (Kennett et al., 1995). ....36

Figure 5.2: The depth slice plot of the 3D true velocity and coupled density model mimicking Botswana's geology at 7.5 (a & b) and 112.5 km depth (c & d), respectively. The different geological units such as the Nosop and Passarge sedimentary basin (NB & PB), buried Micro-craton (MC), Congo craton (CC), the Kalahari craton (KC), the Okavango rift zone (ORZ), and the EARS extension (ER), are depicted as a homogeneous block from the background values. Note that each map of the depth slice plot has a different color scale to help keeping the images' details. ....37

Figure 5.3: A 2D cross-section of the true velocity (a) and coupled density model (b) mimicking Botswana's geology along the A-A' and B-B' east-west cross section lines shown in Figure 5.2's depth slices plot. The different geological units, such as the Nosop and Passarge sedimentary basins (NB & PB), the buried Micro-craton (MC), the Congo craton (CC), the Kalahari craton (KC), the Okavango rift zone (ORZ), and the EARS extension (ER), are depicted as a homogeneous block from the background values. ....38

Figure 5.4: Random noise-contaminated gravity signal calculated at a satellite altitude of 225 km from the density contrast model shown in Figure 7.15, Appendix 2. The gravity component includes the vertical gravity field (a) and the other six-components gradient data (b-g), and the color scale indicates the high and low values of the gravity signals for each component.....39

Figure 5.5: Random noise-contaminated Rayleigh wave group (A) and Phase (B) velocity at 7.5, and 112.5 s calculated from the synthetic model shown in Figure 5.3. A-A' & B-B' cross-sections show the group and phase velocity measurements calculated for the same locations as in the depths slice subplot. ....40

Figure 5.6: The calculated average group and phase velocity dispersion curves over period 3-120s after noise contamination (a). (b) shows the global shear wave velocity model interpolated from AK135 (Kennett et al.,

1995) which is used as a reference model., as well as the sensitivity analysis of the group and phase velocity period used, which demonstrates that the group and phase velocity up to 120s can depths up to 200 km (c and d, respectively).....	41
Figure 5.7: Shallow (7.5 km) and deep (112.5 km) density model depth slice plot of the true density (a & b), recovered density model from gravity data only inversion (c & d), and recovered density model from the joint inversion of gravity and surface wave data (e & f). Each map has a distinct color scale to preserve features. ....	44
Figure 5.8: A 2D cross-section of the true density (a) and recovered density models (b and c) along A-A' and B-B' east-west cross-section lines highlighted in the depth slices in Figure 5.7. The different geological units are highlighted, such as the Nosop and Passarge sedimentary basins (NB & PB), the buried Micro-craton (MC), the Congo craton (CC), the Kalahari craton (KC), the Okavango rift zone (ORZ), and the EARS extension (ER). ....	45
Figure 5.9: Shallow (7.5 km) and deep (112.5 km) velocity model depth slice plot of the true velocity (a & b), recovered velocity model from surface wave data only inversion (c & d), and recovered velocity model from the joint inversion of gravity and surface wave data (e and f), respectively. Note each image has a different color scheme per depth slice. ....	46
Figure 5.10: A 2D cross-section of the true density (A) and recovered density models (B and C) along A-A' and B-B' east-west cross-section lines. The different geological units are highlighted, such as the Nosop and Passarge sedimentary basins (NB & PB), the buried Micro-craton (MC), the Congo craton (cc), the Kalahari craton (KC), the Okavango rift zone (ORZ), and the East African Rift system (ER).....	47
Figure 6.1: The average group and phase velocity dispersion curve of Botswana (a), and the corresponding sensitivity analysis of the group and phase velocity periods (b and c). The average 1D shear wave velocity model shown in Figure 6.2 is used as a reference model for the sensitivity analysis.....	50
Figure 6.2: Interpolated average 1D vs model of Botswana from Fadel et al., 2020 shear wave velocity model. ....	51
Figure 6.3: Plane view of the absolute shear wave velocity model depth slices at 5, 30, 60, 100, 120, 140, 160, and 200 km depths. NB = Nosop Basin; PB = Passarge Basin; KC = Kalahari Craton; ORZ=Okavango Rift Zone; ZC = Zimbabwe Craton; ER = East African Rift System; CML = Colesberg Magnetic Lineament. ....	53
Figure 6.4: Plane view of the density contrast model depth slices at 5, 30, 60, 100, 120, 140, 160, and 200 km depths. NB = Nosop Basin; PB = Passarge Basin; KC = Kalahari Craton; ORZ=Okavango Rift Zone; ZC = Zimbabwe Craton; ER = East African Rift System; CML = Colesberg Magnetic Lineament. ....	54
Figure 6.5: The 3D shear wave velocity model of Botswana. The location of the cross-section line is indicated in plot c. The location of the 3 April 2017 earthquake is indicated on the depth slice map. The shear wave velocity model shown here are the velocity contrast for crustal and upper mantle part. The green circle at A-A' shows the expected location of ORZ and surface expression of the EARS. The red circle shows at B-B' shows a low velocity anomaly seen at the Nosop basin. The orange circle shows the expected location of the MC craton. However, the depth extent is not clearly resolved. The red star indicates the location of the 2017, 3rd April earthquake epicentre. NB = Nosop Basin; PB = Passarge Basin; KC = Kalahari Craton; ORZ=Okavango Rift Zone; ZC = Zimbabwe Craton; LB = Limpopo Belt; ER = East African Rift System; CML = Colesberg Magnetic Lineament. ....	55
Figure 6.6: The 3D density contrast model of Botswana. The location of the cross-section line is indicated in plot c. The density contrast model shown here are the density contrast model plotted for crustal and upper mantle. The green circle at A-A' shows the expected location of ORZ and surface expression of the EARS. The red circle shows at B-B' shows a low velocity anomaly seen at the Nosop basin. The orange circle shows the expected location of the MC craton. However, the depth extent is not clearly resolved. The	

red star indicates the location of the 2017, 3rd April earthquake epicentre. NB = Nosop Basin; PB = Passarge Basin; KC = Kalahari Craton; ORZ=Okavango Rift Zone; ZC = Zimbabwe Craton; LB = Limpopo Belt; ER = East African Rift System; CML = Colesberg Magnetic Lineament.....56

Figure 7.1: Starting model used for the inversion. Plot (a) shows the interpolated velocity model from the global AK135 with the cross-section along the profile lines A-A' and B-B'. Plot (a) shows the derived density model from the velocity model using the Brocher relation of density and velocity with the corresponding cross-section of lines A-A' and B-B'. .....71

Figure 7.2: Depth slice plot of the density contrast model at a 17.5 km and its 2d cross section along line A-A' and B-B'. .....72

Figure 7.3: RMSE per depth plot of Table 4.1 for the density model obtained from gravity only and joint inversion of gravity with surface wave data. ....75

Figure 7.4: RMSE per depth plot of Table 4.2 for the velocity model obtained from the surface wave only and joint inversion of gravity with surface wave data. ....75

Figure 7.5:  $g_z$  data misfit .....76

Figure 7.6 : Gravity data misfit obtained from the gradient data only inversion .....76

Figure 7.7: Gravity data misfit obtained from the  $g_z$  and  $g_{zz}$  gravity data only inversion.....77

Figure 7.8: Gravity data misfit obtained from the  $g_z$  and  $g_{all}$  gravity data only inversion.....77

Figure 7.9: Rayleigh wave group and phase velocity data misfit obtained from cenario-2 of surface wave only inversion.....78

Figure 7.10: The gravity field data ( $g_z$ ) misfit after the joint inversion with the surface wave data. ....78

Figure 7.11: The fundamental mode Rayleigh wav group and phase velocity misfit after the joint inversion with the gravity field data only. ....79

Figure 7.12: The gravity data (gravity field and six component of gradient data) misfit after jointly inverted with the surface wave data (group and phase velocity data).....79

Figure 7.13: The fundamental mode Rayleigh wav group and phase velocity misfit after the joint inversion with the gravity field and six component gradient data. ....80

Figure 7.14: Starting model used for the inversion. The starting velocity model is interpolated from the global AK135 1d velocity model to 200 km depth shown in the cross-section plot from lines A-A' and B-B'. .....81

Figure 7.15: 3D true density contrast model (expressed in  $kg/m^3$ ). Top panel, the depth slice plot at different depths of 7.5, 42.5, and 122.5 km. The bottom panel is the cross-section plot obtained using the profile lines A-A', B-B', and C-C'. The different geological units such as the Nosope and Passarge sedimentary basin (NB & PB), buried Maltahohe micro-craton (MC), Congo craton (CC), the Kalahari craton (KC), the Okavango rift zone (ORZ), and the East African Rift system (ER), are depicted as a homogeneous block from the background values. ....82

Figure 7.16: Gravity data misfit obtained from the  $g_z$  and  $g_{all}$  gravity data only inversion.....84

Figure 7.17: The fundamental mode Rayleigh wav group and phase velocity misfit after the joint inversion with the gravity field and six component gradient data. ....84

Figure 7.18: The gravity data (gravity field and six component of gradient data) misfit after jointly inverted with the surface wave data (group and phase velocity data).....85

Figure 7.19: The group and phase velocity dispersion velocity misfit plot after jointly inverted with the gravity field and six component gradient data. ....85

Figure 7.20: The vertical gravity field data misfit obtained after joint inversion of the gravity and surface wave data of Botswana. ....86

Figure 7.21: The data misfit plot for the six-component gravity gradient data obtained after joint inversion of the gravity and surface wave data of Botswana.....87

Figure 7.22: Period slice plot of group (a-c) and phase (d-f) velocity data misfit map obtained after joint inversion of the gravity and surface wave data of Botswana..... 88

## LIST OF TABLES

---

Table 4.1: RMSE per depth comparison for density model misfit obtained from scenario-1 of gravity data only and scenario-3 of the joint inversion of gravity and surface wave data.....	32
Table 4.2: RMSE per depth comparison for velocity model misfit obtained from scenario-2 of surface wave only and scenario-3 of the joint inversion of gravity and surface wave data.....	32
Table 4.3 A summary of the data misfit RMSE obtained from the three inversion scenarios.....	33
Table 5.1: RMSE of the recovered density and velocity model from the single data inversions scenario-1 & -2 and joint inversion of both data sets scenario-3.....	48
Table 5.2: Data misfit RMSE for each of the inversions conducted using the single data and joint inversion of the data set.....	48
Table 6.1 RMSE of the data misfit for the real data joint inversion of gravity and surface wave data.....	59
Table 7.1: Parameters used during the first phase of synthetic method test.....	73
Table 7.2: Parameters used during the second phase of complex synthetic method test.....	83
Table 7.3: Inversion parameters used for the real data application.....	86

# 1. INTRODUCTION

## 1.1. Background

The integration of multiple independent geophysical data sets called cooperative inversion was defined first by Lines et al. (1987). In their paper, they discussed the concept of the cooperative inversion using data sets from surface and borehole measurements of seismic and gravity data. They classified the approach into two, sequential and joint inversion. Both approaches handle the data sets differently. Sequential inversion treats each data set separately, and the result of one inversion is used to begin a subsequent inversion (Lines et al., 1987). In joint inversion, however, different data sets are weighted and used simultaneously while a coupling relationship is established between the data sets. Therefore, due to the benefits of integrating different data sets that are sensitive to different materials of the Earth simultaneously, joint inversion of multiple data sets can better estimate Earth's physical properties (Afonso et al., 2013; Julia et al., 2000, 2005; Maceira and Ammon, 2009).

The constrained optimization problem to generate subsurface model from different independent data sets jointly helps to reduce the intrinsic non-uniqueness of the geophysical inverse problem and also improves the resolving power of the individual dataset. Additionally, the variation of sources of noise and their impact on collected data often varies leading to complexity in resolution in the retrieved subsurface model from geophysical inversion. Thus, instead of adding more of one type of data, the different data sets are combined to resolve the disparities and improve the retrieved models (Julià et al., 2000). Effectively, with the recent prevalent availability of geophysical data sets, their integration in a joint inversion scheme has become a widespread active research area in small scale exploration or large scale lithospheric modelling (Afonso et al., 2016; Liao et al., 2021; Syracuse et al., 2017; Wu et al., 2022).

In the past few decades, there has been an attempt to use seismic data combined with satellite gravity measurements in the joint inversion to model the density and velocity structure of the subsurface. For example, Maceira and Ammon. (2009) developed the first approach to jointly invert seismic surface wave Rayleigh group velocity with satellite gravity data using rectangular prisms as geometric system for model discretization. This rectangular prism has the advantage of reducing analytical and computational costs, but it does not consider the effect of the Earth's spherical curvature for areas with spatial coverage larger than  $10 * 10$  degrees. Moreover, they only used group velocities dispersion data, and their approach was not developed to utilize gravity gradient measurements. Then, Afonso et al. (2013) developed a 3D inversion algorithm using a Bayesian probabilistic approach to invert multiple data sets from geophysical measurements. This combination of different data sets helps resolve the subsurface structure in detail and results in comprehensive high-resolution geophysical models. However, it is computationally expensive and requires a different (compositional) data set and constraints that are not easily accessible, and the employment of a cartesian coordinate system may limit its application for regional modeling. Recently, Roecker et al. (2017) also performed the joint inversion of body wave, surface wave, and gravity data to image the magmatic manifestation of the eastern rift system around northern Tanzania and southern Kenya. In their approach, Roecker et al.(2017) used a spherical coordinate system assuming constant density within the spherical element centred at each node for the gravity forward problem. However, the joint inversion is performed in a stepwise or progressive fashion. Further, the inversion was based on phase velocity surface wave data, and the method was not designed to handle satellite gravity gradient data. Despite the strength

and limitations of the joint inversion approaches described in this paragraph, they are applied in different part of the world for lithospheric modeling.

The lithosphere, which consists of the crust and uppermost part of the mantle, is part of the Earth's rigid outer layer where most tectonic activities occur along plate boundaries. By the plate boundaries, the lithosphere of the Earth can be divided up into numerous different lithospheric plates, each of which has its own unique composition, thickness, and density. Understanding the density and velocity structure of the lithosphere is crucial to better understand the distribution of the Earth resources and also the associated natural hazards.

The lithospheric plate of Africa contains tectonic elements that are fundamental to understand the global tectonics and plate tectonic theory (Begg et al., 2009). The African lithospheric plate comprises major Archean cratonic blocks and fragments of cratons that are bounded by younger mobile belts and intra-cratonic boundaries (Begg et al., 2009).. Understanding the tectonic history of cratons and their relationship with the mobile belts can assist in understanding the tectonic evolution and geodynamics of Africa (Begg et al., 2009). Moreover, the African superswell and the East African Rift System (EARS) are major tectonic activities that affects the African plate tectonics and geodynamic evolution (Figure 1.1). One of the regions where the Archean cratons, mobile belts, EARS and the African superswell intersects is Botswana. Better understanding the tectonics of Botswana could contribute to improve our understanding of the African tectonics and geodynamics and can help in better understanding some fundamental tectonic concepts, for example, rift initiation and development (e.g., Macgregor,D (2015)).

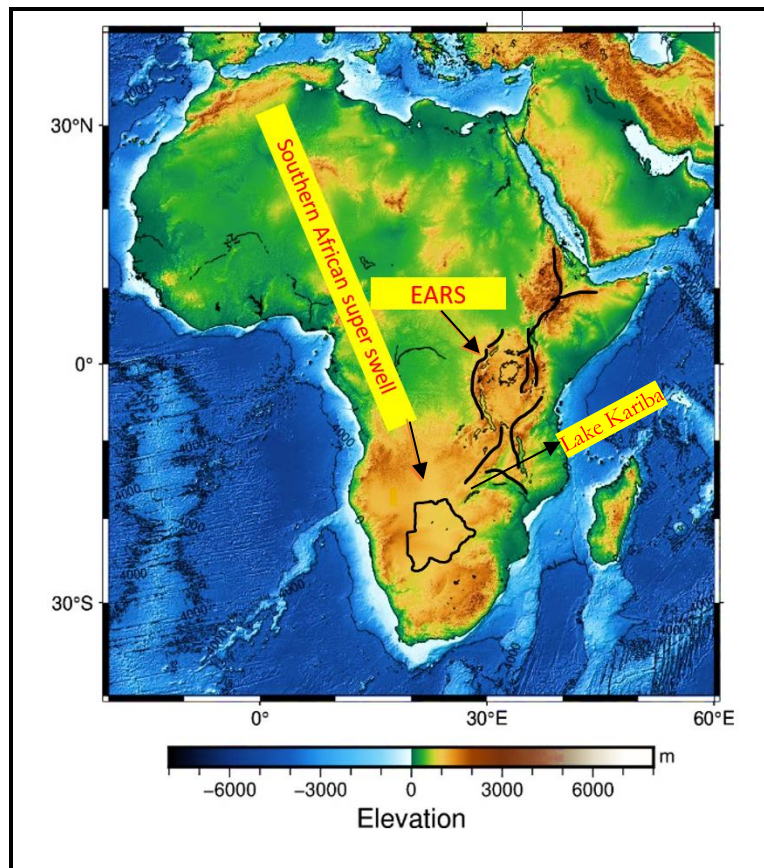


Figure 1.1 Topographic map of Africa showing the location of Botswana outlined by its boundaries in southern Africa. The African Superswell in the southern Africa region, the east and west branches of EARS and Lake Kariba which is expected to be the last surface expression of the EARS are indicated by black arrows.

Recently Botswana's lithosphere has been investigated using different types of geophysical measurements (e.g., seismology, gravity, magnetics, and electromagnetics). Even though several geophysical investigations were conducted in the area, there are some discrepancies that are not yet understood about the tectonics and geodynamics of Botswana. As a result, Botswana lithospheric structure is still the subject of some debated hypotheses and divergent views. For example, seismological studies of Begg et al. (2009) and Fadel et al. (20180 and recent MT study of Akinremi et al. (2022) indicted the existence of separate buried

Maltahohe micro-craton in southwest Botswana. However, their findings contradict with an earlier deep seismic profiling of the Nosop basin, indicated and interpreted it as the western extension of the Kaapvaal Craton (A. Wright and Hall, 1990). Furthermore, there is an argument for the southward continuation of the EARS in ORZ and central Botswana, and its linkage with the April 3<sup>rd</sup>, 2017, 6.5 Mw Botswana's largest earthquake is yet to be fully understood. Pastier et al. (2017) argued that there is no rifting in ORZ; instead, they propose the area as a deformation zone between bounding craton and plates. However, recent geophysical studies (e.g., Fadel et al., 2020; Leseane et al., 2015; Y. Yu et al., 2015) interpreted as the presence of rifting in ORZ as the southward extension of the western branch of EARS on ORZ and even to central Botswana where the April 3<sup>rd</sup> 6.5 Mw earthquake occurred (Figure 1.2). This argument is also supported by the most recent seismic study across the Kalahari by Paulssen et al. (2022). However, this contradicts with the finding of Kolawole et al. (2017) suggesting as the earthquake was not related to the EARS extension. Rather, they suggested an extensional reactivation of a thrust splay in the crust at the earthquake region. Therefore, despite a small-scale study of the ORZ characteristics using a joint inversion of gravity and receiver function (Y. Yu et al., 2015), the previously conducted nationwide research in Botswana, are mostly single data inversion and they are inconclusive to better understand the tectonic features and lithospheric structure of Botswana.

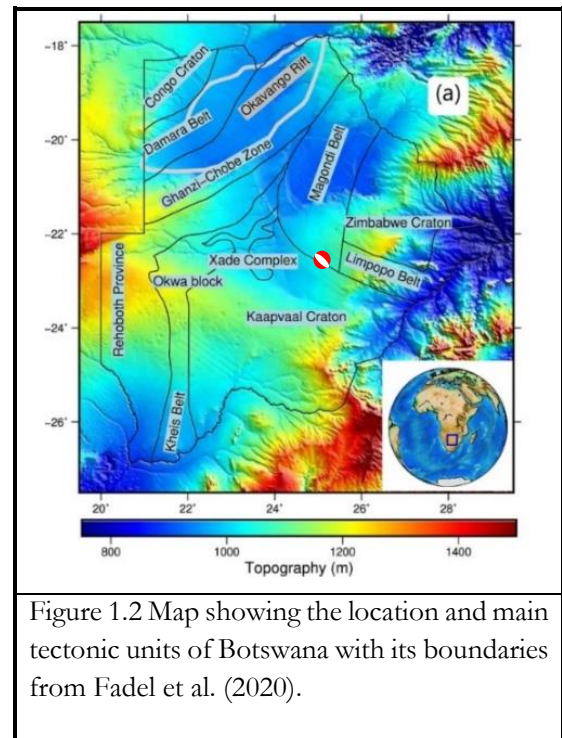


Figure 1.2 Map showing the location and main tectonic units of Botswana with its boundaries from Fadel et al. (2020).

This study will use the strength of the joint inversion approach using satellite gravity and its gradient data with seismic surface wave data that has never been integrated before in Botswana. Seismological measurements are the common geophysical techniques used jointly with gravity measurements for subsurface density and velocity investigations (Blom et al., 2017; Kaban et al., 2016; Koslovskaya et al., 2004). Among seismological measurements, seismic surface waves Rayleigh group and phase velocity have been used with gravity data for subsurface velocity and density modelling because of their sensitivity to density, albeit only weakly (e.g., Maceira and Ammon, 2009).

The gravity gradient data is increasingly used in the industries for mineral or oil explorations and for crustal targets. A limited studies have attempted to invert the gravity gradient data for lithospheric modelling (e.g., Afonso et al., 2019). The unique feature of acquiring the gradient data globally using GOCE satellite data and its homogeneous coverage make it useful for large scale subsurface modelling (Bouman et al., 2015). However, satellite gravity gradient data's full potential and sensitivity to the geometry of 3D subsurface density structures have yet to be fully exploited (Van der Meijde et al., 2015). As such, the unique inclusion of gradient data sensitivity for subsurface information in the joint inversion for this study is expected to give a more resolved model. Therefore, the integration of two data set (e.g., satellite gravity and seismic surface wave) in a joint inversion will provide additional insight into crucial geodynamical and structural questions in Botswana regarding cratonic boundaries and extension of EARS extension in ORZ and central Botswana. These phenomena are relevant in the understanding of rifting and earthquakes occurrence that plays a significant role in hazards assessments for human safety and in exploration context as cratons and mobile belts are known to host minerals of economic significance (Black and Liegeois, 1993). The simultaneously

recovered density and velocity models from the joint inversion of gravity and the seismic surface wave data can help to map and delineate tectonic units and their spatial and depth extent. Therefore, the expected low velocity and density associated with rifting and sedimentary basin (e.g., Fadel et al., 2020; Maceira and Ammon, 2009) and high velocity and density anomaly associated with thick and strong cratonic blocks (e.g., White-Gaynor et al., 2021) will help to elucidate the arguments mentioned above about the tectonic questions of Botswana.

## 1.2. Problem statement

At this moment, there are limitations in the available methods that can efficiently use the available satellite gravity and its gradient data with surface wave measurements for regional and global studies. Additionally, there are unresolved debates on the tectonics and geodynamics of Botswana mentioned in the previous section. Furthermore, joint inversion of multiple geophysical data (e.g., satellite gravity and seismic surface wave data) has never been conducted at regional scale in Botswana to address the debates about Botswana tectonics. This study aims to test a new joint inversion method developed by Fadel (2018) which jointly invert gravity (including the gradients) and surface wave data and implement it on Botswana to enhance understanding of the crust and upper mantle tectonic features and geodynamics. However, the performance of the joint inversion method for high-resolution and large-scale modelling has not been fully evaluated yet. Furthermore, at the time of this study, the method was not fully ready to use for real data applications. Exploring the strengths of the joint inversion on Botswana case study can provide better insight into the crucial geodynamical and structural questions in the study area. The new information from the 3D density and velocity model also could potentially contribute to confirming and rejecting the hypothesis presented about the existence of MC, rifting in ORZ, and the extension of EARS to central Botswana. Therefore, the combination of gravity with seismic surface wave data will give us a better insight about the density, and velocity nature of the subsurface (and hence temperature and fluids) which can help us to resolve the configuration of the subsurface more confidently.

## 1.3. Research Objectives

### 1.3.1. Main Objectives

The main objective of the research is to test and apply a newly joint inversion approach that integrates gravity and its gradient with seismic surface wave data to image the 3D density and velocity structure of Botswana's crust and upper most mantle and thereby confirm or reject the existing hypothesis on the tectonics of Botswana.

### 1.3.2. Sub-Objectives and Questions

**The sub-objectives of the proposed research with the respective research question are described below: -**

1. To test the efficiency of the joint inversion approach of Fadel (2018) in terms of computational cost and scalability to define the model parameters.

- How efficient is the existing inversion approach to model the subsurface velocity and density distribution at different resolutions?
- What should be the optimum inversion parameters, and how to adjust them efficiently?
- How is the weighting of the individual data set treated for the joint inversion?

2. Evaluate satellite gravity gradient data's added value for subsurface density modelling using synthetic models.

- What is the added value of satellite gravity gradient data on the developed density model?

3. Implement the joint inversion methodology on Botswana and visualize the depth and spatial extent of the cratons, including the Maltahohe, buried micro-craton to understand their deformation history.

- Can the inverted velocity and density model help to confirm the existence of buried micro-craton?
- If the existence of the micro-craton is confirmed, what are the depth and spatial extent of the boundaries?

4. Use the joint inverted model to image and delineate the southward extension of the EARS at the ORZ and confirm or reject its extension to central Botswana.

- Can the inverted velocity-density model indicate and map the presence of rifting along the Okavango zone?
- Can the inverted velocity-density model indicate the extension of EARS to central Botswana?

5. If the extension of EARS to central Botswana exists, better understand its linkage with the 3<sup>rd</sup> of April earthquake.

- What is the relation of the EARS to the April 3, 6.5 Mw earthquake?

#### **1.4. Thesis Structure**

Chapter 1: includes background, a brief description of the research problem, research objectives, and research questions.

Chapter 2: includes a detailed description of the geology of the study area and previous studies.

Chapter 3: includes a detailed description of the methodology.

Chapter 4: Includes first phase of method test using a simple synthetic geological model.

Chapter 5: Includes second phase of method test using a complex synthetic geological model mimicking Botswana geology.

Chapter 6: includes real data application of the joint inversion approach.

Chapter 7: includes the conclusion, and recommendations.

## 2. STUDY AREA AND DATA SET

In this chapter, a brief overview of the study area and geology (section 2.1 & 2.2) and a description of the data set used in this study are presented.

### 2.1. Study Area

This study is conducted in Botswana, an interesting area in southern Africa which contains a diversity of cratons, sedimentary basins, and sutured mobile belts. It covers the structurally deformed zone between the Kalahari (KAAPVAAL and ZIMBABWE blocks) and the Southern part of Congo Craton, as shown in Figure 2.1. In between the stable cratonic blocks, accretion and rifting led to the formation of mobile belts and sedimentary basins (Haddon, 2005). As a result, the interaction of these cratons with the mobile belts shaped the lithospheric structure of Botswana through time (Begg et al., 2009; Simon et al., 2012). A detail description of the main geologic units of Botswana are given in the following sections.

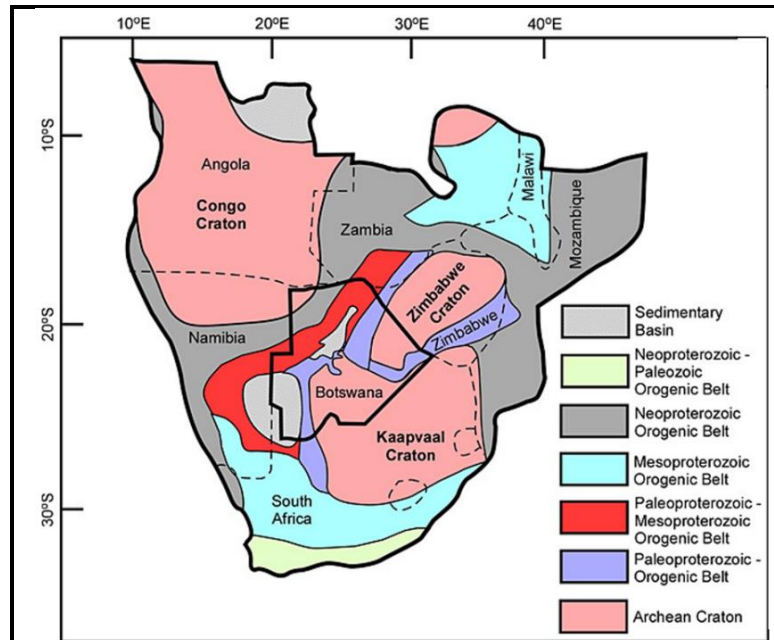


Figure 2.1: The tectonic map of Southern Africa with the outline of Botswana boundary at the center from Leseane et al. (2015) showing the Archean Cratons, orogenic Belts, and Sedimentary basins.

#### 2.1.1. Cratons

This section provides an overview of the major cratons that, includes the Kalahari craton (comprised of the Kaapvaal and Zimbabwe cratons), the Congo craton, and the Rehoboth province in Botswana.

##### 2.1.1.1. Kalahari Cratons

The Kalahari craton comprises the larger Kaapvaal Craton in the southeast and the smaller Zimbabwe Craton in the northeast (Figure 2.1). The two cratonic blocks are separated by the Limpopo Belt in between (Figure 2.2). The Kaapvaal craton is the oldest cratonic block formed between 3.7 – 3.2 Ga ago in Botswana (Fadel, 2018). Granitoids mainly cover this craton with gneisses and greenstone belts (Haddon, 2005). The second Kalahari cratonic block, known as the Zimbabwe craton, was formed between 3.57 - 3.37 Ga ago, consisting of 20 % of greenstone belts and granite-gneiss complexes covering the rest (Jelsma and Dirks, 2002). This cratonic block is uncomfortably overlain by flood basalt, komatiites, and sediments (Begg et al., 2009). As a result, the Kalahari Craton is not exposed in many parts of Botswana, but it is a large and old Archean craton covering large parts of Botswana's subsurface with keel extending deeper than 200km (Begg et al., 2009; Midzi et al., 2018; Fadel et al., 2019).

Proterozoic belts and mafic complexes surround the Kalahari Craton, some of which intruded and affected these stable crustal blocks (Begg et al., 2009). In the western and northern margins of the Kalahari Craton lies the Kalahari Suture Zone, a Paleo-Proterozoic thrust zone that separates it from the spatially attached

Damara-Ghanzi-Chobe belt (Figure 2.2). Besides separating the Kalahari Craton from the Damara-Ghanzi-Chobe Proterozoic belt, the Kalahari Suture Zone played a major role in forming the Kheis-Okwa-Xade-Magondi Belt (e.g., Reeves and Hutchins, 1982). The Kalahari Suture Zone is made up of two lines: the Kalahari Line, which runs along the Kheis-Okwa Belt from South Africa to southern Botswana, and the Makgadikgadi Line, which runs north-east from the Kaapvaal Craton to the Magondi Belt (Figure 2.2, Haddon, 2005).

### 2.1.1.2. Congo craton

The Congo craton is also an Archean to Paleoproterozoic craton in southern Africa, where most part of the craton is found in Angola and Namibia. It extends to the northwestern part of Botswana, where its boundary has been the subject of ample assumption and is not exposed due to the thick sediment overly (Corner and Durrheim, 2018; Key and Ayres, 2000; Khoza et al., 2013). The Congo Craton contains Archean and Paleoproterozoic rock units separated from the Kaapvaal and Zimbabwe Craton by the Damara and Ghanzi-Chobe Mobile Belts (Figure 2.2) and, it is mainly comprised of granitoid rock units, including gneisses and granulite, which are intruded by younger granite plutons (Begg et al., 2009). The oldest rock units recorded in the Congo craton are believed to be between 3.2 – 2.9 Ga ago (Fadel et al., 2018).

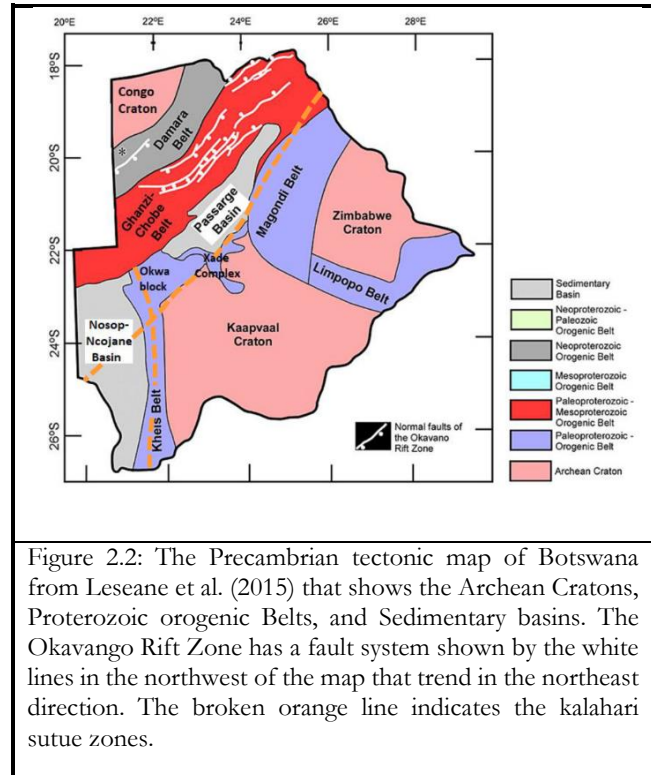


Figure 2.2: The Precambrian tectonic map of Botswana from Leseane et al. (2015) that shows the Archean Cratons, Proterozoic orogenic Belts, and Sedimentary basins. The Okavango Rift Zone has a fault system shown by the white lines in the northwest of the map that trend in the northeast direction. The broken orange line indicates the kalahari sutue zones.

### 2.1.1.3. Rehoboth province

The Rehoboth province, an area covered by an extensive cover of the Kalahari sediments (Begg et al., 2009; Van Schijndel et al., 2014; Simon et al., 2012), lies under the Nosop basin in Botswana and extends to the west in Namibia (Figure 2.1). Most parts of the Rehoboth province were formed during the Paleoproterozoic around 2.2 - 1.9 billion years ago; nevertheless, the province's full assembly date is not yet determined (Van Schijndel et al., 2011). Initially, it was defined as a sub-province of the Namaqua province in Namibia and South Africa (Van Schijndel, 2013). However, it was later suggested that it is accreted to the Kaapvaal craton between 1.93 and 1.75 billion years ago (Tinker et al., 2004). It has been suggested that there is an ancient buried micro-craton in Rehoboth Province (Begg et al., 2009; Fadel et al., 2020), which has also been interpreted as a deep extension of the Kaapvaal Craton by Wright and Hall (1990).

## 2.1.2. Mobile Belts

This section briefly summarizes the mobile Belts, including the Limpopo Belt, Damar-Ghanzi-Chobe belt, and Kheis-Okwa-Magondi Belt.

### 2.1.2.1. Limpopo Belt

The Limpopo belt, located in eastern Botswana and extending to the southern part of Zimbabwe (Figure 2.1 & Figure 2.2), contains reworked metamorphic terrains during Proterozoic. The Limpopo belts are dominated by metamorphic assemblages: migmatite, porphyritic granite, gneissic granite, metasedimentary rocks, and meta-intrusive rocks are among the most common rocks. (Key and Ayres, 2000). It separates the

Kaapvaal and Zimbabwe cratons and is formed during the two cratons' collision between 2.7 – 2.5 Ga (Begg et al., 2009; Fadel, 2018).

#### **2.1.2.2. Damara-Ghanzi-Chobe Belt**

The Damara-Ghanzi-Chobe Belt is located bounding the southeastern margin of the Congo Craton in the northwest and the Kalahari Craton in its southeast (Figure 2.2). As part of Botswana's northern region, the Damara Belt comprises highly metamorphosed Sedimentary rocks that were formed during the Damara orogeny when the Congo and Kalahari Cratons collided together from 550-500 million years ago (Meneghini et al., 2017 A. Wright and Hall, 1990; Fadel et al., 2018; Nascimento et al., 2017).

An area of the southern part of the Damara Belt is bounded by the Ghanzi-Chobe Belt (Modie, 2000), which is comprised of a sequence of folded late Proterozoic metasedimentary rocks (A. Wright and Hall, 1990; Lintern et al., 2016). Initially, the Ghanzi-Chobe Belts were formed as a rift basin developed through extensional tectonics. Later, during the Damara Orogeny, the basin was deformed, resulting in folded and thrust belts (Meneghini et al., 2017).

The Okavango Rift Zone (ORZ), located within the Damara-Ghanzi-Chobe Belt (Modisi, 2000), is one of the seismically active areas in Botswana (Midzi et al., 2018) and is interpreted to be the terminus of the southward extension of the EARS (Fadel et al., 2018; Leseane et al., 2015). Several studies of the lithosphere beneath the ORZ (e.g., Leseane et al., 2015; Yu et al., 2015b; Yu et al., 2017) suggest the development of rift initiation in the area. According to their finding, the rifting process cuts across the Damara and Ghanzi-Chobe belts. Additionally, a joint inversion of receiver function and gravity study by Yu et al., (2015) suggested the presence of melts and lithospheric stretching below ORZ evident from their low upper mantle density anomaly. However, this idea of rifting in ORZ conflicts with the idea postulated by Pastier et al., (2017). Their investigation beneath the ORZ argued that there is no rifting in Okavango; instead, they propose the area as a deformation zone between bounding cratons and plates. Recent seismological studies of Botswana (e.g., Fadel et al., 2020, 2018) indicated the presence of rifting in ORZ that even continues to central Botswana as evidenced from their thin crust and low velocity anomalies.

#### **2.1.2.3. Kheis-Okwa-Magondi Belt**

The composite Kheis-Okwa-Magondi Belt covers the central part of Botswana, bounding the western margin of Kaapvaal and the Zimbabwe Craton (Figure 2.2; Begg et al., 2009). The Kheis Belt formed about 2 Ga ago and ran northward along the western boundary of the Kaapvaal Craton. It is a fold and thrust belt consisting of low-grade metavolcanic and metasedimentary rocks (Haddon, 2005; Midzi et al., 2018). The Kalahari suture zone separates the Kheis Belt from the neighbouring Rehoboth province (Oriolo and Becker, 2018).

Within the Okwa block, located on the northern edge of the Kheis Belt (Figure 2.2), are metamorphic rocks that are estimated to be about 2 Ga years old and are believed to be underlain by Archean rocks (Begg et al., 2009). The area called Okwa-Magondi terrain surrounding the northeastern part of the Limpopo Belt and western part of the Zimbabwe Craton has an unclear outcrop due to the thick Kalahari sand coverage (Midzi et al., 2018). Along the western edge of Zimbabwe Craton is the early Proterozoic Magondi belt comprised of a thick sequence of sediments and volcanic rocks that metamorphosed between 2.1 – 1.96 Ga ago. The Magondi Belt unconformably overlies the Zimbabwe Craton in the west, and the younger sediments overlie the western boundary of the mobile belts. Later during the Eburnean Orogeny, which took place between 2.0 - 1.8 Ga, the Magondi basin and the Okwa-Kheis Belt accreted together (Thomas et al., 1993).

### 2.1.3. Nosop and Passarge Basins

In Botswana, two major sedimentary basins are located between the Kheis-Okwa-Magondi belt and the Damara-Ghanzi-Chobe belt. The Nosop basin, which covers the upper crust of Botswana, is located in southwest Botswana. It is covered by thick, more than 10 km sediment deposition from the Nama group sediment, consisting of marine carbonates and siliciclastic rocks (A. Wright & Hall, 1990; Begg et al., 2009; Pretorius, 1984).

On the other hand, the Passarge basin is located in the central part of Botswana between the Ghanzi-Chobe Belt in northwestern Botswana and the Kaapvaal Craton. A thick sedimentary cover covers the basin, similar to the Nosop basin. The sediment is approximately 10 km thick and is composed of siliciclastic and carbonate sedimentary rocks from the Ghanzi group sediment (Key & Ayres, 2000; Pretorius, 1984).

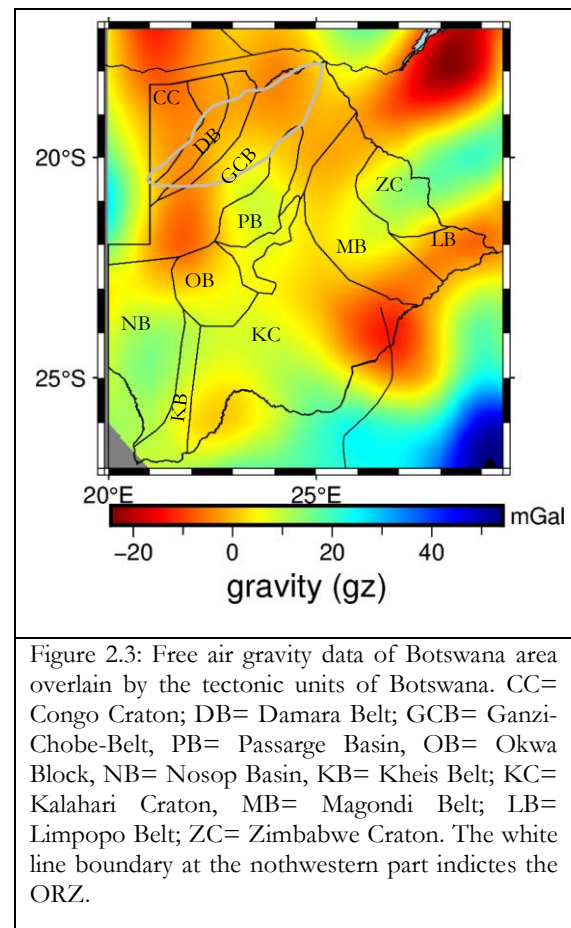
## 2.2. Data set

This research used satellite gravity data (free air gravity field and GOCE gravity gradient data) and seismic surface wave data obtained from several different seismological stations. The details of both datasets are explained below.

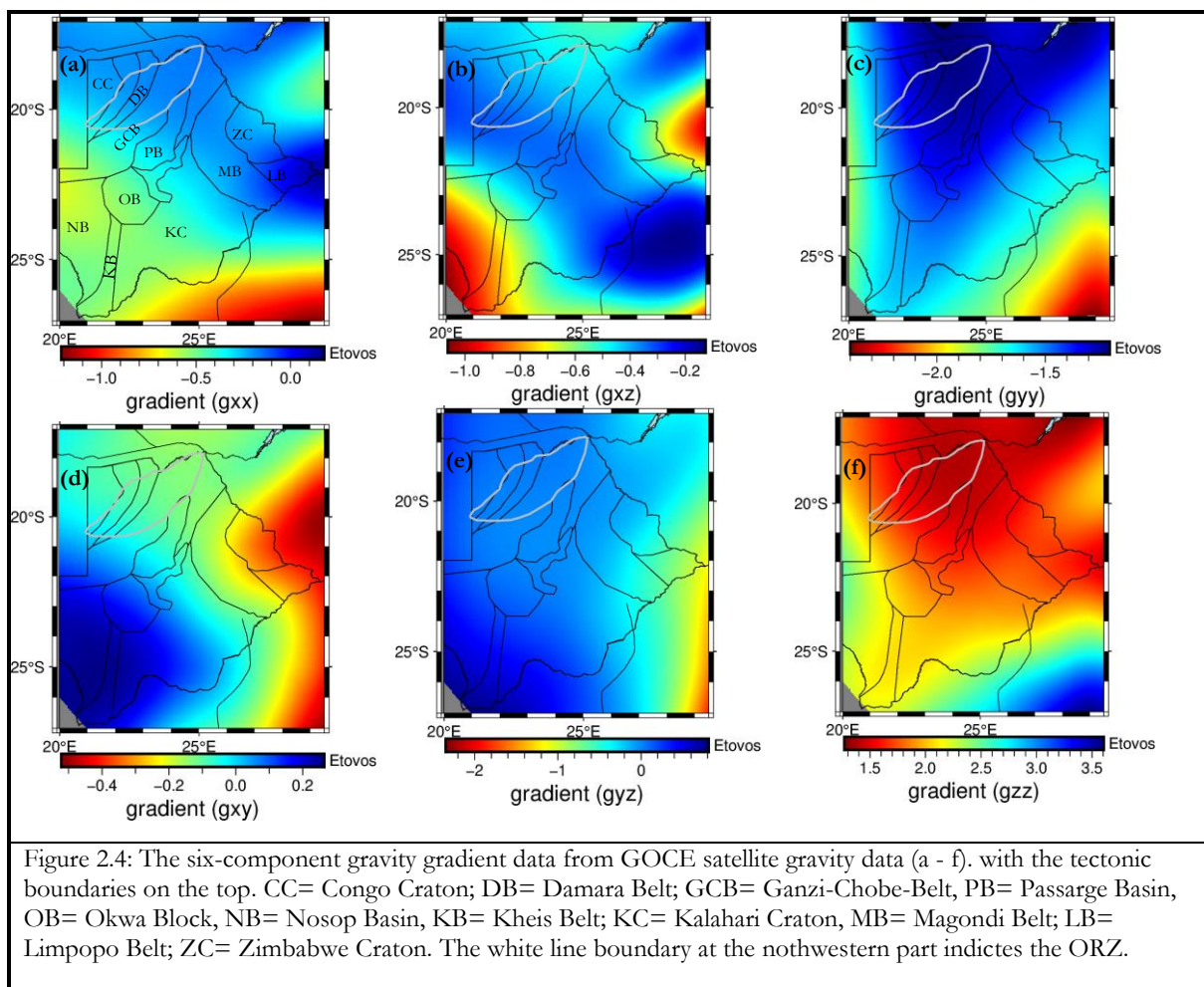
### 2.2.1. Gravity data

The free air gravity data was obtained from the combined gravity model EIGEN-6C4 (Förste et al., 2015) and the six component gravity gradient data from direct GOCE measurements (last accessed June 10, 2022). The free-air gravity anomaly from Eigen-6C4 is a high-resolution satellite gravity data, which was built from the prior EGM2008 model with GOCE, GRACE, and satellite altimetry data added to it (Förste et al., 2015). The model has a resolution of up to degree and order 2190, which can reach up to 0.1 degrees spatial resolution. However, to keep the consistency with the spatial resolution of the surface wave data that are obtained at one degree (Fadel et al., 2020), the free air gravity data shown in Figure 2.3, is obtained at one-degree spatial resolution. The data is available freely from the International Centre for Global Earth Models (ICGEM: <http://icgem.gfz-potsdam.de/calcgrid>).

Furthermore, shallow source short wavelength signals are filtered from the gravity signal to avoid disturbance in the inversion processes. This is due to the fact that the shallow source features in the data could not be retrieved in the inversion, making it difficult to fit the data. Therefore, the total free air gravity field data are filtered with low pass filtering using the calculation service of the ICGEM called truncating the model. As a result, the low pass gaussian filtering was conducted by lowering the spherical harmonic expansion to remove high frequency content of the signal. The figure plotted in Figure 2.3 shows the low pass filtered free air gravity anomaly.



On the other hand, the gravity gradient data is obtained from the GOCE gravity satellite of the European space agency. The GOCE gravity gradient data provides a global homogeneous gravity profile covering the whole Earth at a satellite altitude of 225 km and has a configuration of  $V_{xx}$ ,  $V_{xz}$ ,  $V_{yy}$ ,  $V_{xy}$ ,  $V_{yz}$ , and  $V_{zz}$ , (Figure 2.4 (b-g); Bouman et al., 2016). The six component gradient data have different sensitivities to the subsurface density distributions from different angles. Furthermore, gravitational gradients at satellite altitude have the benefit of being limited to wavelengths greater than 50 km, making them excellent for studying the regional crustal or lithospheric setting and containing long wavelength signals (Bouman et al., 2016). It is freely accessible and downloaded from the official website of the European Space Agency ([https://goce-ds.eo.esa.int/oads/access/collection/GOCE\\_Global\\_Gravity\\_Field\\_Models\\_and\\_Grids/](https://goce-ds.eo.esa.int/oads/access/collection/GOCE_Global_Gravity_Field_Models_and_Grids/)) with a spatial resolution of 0.2 degrees. However, in this study the gradient data were interpolated to one degree using spline interpolation to make it consistent with the surface wave and vertical gravity field spatial resolution. Figure 2.4 below shows the six components of the gravity gradient data from GOCE satellite.



### 2.2.2. Surface wave data

The surface wave dispersion velocity data consists of the fundamental mode Rayleigh wave group and phase velocity measurements. These dispersion measurements were taken from the regional shear wave analysis of Botswana conducted by Fadel et al., 2020. They computed short period Rayleigh wave group (3-30 sec) and phase velocity (3-35 sec) from ambient noise and longer periods phase velocities (30-120 sec), from Helmholtz tomography of teleseismic earthquake signals using automatic frequency-time analysis (more information of the data processing is presented in Fadel et al., 2020). The phase velocity measurement obtained from ambient noise and Helmholtz tomography have overlapping regions from 30-35 sec period.

As a result, the two measurements from ambient noise and earthquake signals were merged using the overlapping region of the two measurements from 30-35 sec to have a smooth transition of the dispersion curve (Fadel et al., 2020 and reference therein). Figure 2.5 & 2.6 shows the distribution of the seismological stations and the Rayleigh wave group and phase velocity dispersion maps at different time periods.

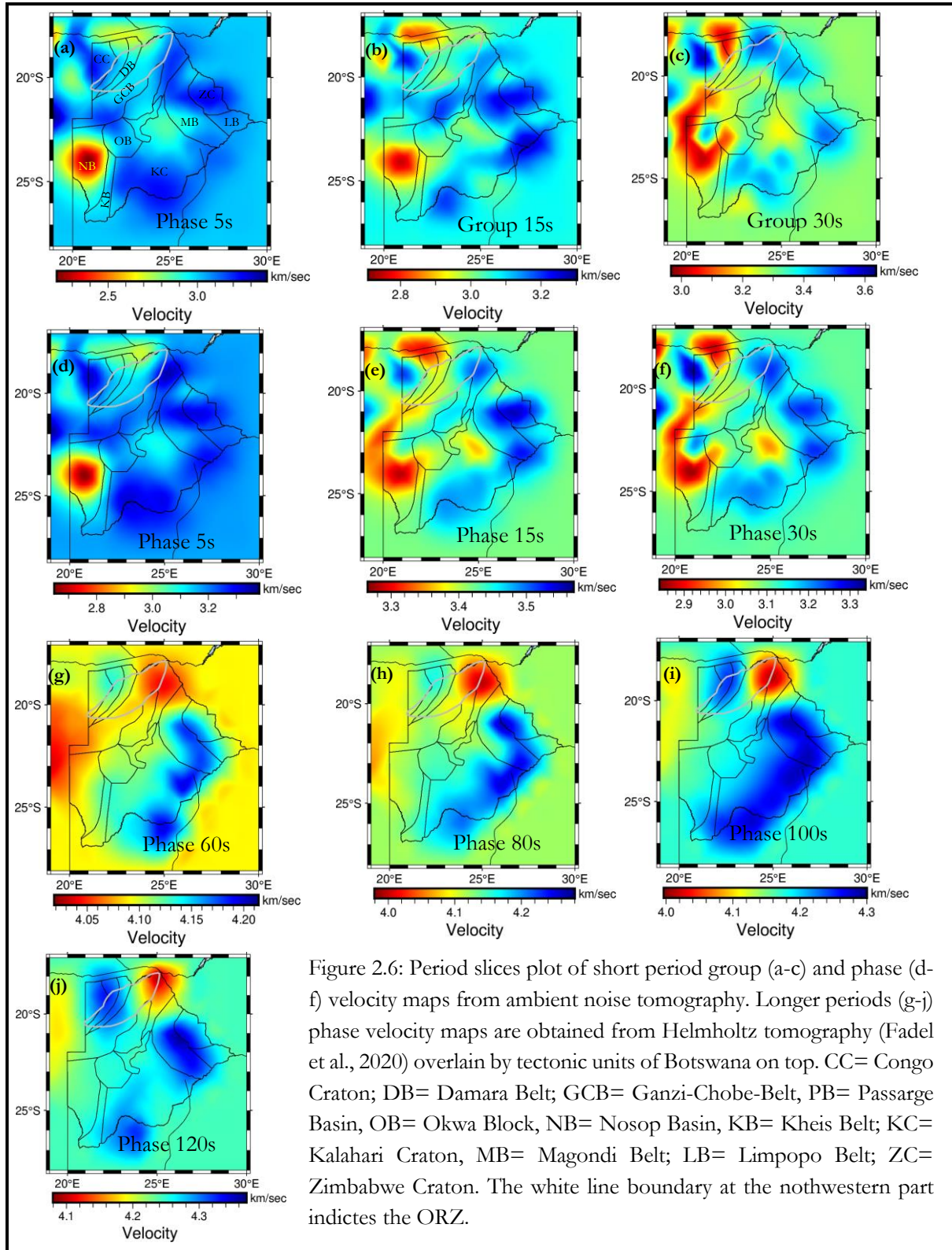


Figure 2.6: Period slices plot of short period group (a-c) and phase (d-f) velocity maps from ambient noise tomography. Longer periods (g-j) phase velocity maps are obtained from Helmholtz tomography (Fadel et al., 2020) overlain by tectonic units of Botswana on top. CC= Congo Craton; DB= Damara Belt; GCB= Ganzi-Chobe-Belt, PB= Passarge Basin, OB= Okwa Block, NB= Nosop Basin, KB= Kheis Belt; KC= Kalahari Craton, MB= Magondi Belt; LB= Limpopo Belt; ZC= Zimbabwe Craton. The white line boundary at the northwestern part indicates the ORZ.

### 3. METHODOLOGY

The research uses the joint inversion approach that integrates the satellite gravity and seismic surface wave data developed by Fadel (2018) and has only been synthetically tested with limited scenarios. During the initial development of the method, the performance of the method that demands high computing time was a major concern. However, during this research phase, the method was updated by the main developer to improve the performance and decrease the computing time of the joint inversion approach. Therefore, this chapter will give an overview of the joint inversion scheme that will be used in this research and describe how the method's performance was improved (section 3.1). Finally, an overview of the joint inversion implementation for the synthetic test and real data application are presented (section3.2).

#### 3.1. Joint Inversion Method

Figure 3.1 shows the diagrammatic representation of the joint inversion scheme. The methodology is divided into two basic components: the forward solver that calculates the model response using the gravity and surface wave forward calculation and the inversion formulation that uses a pre-formulated objective function to produce the subsurface model, which optimally minimizes such function. The methodology was designed in a spherical coordinate system that is suitable for local, regional, and global scale studies. In the following section, a detailed description of the two components of the joint inversion scheme is presented.

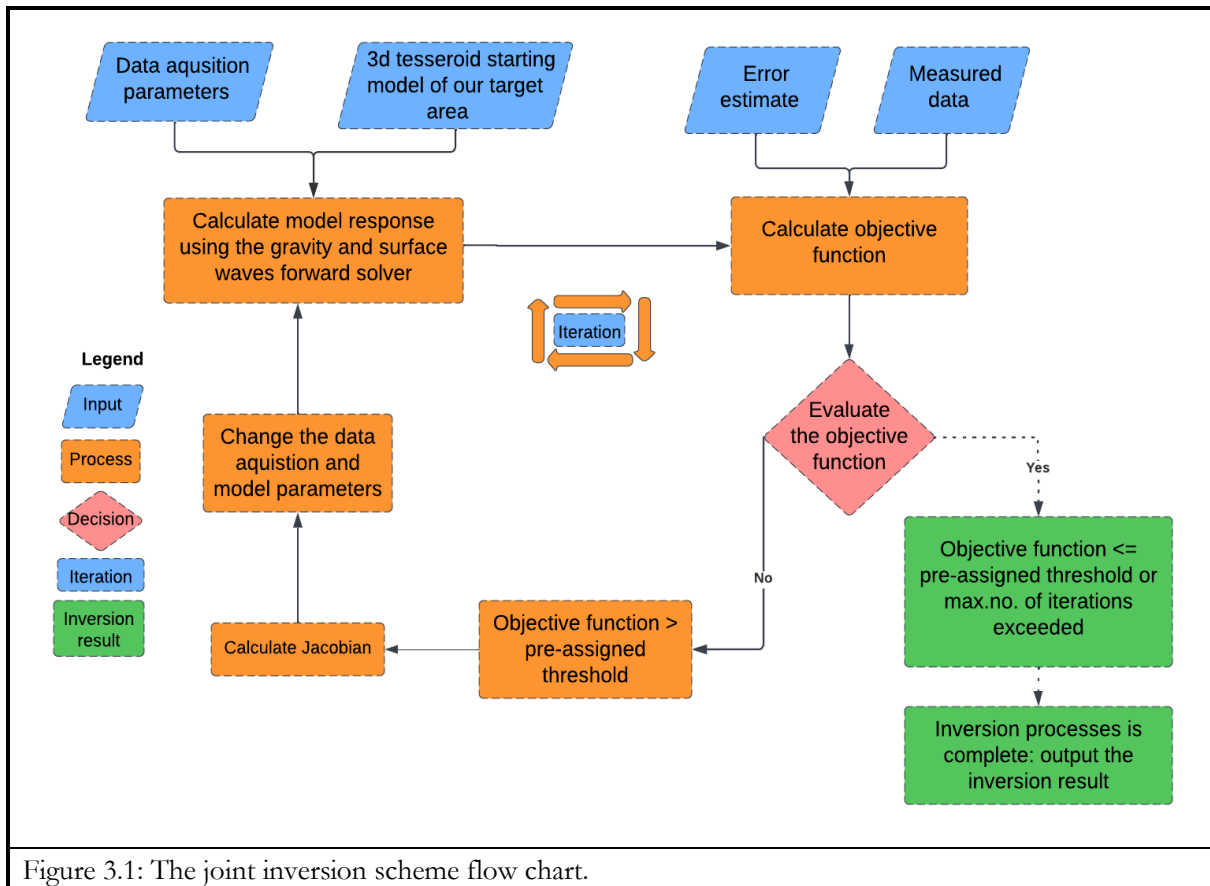


Figure 3.1: The joint inversion scheme flow chart.

#### 3.1.1. Forward Solver and Sensitivity Kernel

The forward solvers are constructed to deal with three-dimensional models that take the form of tesseroids and use spherical coordinates (Figure 3.2). The advantage of using tesseroid model is that it considers the

Earth's spherical curvature for areas with spatial coverage larger than  $10 * 10$  degrees, like Botswana (Uieda et al., 2016). For the forward solver, the tesserooids model consists of four different physical parameters, which are as follows: 1) The velocity of the S-wave ( $V_s$  in km/s), 2) The velocity of the P-wave ( $V_p$  in km/s), 3) density ( $\rho$  in  $gm/m^3$ ), and 4) density anomaly (expressed in  $kg/m^3$ ). The  $V_s$ ,  $V_p$ , and  $\rho$  are used in the forward solver for the group and phase velocity calculations, whereas the density anomaly is calculated using the difference between the density of the used model and a pre-defined reference background average density model; and was mainly utilized in the gravity forward calculation. The velocity ( $V_s$  and  $V_p$ ) and density are coupled to each other using the Brocher (2005) velocity and density relation as shown in the equation below (Equations 3.1 and 3.2).

The first equation (Equation 3.1) expresses the Brocher relation between  $V_p$  and  $V_s$  in which the  $V_p$  velocity is expressed as a function of  $V_s$ .

$$V_p(km/sec) = 0.9409 + 2.0947V_s - 0.8206V_s^2 + 0.2683V_s^3 - 0.025V_s^4 \quad \text{Equation 3.1}$$

Equation 3.2 is the Brocher polynomial regression fit to the existing density and  $V_p$  values which the density is described as a function of  $V_p$  and is considered to be valid for  $V_p$  between 1.5 and 8.5 km/sec (Brocher, 2005).

$$\rho(g/cm)^3 = 1.6612V_p - 0.4721V_p^2 + 0.0671V_p^3 - 0.0043V_p^4 + 0.000106V_p^5 \quad \text{Equation 3.2}$$

The forward solver is parallelized in Python and optimized to forward map from the model domain to the data domain using the coupled model parameters to calculate the gravity (using the density anomaly model parameter) and surface wave data (using  $V_p$ ,  $V_s$ , and density model parameters), as shown in Equation 3.3. The scalability performance of the 3D forward solvers is evaluated using 1,2,4,8,16, and 32 processors on Dell Tower 7910 machine with 196 GB RAM and 48 Xeon Gold 3.2GHz processors, as shown in Figure 3.3 in which the gravity and surface wave solvers show a scalable performance up to 32 CPUs.

$$\begin{pmatrix} K_{grp} \\ K_{phs} \\ K_{gz} \\ K_{gzz} \\ K_{gxx} \\ K_{gyy} \\ K_{gxy} \\ K_{gxx} \\ K_{gyz} \end{pmatrix}_{i \times j} * (m_{vs \rightarrow vp \rightarrow rho})_{j \times 1} = \begin{pmatrix} d_{grp} \\ d_{phs} \\ d_{gz} \\ d_{gzz} \\ d_{gxx} \\ d_{gyy} \\ d_{gxy} \\ d_{gxx} \\ d_{gyz} \end{pmatrix}_{i \times 1} \quad \text{Equation 3.3}$$

Where:

$K_{par}$  is the sensitivity kernel to map from the model domain to the data domain (par is the data type; either grp (group velocity), phs (phase velocity), and  $g_x$  (the gravity component)).

$m_{par}$  is the coupled model parameter.

$d_{obs}$  is the calculated gravity and surface wave data.

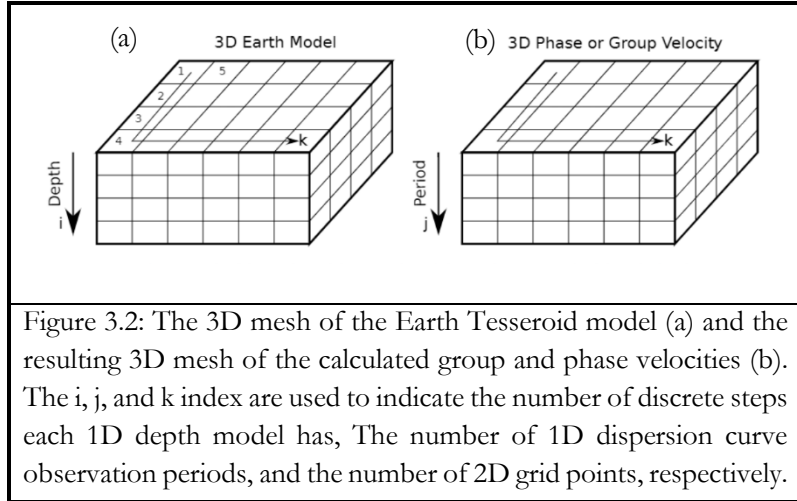
### 3.1.1.1. Gravity Forward Solver and Sensitivity Kernel

The vertical gravitational field and six-component gradients are calculated using a modified version of the Tesseroids function (Uieda et al., 2016) written in Python 3 and capable of parallel computations. Here, the joint inversion approach uses the tesseroid spherical geometric element to calculate the total gravitational field above the Earth surface and the gravity gradients at the GOCE satellite altitudes of 225 km. The gravity forward solver uses a fixed geometry of the tesseroid model that does not change in the whole inversion

scheme and saves the sensitivity matrix for fast calculation of the forward signal during the inversion process. This approach of saving the sensitivity matrix help to reduce the computing time of the joint inversion scheme for regional or continental scale models. However, the size of the sensitivity kernel would exponentially increase with increasing the 3D Earth model resolution and the gravity computational grid.

### 3.1.1.2. Rayleigh Wave Fundamental Mode Group and Phase Velocities Forward Solver and Sensitivity Kernel

The Rayleigh wave fundamental mode group and phase velocities 3D forward solver is basically a 1D solver which iterates over the 2D grid points to generate a 3D group and phase velocity measurements. The 1D forward solver uses a 1D model of  $V_p$ ,  $V_s$ , and density to calculate the group and phase velocity dispersion measurements. Figure 3.2 a & b shows how the Surface Wave Forward Solver operates in 1D-depth (i) over the 2D grid points (k) of the 3D Earth model and the calculated surface wave data (group or phase velocities) in the 3D model.



The early implementation of the joint inversion algorithm was using the central finite difference scheme which was operated by iterating through each cell of the 3D model to automatically calculate the Jacobian matrix of the group and phase velocity measurements. However, this makes the computational time exponentially increase with the increase of the model size and resolution e.g., high resolution continental scale modelling. In this work, the performance of the joint inversion scheme was improved by implementing the calculation of the Jacobian matrix through a 1D central finite difference scheme that loops through the 2D grid points to calculate the sparse 3D sensitivity kernel (Equation 3.4) instead of iterating through each cell of the 3d models (Figure 3.2, A) that significantly reduces the computational time to calculate the sensitivity kernel of the surface wave data.

Equation 3.5 below shows the mathematical representation of the sparse optimized Jacobian matrix used in the joint inversion ( $s_{ji}$ ) represented in the forward modelling operation as it is multiplied by the 1D depth model ( $m_i$ ) at each 2D grid point to give the calculated data ( $d_j$ ).

$$\begin{bmatrix}
 \begin{bmatrix} s_{11} & s_{12} & \dots & s_{1i} \\ s_{21} & s_{22} & \dots & s_{2i} \\ \vdots & \vdots & \ddots & \vdots \\ s_{j1} & s_{j2} & \dots & s_{ji} \end{bmatrix} & 0 & \dots & 0 \\
 0 & \begin{bmatrix} s_{11} & s_{12} & \dots & s_{1i} \\ s_{21} & s_{22} & \dots & s_{2i} \\ \vdots & \vdots & \ddots & \vdots \\ s_{j1} & s_{j2} & \dots & s_{ji} \end{bmatrix} & \dots & 0 \\
 \vdots & \vdots & \ddots & \vdots & \dots & \vdots \\
 0 & 0 & \dots & \begin{bmatrix} s_{11} & s_{12} & \dots & s_{1i} \\ s_{21} & s_{22} & \dots & s_{2i} \\ \vdots & \vdots & \ddots & \vdots \\ s_{j1} & s_{j2} & \dots & s_{ji} \end{bmatrix} & \dots & \vdots
 \end{bmatrix}
 \times
 \begin{bmatrix} m_1 \\ m_2 \\ \vdots \\ m_i \end{bmatrix}_1
 \times
 \begin{bmatrix} m_1 \\ m_2 \\ \vdots \\ m_i \end{bmatrix}_2
 \times
 \dots
 \times
 \begin{bmatrix} m_1 \\ m_2 \\ \vdots \\ m_i \end{bmatrix}_k
 =
 \begin{bmatrix} d_1 \\ d_2 \\ \vdots \\ d_j \end{bmatrix}_1
 \times
 \begin{bmatrix} d_1 \\ d_2 \\ \vdots \\ d_j \end{bmatrix}_2
 \times
 \dots
 \times
 \begin{bmatrix} d_1 \\ d_2 \\ \vdots \\ d_i \end{bmatrix}_k$$

Equation 3.4

Where (see Figure 3.2 for further illustration of the indices):

$s_{ji}$  represents the Jacobian matrix determined at each grid point using finite difference approximation.

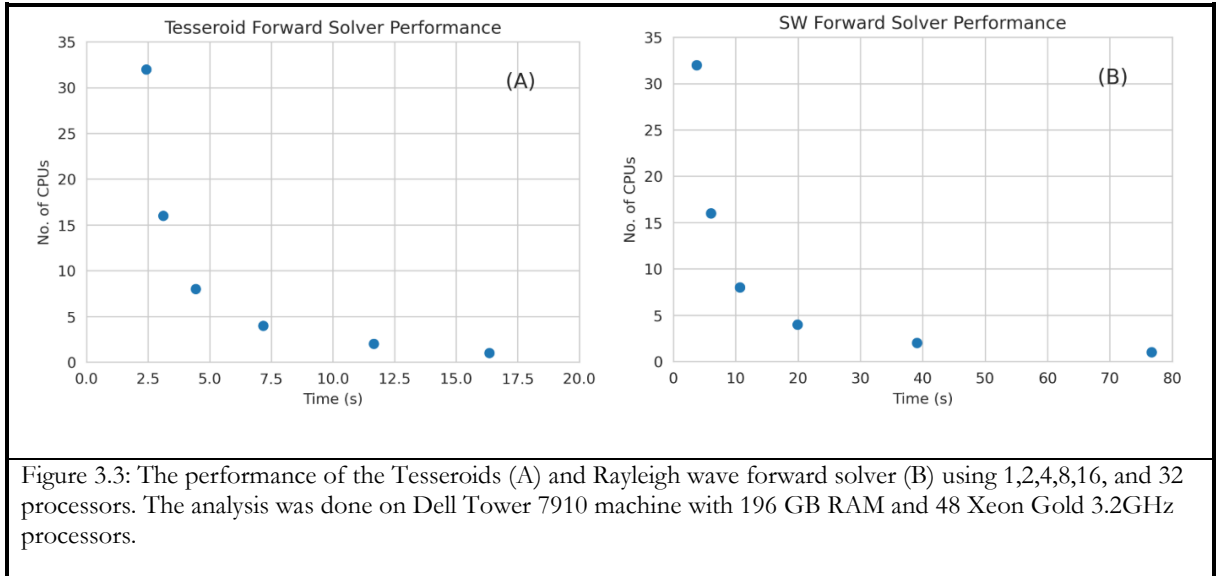
$m_i$  represents the model parameter in a 1-D depth per grid point.

$d_i$  represents the calculated data obtained from the surface wave forward solver.

$k$  represents the number of 2D grid points.

$i$  represents the number of discretized steps in each 1D depth model.

$j$  represents the number of observation periods in each 1D dispersion curve.



### 3.1.2. Inversion Formulation

The joint inversion scheme is designed to minimize the objective function described in equation 3.6 below. The objective function consists of four terms that define the surface wave data misfit, the gravity data misfit, the smoothness constraints, and the model perturbation that describes how far the inverted model can vary from a predefined starting model.

The main aim of the inversion process is to minimize the objective function by controlling the balanced contribution of the different data sets controlled by the weighting parameters in equation 3.6 below. To get the optimal result from the joint inversion, we need to reduce the objective function by minimizing the data misfit, generating subsurface models with geologically acceptable smoothing, and at the same time having an acceptable level of variation from the starting model.

$$\begin{aligned} \phi = & \|[g(m) - d_{obs}]_{sw} * w_{sw}\|_2^2 + \|[g(m) - d_{obs}]_{gv} * w_{gv}\|_2^2 + \left\| \left[ \frac{\partial m}{\partial x} + \frac{\partial m}{\partial y} + \frac{\partial m}{\partial z} \right] * \alpha \right\|_2^2 + \\ & \|[m - m_0] * \beta\|_2^2 \end{aligned} \quad \text{Equation 3.6}$$

Where:

- The first term describes Rayleigh wave dispersion data misfit where  $g(m)$  is the forward solver,  $d_{obs}$  is the observed data, and  $w_{sw}$  is the weight of the surface wave data
- The second term describes the gravity data misfit where  $g(m)$  is the gravity forward solver,  $d_{obs}$  is the observed gravity data, and  $w_{gv}$  is the assigned weight to the gravity data.
- The subscript  $sw$  and  $gv$  in the first and second terms indicate the surface wave and gravity part of the misfit term.
- The third term is a model regularization that describes directional smoothness in  $x$ ,  $y$ , and  $z$  directions with weighting value represented by  $\alpha$  along  $x$ ,  $y$ , and  $z$  directions.
- The last term controls the degree to which the inversion result ( $m$ ) can vary from the starting model ( $m_0$ ) with the corresponding damping weight to the background model represented by  $\beta$  (Fadel, 2018, P.137).

The inversion scheme employs an iterative damped least-square optimization strategy based on the Levenberg-Marquardt algorithm (More, 1978) to reduce the joint inversion misfit function. The inversion scheme uses a pre-defined Jacobian matrix described in subsection 3.1.1 (Fadel, 2018). The iteration of the joint inversion process will continue until either one of the following conditions is satisfied: 1) the number of iterations reaches a predefined threshold, or 2) the misfit function falls below a predetermined threshold. The shear wave velocity is the primary focus of the inversion procedure that is always coupled to density and  $V_p$  using the Brocher relation of velocity and density (Brocher, 2005). It is important to mention that the joint inversion method has the capability to honour the topography at any desired vertical resolution but on the expense of the computational time.

## 3.2. Joint Inversion Testing and Implementation

The joint inversion scheme described above is tested and implemented in three phases: the first phase conducts synthetic method test using a simple geologic model to understand the efficiency and scalability of the method after method performance improvement was conducted. The second phase uses a complex synthetic geologic model mimicking Botswana geology to understand the applicability of the method to real world scenarios and thereby understand the influence of the different model parameters in the inversion processes. The final phases conducted was real data application of the method using satellite gravity and seismic surface wave measurements of Botswana.

### 3.2.1. First Phase: Simple geologic model synthetic test

In this synthetic test of the joint inversion method, the inversion scheme is implemented using three scenarios in which varying combinations of the datasets were utilized. The **first scenario** uses the gravity data only in the inversion. In this scenario, both the vertical gravity field ( $g_z$ ) and the six components of gravity gradient data are used in a different configuration to understand the added value of the different gravity components for the subsurface density modelling. Those configurations are inverting 1)  $g_z$  only, 2)  $g_{zz} + g_{xx} + g_{yy} + g_{xy} + g_{xz} + g_{yz}$ , 3)  $g_z + g_{zz}$ , and finally  $g_z + g_{zz} + g_{xx} + g_{yy} + g_{xy} + g_{xz} + g_{yz}$ . The **second scenario** uses the surface wave-only data for velocity modelling. In this scenario, the fundamental mode Rayleigh wave group and phase velocity are used in the inversion processes. On the other hand, the **third scenario** conducts the joint inversion of the surface wave and gravity data mentioned above simultaneously for subsurface velocity and density modelling. In particular, the main interest was to assess the efficiency of the joint inversion approach in terms of computational cost, scalability, and how the joint inversion performs compared to single data inversions. Therefore, by determining and understanding the added value

of the different data sets for subsurface density and velocity modelling, it is possible to analyze to what extent our model improved in retrieving subsurface structures.

### 3.2.2. Second Phase: Complex geologic model synthetic test

In this stage of the synthetic method test, a more complicated model that mimics the geology of Botswana was utilized to assess the efficiency of the joint inversion approach in a manner that is more realistic to the real world. Therefore, in a similar manner conducted in a simple synthetic method test, the inversion was conducted in three scenarios but with less configuration of data set than phase-1 method test. Those are, **scenario-1**: gravity only inversion using  $gz + gall$  gravity data to recover density, **scenario-2**: surface wave only inversion using the group and phase velocity dispersion data to recover velocity and **scenario-3**: joint inversion of gravity ( $gz + gall$ ) and Rayleigh wave group and phase velocity dispersion data for both density and velocity estimation. The 3D starting model depicted in Appendix 1, Figure 7.14, which was interpolated from the AK135 model (Kennett et al., 1995) was used as the starting model for the inversion processes.

### 3.2.3. Third Phase: Real data application of the joint inversion approach

The third phase of real data application was conducted by jointly inverting the real data measurements of Botswana described in section 2.2.

### 3.2.4. Parameter Estimation

The inversion is controlled by three governing parameters: data weighting, model smoothness, and damping weight to background model.

#### 3.2.4.1. Data Weighting

The data obtained from the forward solver for the synthetic case and observed data for the real data application should be weighted to balance the contribution of each data set in the joint inversion. The data weighting is part of the first and second components of the objective function for the surface waves ( $w_{sw}$ ) and gravity data ( $w_{gv}$ ), respectively, as described in Equation 3.6. The joint inversion scheme was designed so that the gravity data (total field and gradients) and the surface wave data (group and phase velocity) have equal contributions to the data misfit portion of the joint inversion so that it overcomes overfit of a particular data set over another (Syracuse et al., 2017). The data misfit indicates the degree to which the calculated data from the predicted model agrees with the measured data (Cockett et al., 2015). Therefore, the proper weighting of the data set needs to be conducted for both gravity and Rayleigh wave phase and group velocity data to get an optimal model from the contribution of both data sets. The inversion scheme uses the inverse of the error covariance as a weight normalization parameter based on the error floor defined to guarantee the balanced contribution of the datasets, given the different ranges of amplitudes in the data set. Considering the challenge of estimating the error in geophysical inversion, a 5% error floor was assigned, commonly used in joint inversion applications (Julià et al., 2000). As a result, a small misfit value was desired to have a good model that could fit the observed data to the level of the error floor. Therefore, finding a model with a data misfit close to the noise level of the data added and assigned threshold misfit criteria is essential neither to fit noises nor loose structures by overfitting and underfitting, respectively. After automatically adjusting the weighting of all datasets, another user customized weighting is adapted to manually control the contribution of each dataset when needed based on trial and errors.

#### 3.2.4.2. Designing Model Smoothness and Damping weight

The third and fourth components of equation 3.6 are terms that control the smoothness and model norm of the inversion output, respectively (Fadel, 2018). The first one is a model smoothness parameter that controls the directional smoothness of the inverted model in x, y, and z directions (Fadel, 2018). On the other hand, the latter term is damping weight to the background model, that controls how much the model can vary from a pre-defined background model; in this case the starting model was used as the background

model for the damping. Therefore, using the two terms mentioned, it is possible to control how the output model looks and to what degree the inverted model is allowed to vary from the starting model. Several testing of the inversion processes with different values of directional derivatives in x, y, and z direction and weighting of the damping to the background model was conducted to make a balanced choice of a parameter that allows retrieval of a useful, realistic Earth model that properly fit the dataset used. Therefore, the specific choices of the model norm parameters were made based on the visual comparison and misfit analysis of the inversion result in reference to the true model and original data set, respectively. A summary of the model norm parameters together with the data weighting values used for the synthetic case and real data application, are presented in Appendix 1, 2 & 3, Table 7.1, 7.2 & 7.3, respectively.

Therefore, after setting up all the parameters, the inversion process was conducted iteratively using the synthetic data generated or the real data until the desired Earth model fits the data and has obtained an acceptable model norm. The number of iterations and the objective function termination threshold (which includes data misfit and model norms) were adjusted to guarantee the minimum number of iterations while achieving the optimum objective function reduction. As a result, the number of iterations was kept to 20 for first phase of simple model synthetic method test and 150 for second phase complex model method test and real data application, and a termination threshold of 0.01 % of the starting misfit was set to let the inversion minimize the objective function as low as possible within the available number of iterations. The final inversion results, which are close to the true model and reproduce the data set that gives a low misfit value, were considered the final model for the inversion.

### **3.2.5. Model Visualization and Assessment**

The final phase of the methodology is to analyse and interpret the model for both the synthetic test and real data application. The root mean square error (RMSE) criteria of the inverted model misfit per depth in comparison to the true model and data misfit are analysed to understand the level of recovery of the amplitude of the anomalies and assess the level of data fit, respectively. The density and velocity model from the inversion results are assessed and visualized using plotting functions in Python and PyGMT (Uieda and Wessel, 2019). A plane view of the model depth slice and vertical cross-section was used to visualize the inverted models and to assess evaluating the goodness of the recovered models. The misfit analysis between the inverted models' responses and the synthetic generated data was done to assess the performance of the final inversion results toward data fitting. Similarly, for the real data application, the plan view and cross-sectional view are used to interpret the subsurface structure and address the tectonic question of Botswana mentioned in chapter 1. Furthermore, a comparison of the inverted model with the true model for the synthetic case and the comparison of the inverted model with velocity and gravity investigation of Botswana from the literature were used to evaluate the final inverted model and better understand the tectonic settings of the study area and confirm or reject the hypothesis given on the tectonics of Botswana.

In the subsequent chapters, the detail description of computing-demanding synthetic test and real data application of the joint inversion approach conducted is presented. The three phases of method application are presented in three different chapters: phase-1 method test using a synthetic model with simple geological structures (chapter 4), phase-2 method test using a synthetic model with complex geological structures by mimicking Botswana geology (chapter 5) and real data application of the joint inversion on Botswana (chapter 6). Therefore, each chapter includes a description of the synthetic test design used to implement the joint inversion approach; the inversion results, and discussions of the final model evaluation and analysis performed to answer the research questions.

## 4. SYNTHETIC METHOD TEST USING A SIMPLE GEOLOGIC MODEL

### 4.1. Introduction

This chapter presents the first phase of method test using a simple synthetic geologic model to understand the efficiency of the method after method performance improvement was conducted. This phase of method test will help us also understand the influence of the inversion parameters for the second phase of method test conducted using a more complex geologic model described in chapter 5 and even for later stage real data application of the joint inversion approach presented in chapter 6. Therefore, this chapter will present the description of the synthetic test design conducted for the first phase of method test using synthetic data (section 4.2), including the description of the data sets, model parameters, and the inversion process conducted. Description of the inversion results and misfit analysis (section 4.3) and finally followed by an overview of the discussion on the synthetic test result and method performance assessment (section 4.4).

### 4.2. Synthetic Model Design for Joint Inversion Implementation

I will here discuss the overall framework of the synthetic test design conducted for the joint inversion implementation. The synthetic test design starts by adjusting the model set-up of the starting and true model for the inversion (section 4.2.1) and a description of the data set from the forward modelling (section 4.2.2).

#### 4.2.1. Model Setup

##### 4.2.1.1. Setting up the Starting Model

The first step in the inverse problem is to specify the discretization of the Earth model (Li and Oldenburg, 1995). Here, the tesseroid Earth model was discretized into a regular grid of spherical geometric elements. The model has a dimension of 0-16 degrees in E-W and 0-16 degrees N-S, and 0-50 km in the vertical directions using cell sizes of 1\*1 degrees and 5 km in x, y, and z, respectively. Using the discretised Earth model, the so-called starting model was constructed from the average 1D velocity models shown in Figure 4.1. It has the same velocity structure as the 1D average shear wave but repeated over the 2D grid points to form the 3D starting model. The average 1D velocity model was derived from the global AK135 reference velocity model (Kennett et al., 1995) using linear interpolation techniques. The interpolation was conducted at 5 km intervals to 50 km depth level of the Earth model. Figure 7.1 shows the 3D starting velocity model used for the inversion processes.

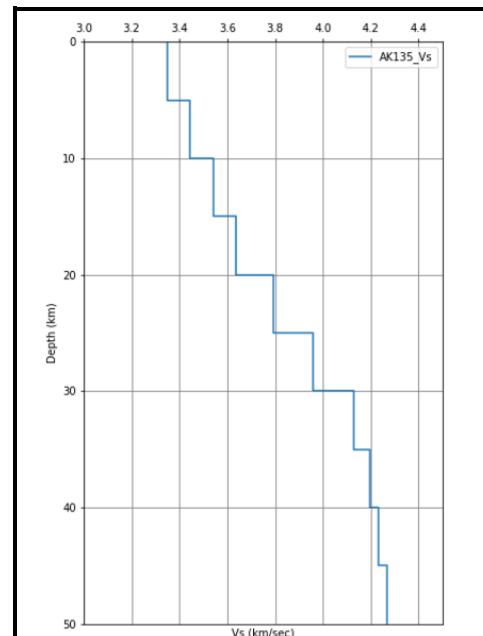
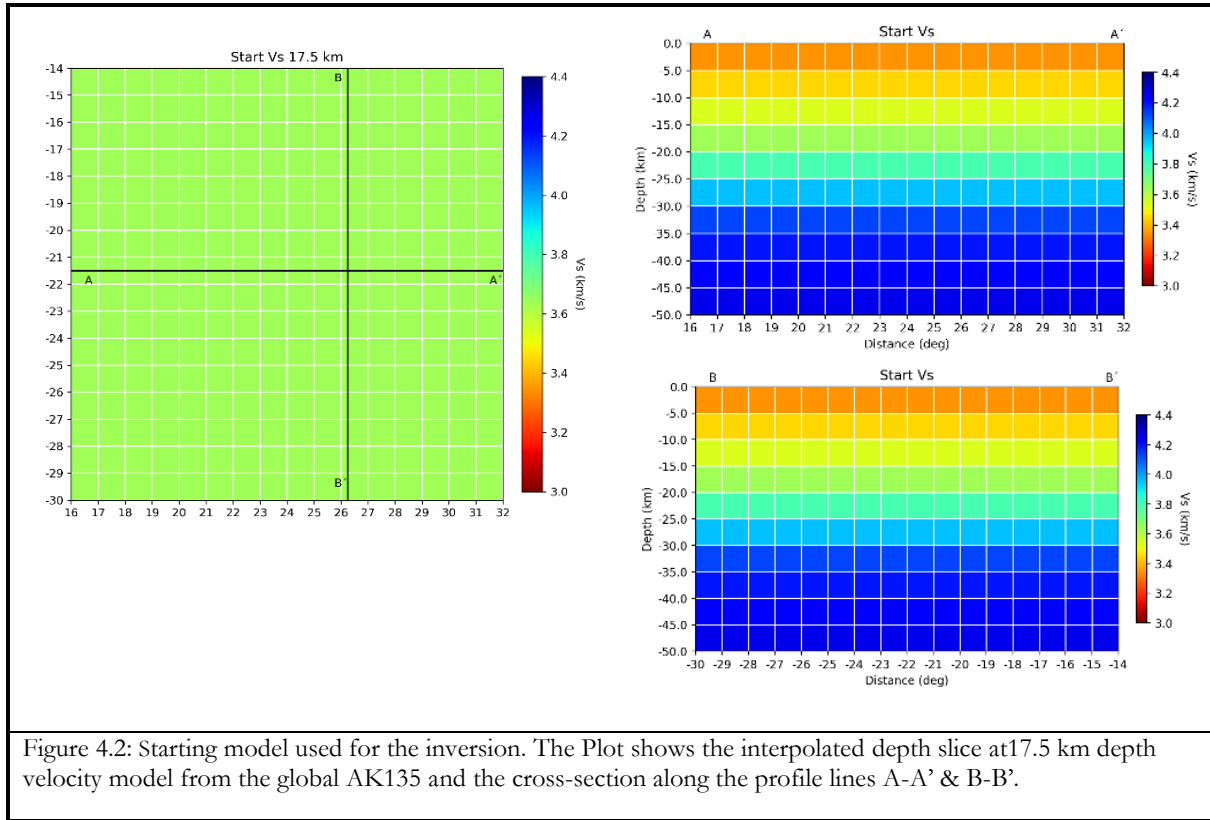


Figure 4.1: Average 1D interpolated velocity from the global Ak135 reference velocity model (Kennett et al., 1995) were used to construct the 3D starting model for the synthetic method test.



#### 4.2.1.2. Setting up the True Model

The so-called true Earth models (Figure 4.3) were constructed by inserting two anomaly bodies with positive and negative anomaly values for velocity and density at the center of the starting model to create a contrast from the background value. The velocity and density anomaly has  $\sim 10\%$  positive and negative deviation from the average background values. The two anomalies have a 2-degree lateral extent spanning from a depth of 10 km to 30 km in the model's background. Therefore, the density and velocity true model (Figure 4.3 a & b) were used for the forward computation of the fundamental mode Rayleigh wave group and phase velocity dispersion measurements. On the other hand, the density contrast model calculated using the difference between the true model and the starting (background) model (Figure 4.3 c) was then used for the forward calculation to generate the satellite gravity total field and gradient data, as described in the next section.

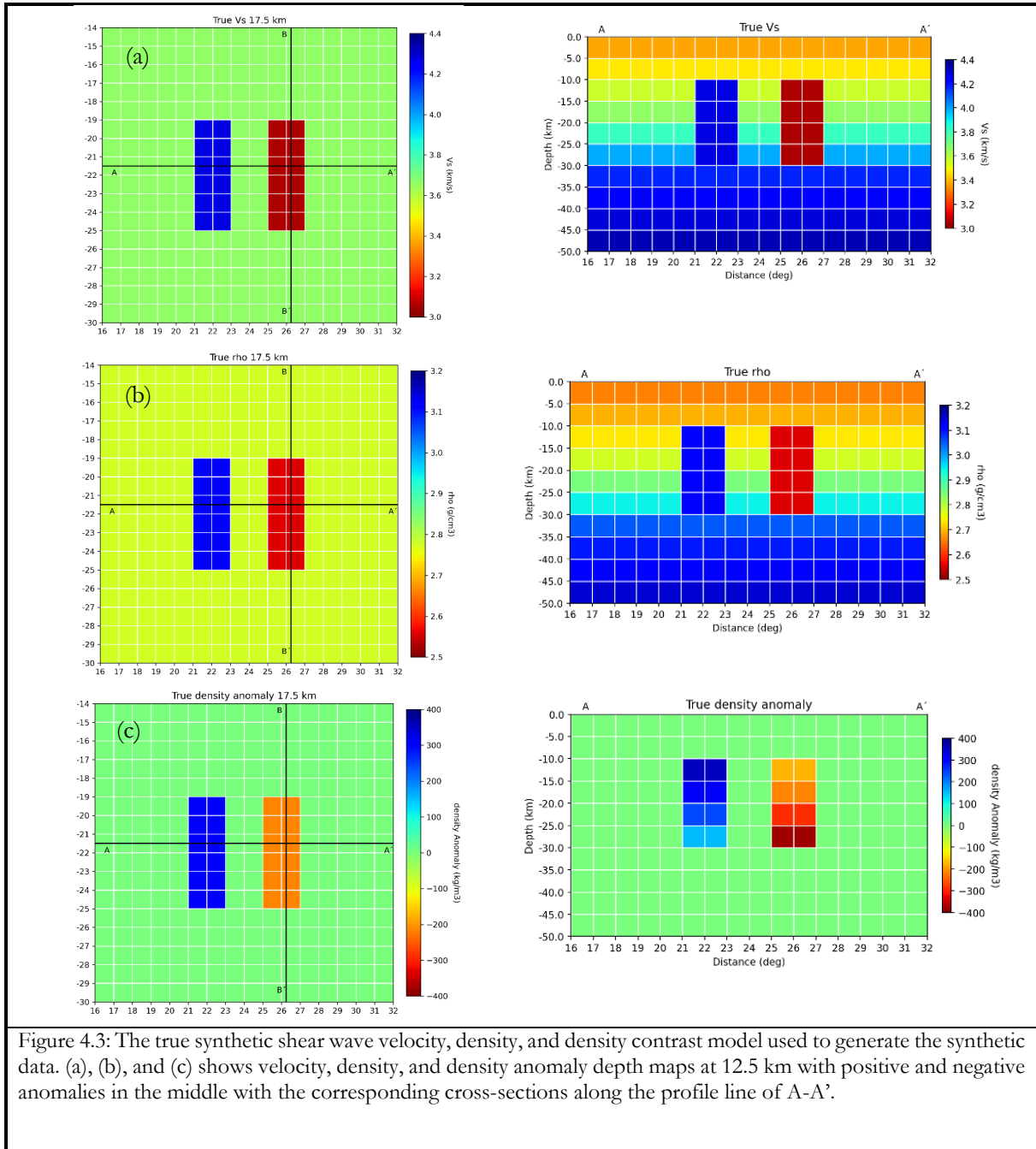


Figure 4.3: The true synthetic shear wave velocity, density, and density contrast model used to generate the synthetic data. (a), (b), and (c) shows velocity, density, and density anomaly depth maps at 12.5 km with positive and negative anomalies in the middle with the corresponding cross-sections along the profile line of A-A'.

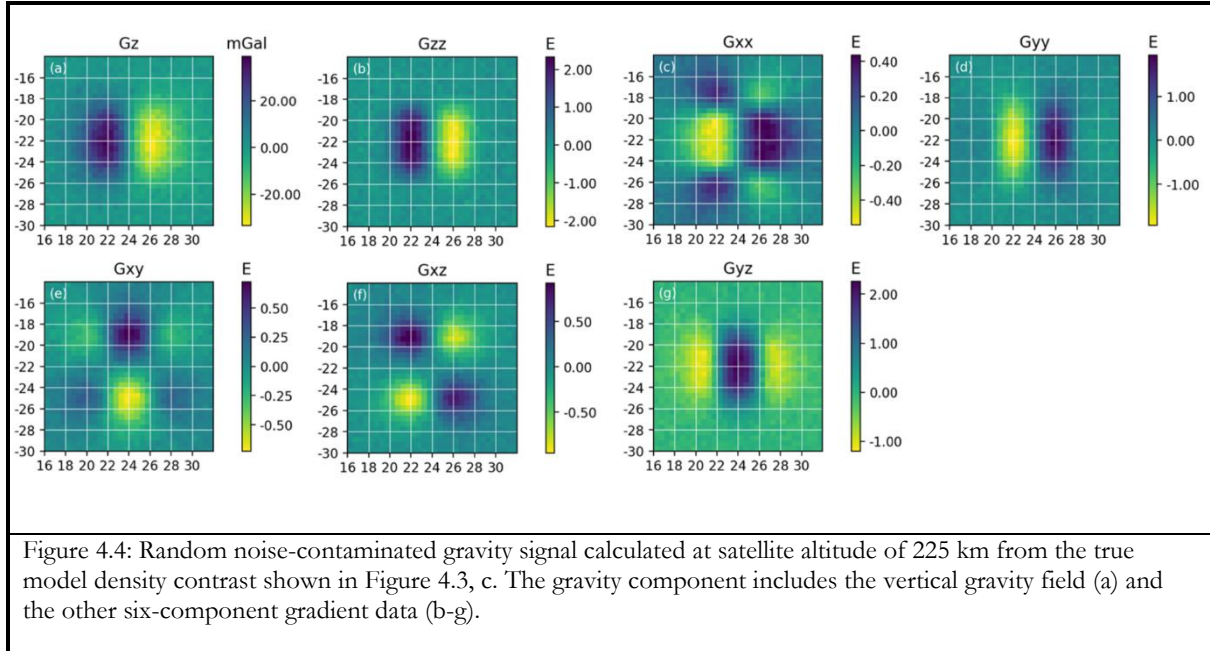
#### 4.2.2. Synthetic Data Forward Modelling (Data set)

In this synthetic test, the constructed true model was used to calculate the gravity and surface wave synthetic data set that will be used later in the inversion processes.

##### 4.2.2.1. Gravity data

Figure 4.4 shows the calculated vertical gravity field ( $g_z$ ) and six components of the GOCE gradient data ( $g_{zz}$ ,  $g_{xx}$ ,  $g_{yy}$ ,  $g_{xy}$ ,  $g_{xz}$ , and  $g_{yz}$ ) obtained from the gravity forward modelling using the synthetic density contrast model shown in Figure 4.3, c). The different gravity gradient data are calculated on a computational grid at a satellite orbital altitude of 225 km to mimic the GOCE gravity gradient data. The computational grid has a spatial extent from 0-16 degrees E-W and 0-16 N-S with a resolution of one degree. In order to mimic a real case scenario, random noise with a normal distribution, zero mean, and standard deviation of 5% of the amplitude ranges of the different components was added to the measured signals. From the different gravity

components, the  $g_z$  and  $g_{zz}$  capture the centre of mass of the anomaly with high and low gravity signals. Since they are the radial component, they contain most of the signals from the density anomaly. The other non-vertical gravity gradient data ( $g_{xx}$ ,  $g_{yy}$ ,  $g_{xy}$ ,  $g_{xz}$  and  $g_{yz}$ ) have different directional sensitivity and shows the anomaly from different angles. The  $g_{xx}$  component, for instance, is most sensitive to north-south oriented objects' boundaries, while the  $g_{yy}$  component is sensitive to east-west oriented boundaries. However, the other component has bidirectional sensitivity.



#### 4.2.2.2. Surface wave data

Figure 4.5 shows the fundamental mode Rayleigh wave group and phase velocity synthetic dispersion measurements obtained using the true model. The surface wave components have their periods calculated at 2 s intervals in the range of 2-50 s in order to guarantee the dominant sensitivity to a depth range of up to 50 km depth. After calculating the surface wave group and phase velocity dispersions data, 5% random noise with a normal distribution and zero mean was applied to the calculated data to simulate the noise level of the real data observations. Figure 4.5 shows the noise-contaminated surface wave dispersion data after it has been incorporated into a tesseroid model with a Z-direction as time, which was employed in the inversion. The group and phase velocity dispersion depicted in Figure 4.5 at 17.5 s and its cross section demonstrates the positive and negative anomalies corresponding to the high and low-velocity measurements.

The relative contribution of depth information to dispersion data can be seen by looking at the variation of the depth sensitivity kernel (Julià et al., 2000). The plot in Figure 4.6 demonstrates the fundamental mode Rayleigh wave group and the phase velocity dispersion determined from the forward solver and its depth sensitivity analysis at 5, 23, 38, and 48 s. Therefore, from the sensitivity plot (Figure 4.6, c & d), it is possible to see the resolving power of the dispersion curve that shows the sampling depth to 50 km. Therefore, the gravity and surface wave data mentioned above are used in the inversion process in different scenarios 1) gravity only, 2) surface wave only, and 3) joint gravity and surface wave, as mentioned in section 3.2.1. In the following section the result and discussion of each inversion scenario are presented.

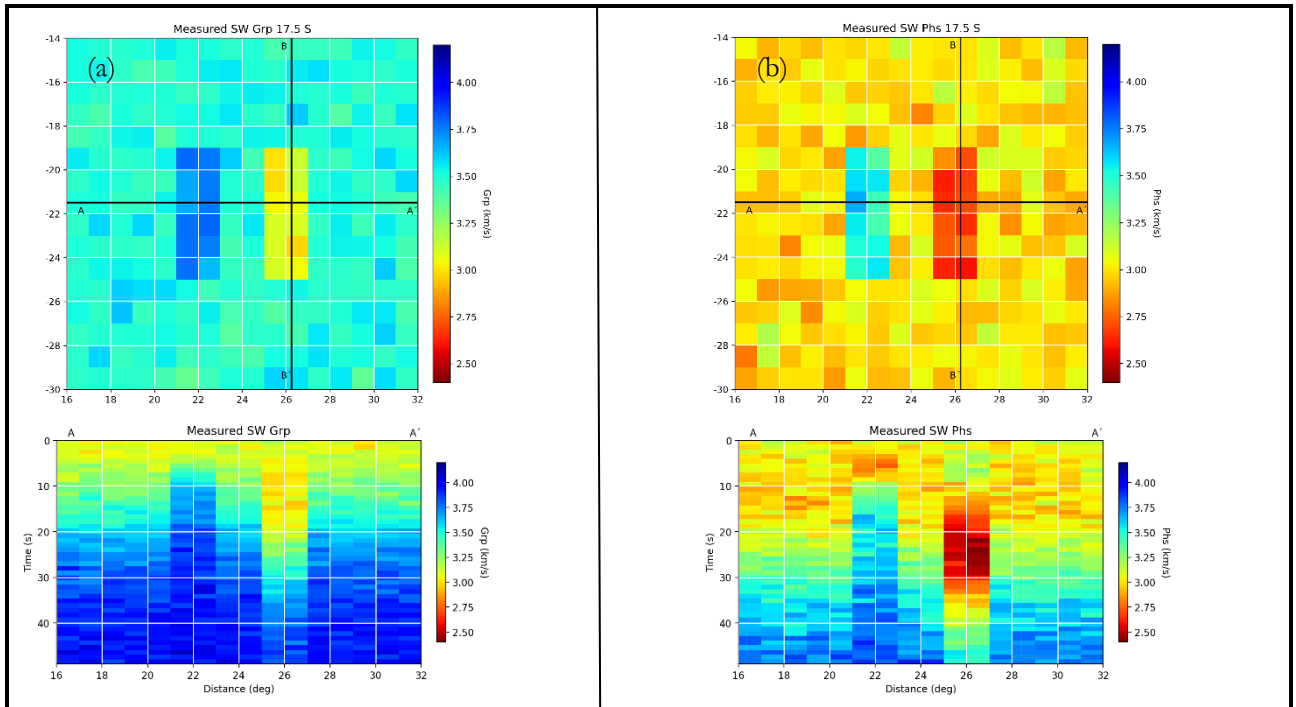


Figure 4.5: The Rayleigh wave group (a) and phase velocity dispersion (b) at 17.5 s period with added random noise to simulate a real case scenario. The Profile lines A-A' depict the corresponding cross-section that shows the period extent of the dispersion curve up to 50 s periods.

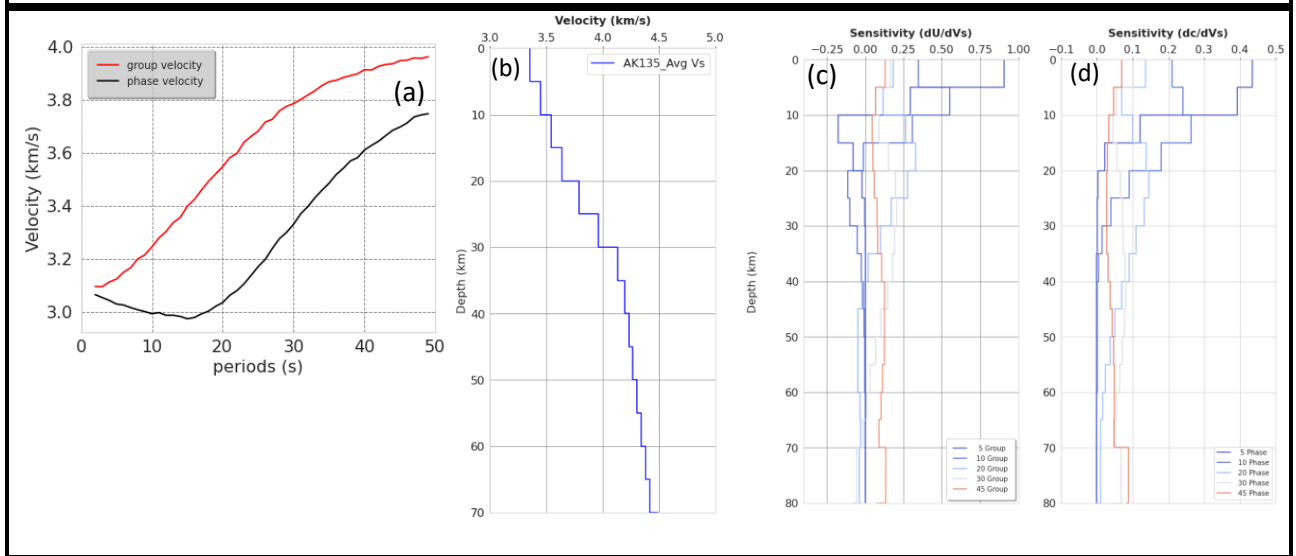


Figure 4.6: The calculated contaminated average group and phase velocity dispersion curves (a) of the 1D shear wave velocity of the true model (b) and its sensitivity analysis at 5, 10, 20, 30 & 45 s intervals, which demonstrates the depth that can be sampled by group and phase velocity up to 50 km and beyond (c and d, respectively).

### 4.3. Inversion Result

In this section, the inversion result from the different scenarios of using the synthetic data is presented. Those scenarios are gravity-only inversion that uses the vertical gravity field ( $g_z$ ) and the six-component of gravity gradient data (scenario 1), surface-wave-only inversion using the fundamental mode Rayleigh wave group and phase velocity data (scenario 2), and finally, a joint inversion of the gravity and surface wave data together (scenario 3).

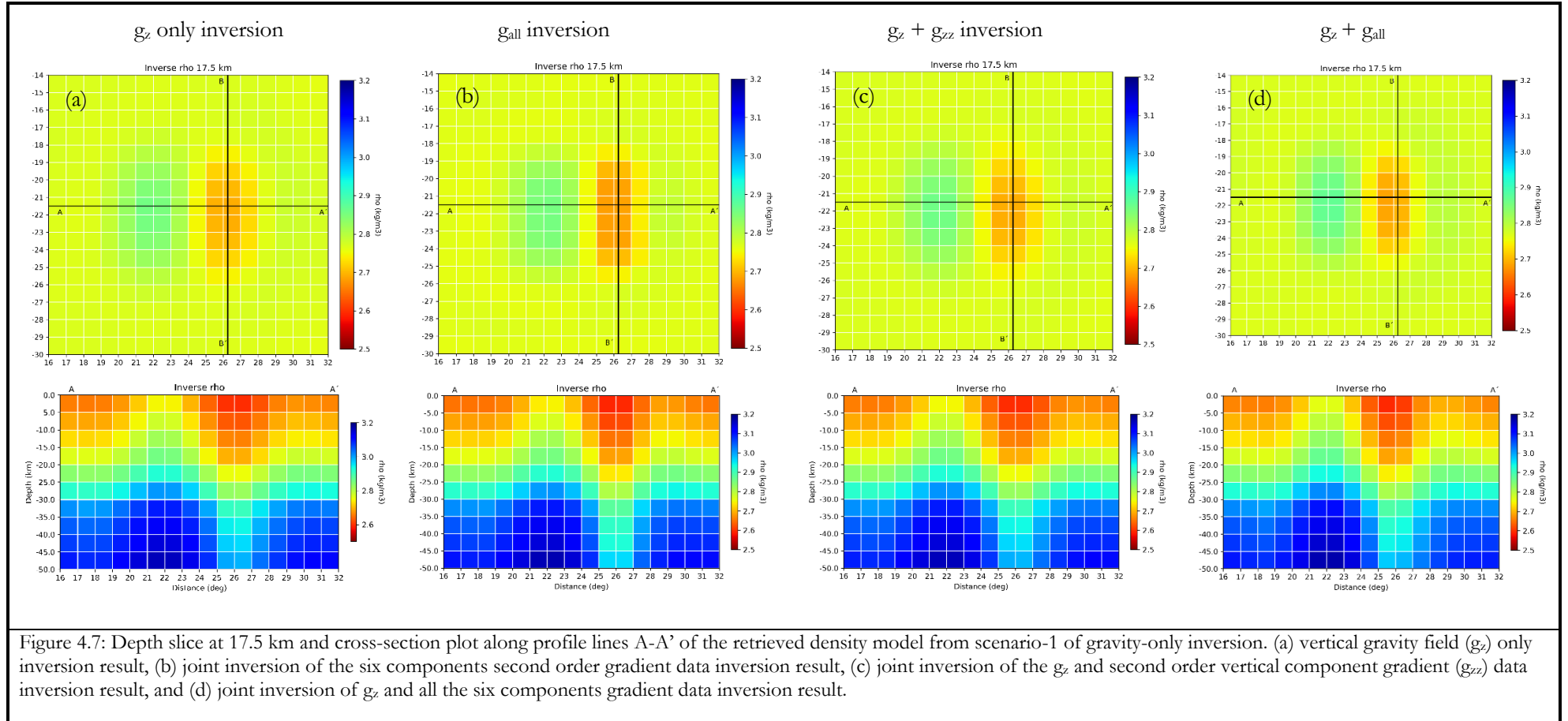
#### 4.3.1. Scenario 1: Gravity-only inversion

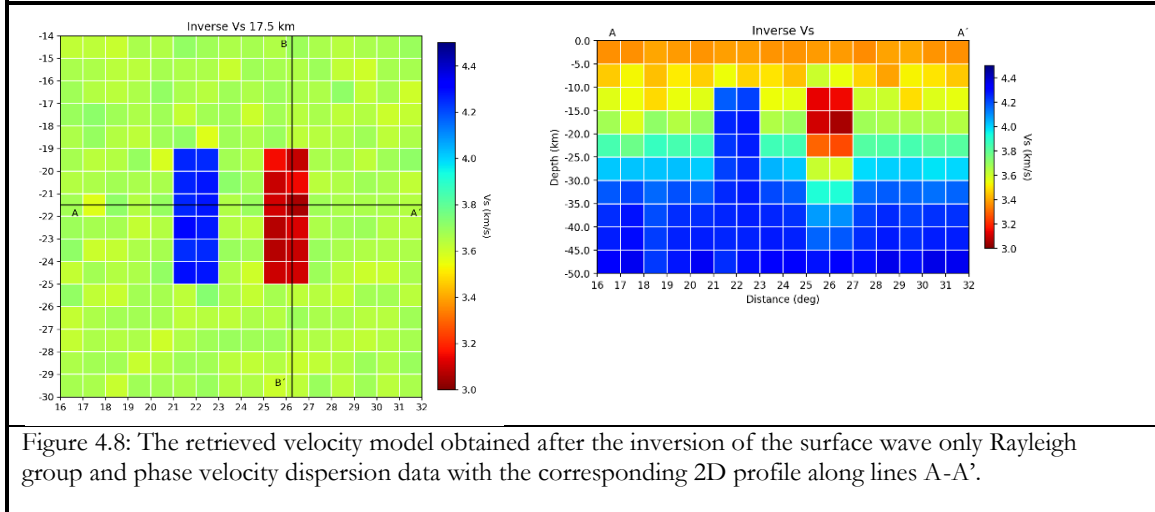
In this scenario of gravity-only inversion, the gravity data only are used to provide information on the subsurface density structure. Comparing the inversion result plotted in Figure 4.7 (a-d), the gravity-only inversion scenario of the synthetic test produces a smooth density model showing a fuzzy boundary of the anomaly from the background. The inversion result demonstrates that the gravity-only inversion does not recover a sharp discontinuity or shape of the anomaly from the background, as it is evident from the depth slice and cross-section plot. Regarding retrieving the anomaly's location, the horizontal depth slice plot at 17.5 km shows the signature of the anomaly at the center of the model, where it shows the spatial location of the two anomalies of high- and low-density values.

The cross-section plot, on the other hand, shows the variation of the density values with depth. However, it shows that the anomalies are shifted to the surface with a smooth transition of density values as it goes deeper into the model (Figure 4.7). This demonstrates the gravity data inversion does not accurately reflect the depth extent of the anomalies as depicted in the true model (Figure 4.3). This is due to the lack of inherent depth resolution of the gravity inversion and the low resolving power of the gravity data to capture the shape and edge of the two anomaly bodies, as presented in Ke et al. (2019). Statistical analysis and comparison of the retrieved model from the different inversion scenarios are presented using RMSE information on model misfit and data misfit analysis.

#### 4.3.2. Scenario 2: Surface wave-only inversion

In this scenario of inversion, the fundamental mode Rayleigh wave group and phase velocity are inverted jointly, targeting the true velocity model depicted in section 4.2.1.2. Because of the sensitivity of surface waves to depth with respect to periods (Julià et al., 2000), it is anticipated that the velocity-depth variation of the anomaly will be resolved from the inversion of surface wave data. Figure 4.8 shows the inverted velocity model depth slice and cross-section plot. From the inversion result, the depth slice plot at 17.5 km depicts the shape and spatial extent of the positive and negative anomalies. Furthermore, the cross-section plot along profile lines A-A' demonstrates the depth-velocity variation of the inverted velocity model, and it shows that the top boundary of the positive and negative anomaly at 10 km depth is clearly visible from the background values. There is; however, a continuous change observed from the lower edge of the anomalies (after 25 km depth) to the deepest layer of the inverted model towards the background values. This is because of the difference between the values allocated to the anomaly compared to the background model that counteracts the effect of the vertical smoothness constraints applied during the inversion.





### 4.3.3. Scenario 3: Joint inversion of Rayleigh wave group and phase velocity with the gravity measurements

This section will cover the third scenario of the inversion processes, which includes the joint inversion of the Rayleigh wave group and phase velocity dispersion with gravity data. Therefore, I used the same data as I used for the separate data set inversions mentioned above with their corresponding additional amount of noise added in. Two ways of integrating both data sets were examined here. The first case combines the Rayleigh wave group and phase velocity components of the surface waves with the vertical gravity field ( $g_z$ ). The second case combines the surface wave group and phase velocities, the vertical gravity field, and six components of the gravity gradient data.

#### 4.3.3.1. Surface wave and $g_z$ gravity data inversion

Figure 4.9 shows the inverted velocity and density model from the surface wave (group and phase velocity dispersion) and the vertical gravity field ( $g_z$ ) inversion. From the inversion result, the inverted density model is significantly improved in resolving power compared to gravity-only inversion when we combine the Rayleigh wave group and phase velocity data with the  $g_z$  gravity data. As a result, the anomalies' depth, location, and edges are retrieved more accurately than the gravity data only inversion, as shown in Figure 4.7 and quantified in section 4.4.2. Furthermore, the amplitude of the anomalies is predicted more accurately than the gravity-only inversion. This denotes the requirement to invert gravity data with seismic data to reduce the nature of ambiguity in gravity inversion interpretation. Similarly, the inversion of the surface wave with the  $g_z$  gravity data improves the amplitude retrieval of the velocity anomalies more than the surface wave-only inversion. A more detailed numerical comparison of the inversion result is presented in section 4.4.1 of the misfit analysis.

#### 4.3.3.2. Surface wave plus all gradient data inversion

Figure 4.10 shows the inversion result obtained using all the data sets generated in section 4.2.2. The inversion result demonstrates an improvement in retrieving the shape and extent of the anomaly from the true model compared to the gravity-only inversion for density modelling. Likewise, a close inspection of the result shows that integrating all the gravity gradient data with the surface wave components provided a subtle variation and improvement of the amplitude of the anomalies retrieval than when the gravity field only is used with the surface wave data. The improvement of the inversion result is shown more in the RMSE analysis per layer presented in section 4.4.2

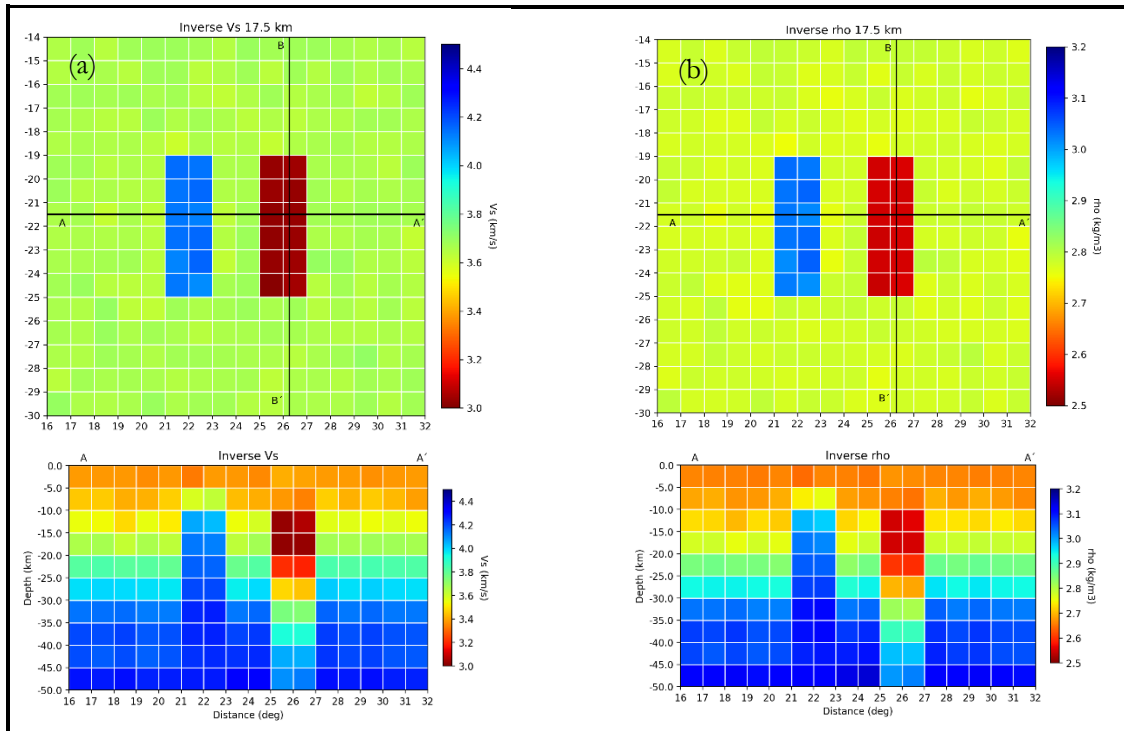


Figure 4.9: Inverted velocity (a) and density (b) model from the inversion of Rayleigh wave group and phase velocity dispersion with the vertical gravity field data ( $g_z$ ). The plot shows the recovered velocity (a) and density (b) model with the corresponding cross-section along lines A-A' for each plot.

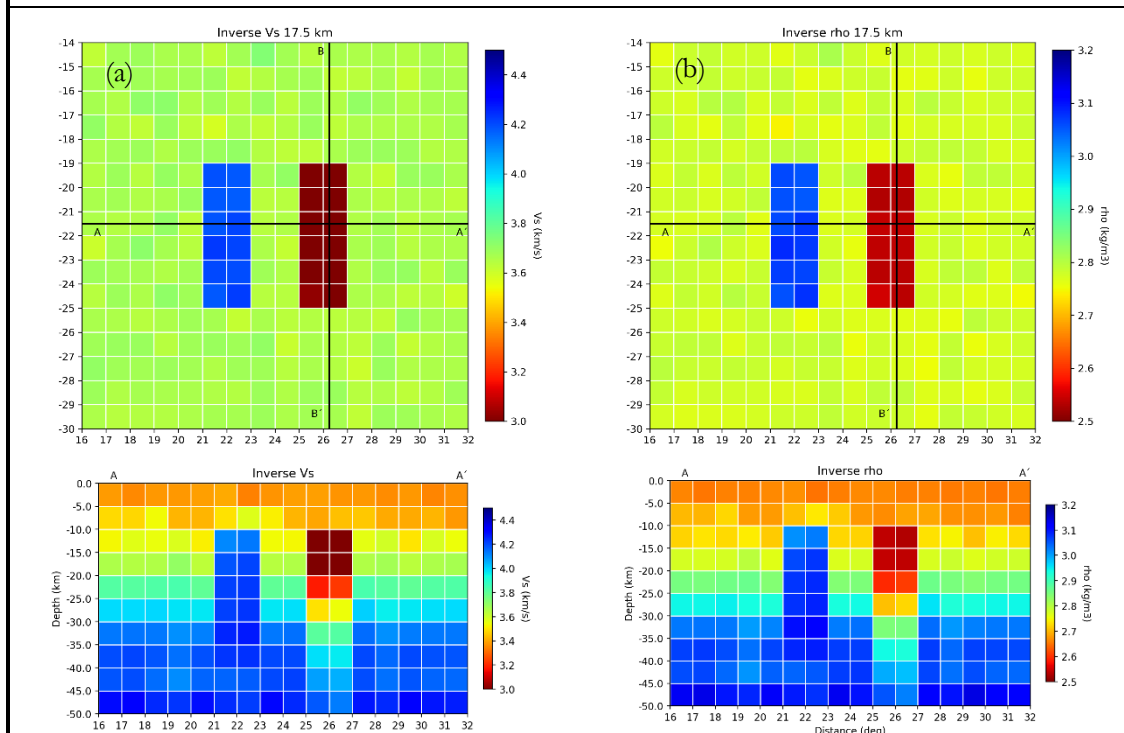


Figure 4.10: Inverted velocity and density model from the joint inversion of the Rayleigh group, and phase velocity dispersion data and all the gravity components ( $g_z + g_{all}$ ). The plot shows the recovered velocity (a) and density (b) model with the corresponding cross-section along lines A-A' for each plot.

#### 4.4. Discussion

In this chapter, the synthetic data generated from the simple synthetic model with known velocity and density anomalies were used to evaluate the method's efficiency in obtaining information from the provided model and the effect of model resolution on the amount of computation time needed to complete the inversion. This is the first step needed to evaluate the method's performance and to apply it to more complex synthetic models, as implemented in chapter 5. Moreover, the test in this chapter can aid in adjusting the inversion parameter for more complex synthetic models and even actual data. Furthermore, the inversion of each data set, both individually and jointly, is carried out to determine the added value of each data set for subsurface density and velocity modeling. This section presents the discussion on the analysis of the inversion result from the different scenarios and configurations of the data set and the joint inversion method performance evaluation.

##### 4.4.1. Evaluation of the Inversion Results

From the perspective of data integration to retrieve the subsurface information, the inversion result from the different data sets was compared and analyzed to determine each data set's added value. Since the gravity data is a potential field and has low sensitivity for density variation with depth (Ke et al., 2019; Paoletti et al., 2016), the inversion result from the gravity data only was expected to be smooth with less contrast to determine the edge of the anomalies depicted in the true model (Figure 4.3). Therefore, it is clear from the inversion result that the gravity field and gravity gradient data inversion resemble each other and lack inherent depth resolution (Figure 4.11, a & b). This is because of the fast decay of the kernel function with increasing depth (Ebbing et al., 2014; Ke et al., 2019). This problem results in the shifting of the anomaly to the surface, as it is shown in the cross-section plots of Figure 4.11, a & b. However, as it is described in different papers (e.g., Bouman et al., 2016; Barnoud et al., 2016; Ebbing et al., 2014; & Ke et al., 2019), the gravity field and gravity gradient data have different depth sensitivity. The  $g_z$  and  $g_{zz}$  components are most sensitive to the mass distribution in the subsurface because they scan the anomaly vertically downward, having the highest amplitude, and give information above the center of the mass. Therefore, at 225 km of satellite height measurement, the  $g_z$  data has a deeper resolving power ( $\sim 40\text{-}60$  km depth) to the lower crust and uppermost mantle than the gradient data (Ebbing et al., 2014). On the other hand, the vertical gradient data  $g_{zz}$  have a more shallow shifted signal power (Bouman et al., 2016; Ebbing et al., 2014) and sensitivity in the middle and lower crustal depths ( $\sim 10\text{-}30$  km depth, Ebbing et al., 2014; Lenczuk et al., 2019). The other non-vertical component gradient data have different directional sensitivity. For example, the  $g_{xz}$ ,  $g_{yz}$ , and  $g_{xy}$  have information about the edge of the anomalies, and the  $g_{xx}$  and  $g_{yy}$  can be able to delineate N-S and E-W aligned structures, respectively (Bouman et al., 2016; Panet et al., 2014). This shows that adding gravity gradient data with a gravity field might help resolve the subsurface density structure at shallow depths from upper to mid-crustal depths.

Comparing the inversion results of the  $g_z$ ,  $g_{\text{all}}$ ,  $g_z + g_{zz}$ , and  $g_z + g_{\text{all}}$  (Figure 4.7) they all show a similar inversion result that they all retrieve a very smooth model that only captures the spatial extent but not the shape of the anomalies indicated in the true model (Figure 4.3). However, the statistical RMSE analysis of the inverted model shown in Table 4.1 shows that the joint inversion of  $g_z$  and  $g_{\text{all}}$  retrieves the density anomaly distributions at shallower depths than the  $g_z$  only. Therefore, the addition of gravity gradient data with the vertical gravity field help to resolve shallow density structure more than the conventional vertical gravity field-only inversion (Ebbing et al., 2014; Lenczuk et al., 2019). This might be due to the different depth sensitivity of the vertical gravity field ( $g_z$ ) and gradient data shallow depth sensitivity, as well as the added value of the gradient data to see the subsurface structure in different directions. This demonstrates the need to use the six gradient components rather than  $g_z$  alone for subsurface density modeling. Therefore, the variable depth sensitivity of the total gravity and gradient data and the distinct angles of observation

from the gradient data might aid in retrieving the subsurface density structure more than using the vertical gravity field alone.

The inversion result obtained from the integration of surface wave data with gravity also shows an improvement in retrieving the subsurface density information than the gravity-only inversion (Figure 4.11). This demonstrates the importance of including surface wave data in a joint inversion with gravity data for density modeling to alleviate the gravity data's restricted depth sensitivity. In contrast, a visual comparison of the inversion result of the retrieved velocity model from the joint inversion of surface wave and gravity components does not demonstrate a significant variation in terms of retrieving the shape and spatial extent of the anomaly from the surface wave only inversion result (Figure 4.12). However, in the RMSE analysis performed for the entire inversion scenarios, the joint inversion of the gravity and surface wave data is shown to increase amplitude retrieval for both density and velocity modelling (Table 4.1 & Table 4.2, respectively). Particularly, the addition of the second-order gradient data is most significant to the shallow part of the model. Therefore, from the finding of the above discussion, it is possible to highlight that the satellite gravity gradient from GOCE might give an added value for lithospheric density and velocity modelling when they are integrated with the total gravity and surface wave data in a joint inversion. Comparison and analysis of the RMSE per depth of velocity and density model obtained from single data inversion and joint inversion are presented in the next section.

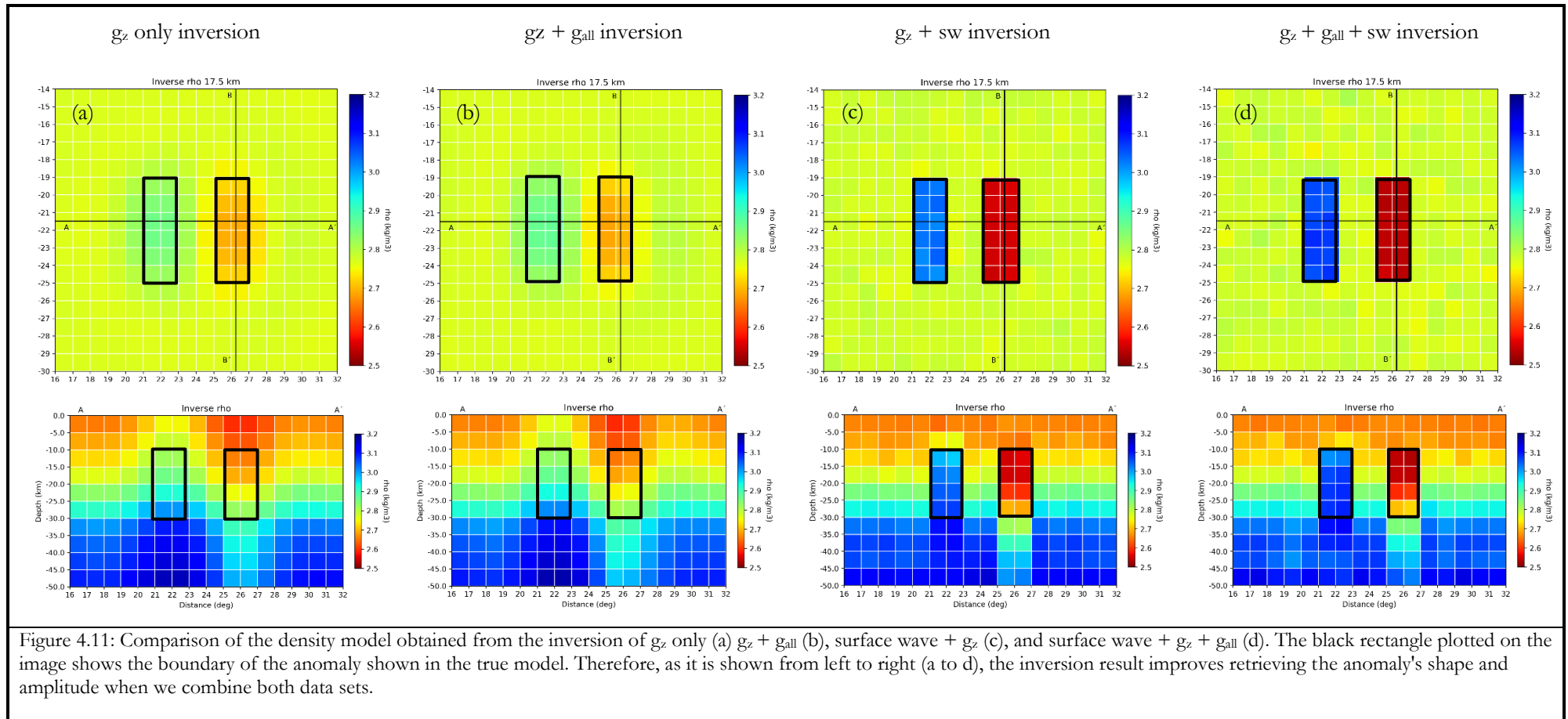
#### 4.4.2. Model Misfit Analysis

The density and velocity models obtained from single data and joint inversion are compared and evaluated based on their RMSE variation. The RMSE of the model misfit per depth is calculated to understand the level of variation between the inverted and true velocity models.

##### 4.4.2.1. Density model

Table 4.1 and the plot shown in Figure 7.3 in Appendix 1 show the variation of the density model misfit RMSE per layer. From the result, we can see that the density model from scenario-1 of gravity-only inversion has the highest RMSE compared to scenario-3 of the joint inversion of gravity, and surface wave data are used. The gravity-only inversion (scenario-1) has a minimum and maximum range of RMSE between 0.2 and 0.6. The RMSE of the model misfit for the inversion of  $g_z + g_{all}$  gradient data is less than or equal to the other set of gravity data only inversion until a depth of 35 km, after which it begins to increase (Table 4.1). This might be due to the constraining information at shallow depths using the gradient data. Therefore, the RMSE analysis indicates that joint inversion of gradients and vertical field data may provide additional information at shallow depths because, compared with the other combination of gravity-only inversion, the resolving power of the inversion increases to retrieve the amplitude and boundary of the anomaly at crustal depth (Ebbing et al., 2014).

The joint inversion results of scenario 3, on the other hand, have an RMSE range between 0 and 0.15. This signifies the joint inversion of gravity with the surface wave data shows a good recovery of the anomaly amplitude per layer from the true model. This is also shown in Figure 4.11, which shows an example of a comparison between the density model obtained when gravity data only and joint inversion of gravity with surface wave data are inverted. Furthermore, the joint inversion result shows the spatial extent and depth of the anomaly than the gravity-only inversion.



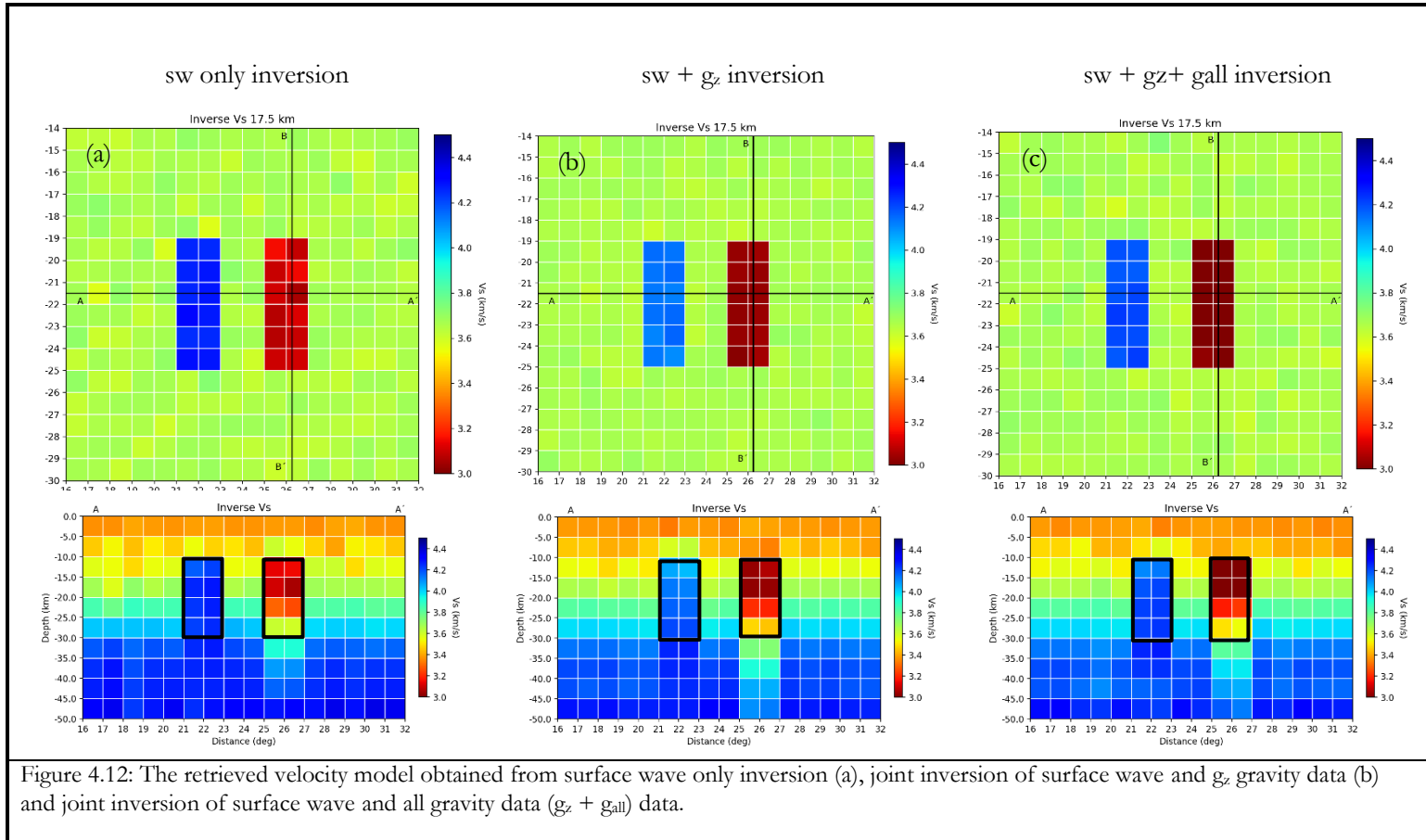


Figure 4.12: The retrieved velocity model obtained from surface wave only inversion (a), joint inversion of surface wave and  $g_z$  gravity data (b) and joint inversion of surface wave and all gravity data ( $g_z + g_{all}$ ) data.

#### 4.4.2.2. Velocity model

The RMSE shown in Table 4.2 and the plot shown in Figure 7.4 in Appendix 1 show the variation of the velocity model misfit RMSE per layer. From the result, we can see that the velocity model from scenario-2 of the surface wave-only inversion has the highest RMSE compared to scenario-3 when joint inversion of gravity and surface wave data are conducted. The surface wave-only inversion has a minimum and maximum range of RMSE between 0.02 and 0.13.

The high RMSE at 30 km is at the transition zone of the anomaly to the background, and it could be related to a less resolved boundary towards the background (Figure 4.8 cross-section A-A'). Furthermore, the high RMSE values may be owing to the fluctuation of velocity values at the low anomaly zone from the background due to the smoothness constraint implemented.

On the other hand, the joint inversion result has an RMSE range between 0.02 and 0.05. This signifies that the joint inversion of gravity with the surface wave data shows a good recovery of the boundary and amplitude of the velocity anomaly per layer from the true model. However, the inversion of the surface wave with a gravity field and surface wave with all gradient data have a very close RMSE value per layer besides a subtle variation as the depth of the model increases. The surface wave with the  $g_z$  performs less than the surface wave with the  $g_z + g_{all}$  data with a 0.001 variation of the RMSE values. This shows that the addition of the gradient data makes a subtle improvement in the shallow part while they perform less at the deeper part of the model. Figure 4.12 (a, b & c) shows an example of visual comparison for the velocity model obtained when surface wave only, surface wave with vertical gravity field ( $g_z$ ), and joint inversion of the surface wave with all gravity data ( $g_z + g_{all}$ ) are inverted.

Table 4.1: RMSE per depth comparison for density model misfit obtained from scenario-1 of gravity data only and scenario-3 of the joint inversion of gravity and surface wave data.

Comparison of RMSE for density misfit from the different inversion scenarios											
Inversion steps		layers (km)									
		5	10	15	20	25	30	35	40	45	50
Scenario-1	$g_z$	0.188	0.216	0.267	0.294	0.342	0.402	0.478	0.506	0.523	0.539
	$g_{all}$	0.189	0.217	0.268	0.295	0.343	0.403	0.478	0.506	0.523	0.539
	$g_z + g_{zz}$	0.188	0.216	0.267	0.294	0.342	0.402	0.478	0.506	0.523	0.540
	$g_z + g_{all}$	0.187	0.215	0.266	0.293	0.342	0.402	0.478	0.507	0.524	0.541
Scenario-3	sw + $g_z$	0.019	0.063	0.055	0.035	0.042	0.091	0.103	0.088	0.111	0.077
	sw + $g_z + g_{all}$	0.018	0.061	0.053	0.033	0.036	0.093	0.096	0.079	0.135	0.071

Table 4.2: RMSE per depth comparison for velocity model misfit obtained from scenario-2 of surface wave only and scenario-3 of the joint inversion of gravity and surface wave data.

Comparison of RMSE for velocity misfit from the different inversion scenarios											
Inversion steps		layers (km)									
		5	10	15	20	25	30	35	40	45	50
Scenario-2	sw	0.015	0.048	0.056	0.030	0.062	0.125	0.064	0.042	0.037	0.044
Scenario-3	sw + $g_z$	0.013	0.021	0.023	0.018	0.020	0.034	0.050	0.037	0.037	0.025
	sw + $g_{all}$	0.012	0.018	0.018	0.016	0.022	0.036	0.047	0.033	0.049	0.026

#### 4.4.3. Data Misfit Analysis

The RMSE of the data misfit obtained from the different inversion scenarios conducted in this chapter is summarized in Table 4.3. From the table, it is evident that the RMSE of the data misfit is very low. The

added 5 % gaussian noise level in the dataset was employed as a boundary condition to evaluate the final inversion data misfit. This is used to overcome either noise overfitting or exaggerated data underfitting. Therefore, an inversion result with data misfit amplitudes close to the gaussian 5 % noise level added to the data set was taken as a good approximation of the inverted model. From the misfit plots (e.g., Figure 7.5 in Appendix 1), we can see that the data misfit has an amplitude below 2 mGal for the gravity field and  $\sim 0.2$  Eotvos for the gravity gradient data, which is comparable to the 5% added noise level. Similarly, the group and phase velocity misfit plot have an amplitude of  $\sim 0.4$  km/sec which is comparable to the gaussian noise level added to the data set (e.g., Figure 7.9, Appendix 2).

Table 4.3 A summary of the data misfit RMSE obtained from the three inversion scenarios

Inversion scenarios		Data used for the inversions	Data misfit RMSE	
			Variables	Values
Scenario 1:	Gravity data only inversion	$g_z$	$g_z$	0.025
		$g_z + g_{zz}$	$g_z$	0.026
			$g_{zz}$	0.013
		$g_{all} (g_{zz} + g_{xx} + g_{yy} + g_{xy} + g_{xz} + g_{yz})$	$g_{zz}$	0.012
			$g_{xx}$	0.042
			$g_{yy}$	0.018
			$g_{xy}$	0.017
			$g_{xz}$	0.047
			$g_{yz}$	0.051
		$g_z + g_{all}$	$g_z$	0.025
			$g_{zz}$	0.038
			$g_{xx}$	0.016
			$g_{yy}$	0.025
			$g_{xy}$	0.015
$g_{xz}$	0.021			
Scenario 2:	Surface-wave data only inversion	group velocity	grp	0.248
		phase velocity	phs	0.241
Scenario 3:	Joint inversion of gravity and Surface-wave data ( $sw + g_z$ )	$g_z$	$g_z$	1.253
		group velocity	grp	0.737
		phase velocity	phs	0.743
	Joint inversion of gravity and Surface-wave data ( $sw + g_z + g_{all}$ )	$g_z$	$g_z$	0.812
		$g_{zz}$	$g_{zz}$	0.21
		$g_{xx}$	$g_{xx}$	0.76
		$g_{yy}$	$g_{yy}$	0.707
		$g_{xy}$	$g_{xy}$	0.588
		$g_{xz}$	$g_{xz}$	0.614
		$g_{yz}$	$g_{yz}$	0.646
		group velocity	grp	0.21
phase velocity	phs	0.211		

Furthermore, the RMSE analysis of the data misfit (Table 4.3) shows that inverting only the gravity data provides the best fit to the gravity anomalies. Similarly, the best fit to the measured values of dispersion is obtained by inverting group and phase velocity dispersion observations only. On the other hand, the three-

dimensional velocity-density model that was derived from the joint inversion fits both data sets concurrently, providing a solution that strikes a balance between the two approaches to fitting the data sets. The misfit plot from the different scenarios of inverting the data set is also presented in Appendix 1 (Figure 7.5).

In conclusion, the simple model synthetic test conducted in this chapter showed how the joint inversion approach performs in a different configurations of data sets. The single data inversion showed less performance in resolving power and retrieving subsurface information. As expected, the inversion of gravity-only data showed less performance in retrieving the boundary and depth location of the density anomalies. Moreover, the different combinations of the vertical gravity and gradient data showed a very small variation of amplitude recoveries of the true model. However, the joint inversion of the vertical gravity, gradients and surface wave data showed a significant improvement in terms of resolving power of the amplitude and shape of the density anomalies. This is summarized in Table 4.1 which shows a clear indication of the added value of each data set to retrieve depth information. Similarly, subsurface velocity information is more accurately retrieved when the joint inversion of the surface wave with gravity is conducted (Table 4.2). However, the joint inversion of gravity and gravity gradient with the surface wave data showed highly significant for density estimation than velocity estimation. This is also shown in a more complex model of method test presented in the next chapter mimicking Botswana geology.

#### 4.4.4. Method Performance Evaluation

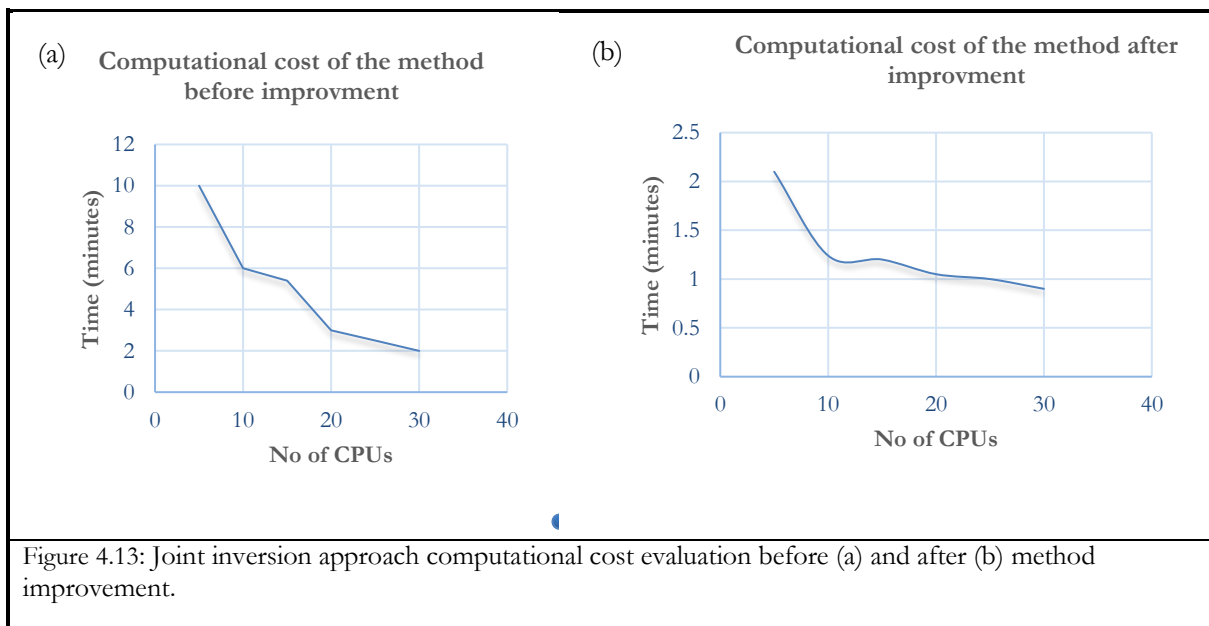
The method performance evaluation was conducted to understand the efficiency of the method in terms of computational cost and scalability for high-resolution and large-scale continental modelling before and after performance improvement was conducted. To generate the data for the joint inversion, it is necessary to calculate the Jacobian matrix for the gravity forward calculation and use a 3D solver that iterates through each cell of the given model for the fundamental mode Rayleigh wave group and phase velocity forward calculation.

However, the calculation of the Jacobian for the forward modelling of the surface wave data that goes through every cell of the 3D cube was the major cause of the high computational cost of the joint inversion approach. Because of this, it is expected that the joint inversion approach's computing time will increase in tandem with the resolution and size of the model. During the initial development phase of the method, the performance of the method was tested using Dell precision 3510 laptops with 16 Gb Ram and 7 processors with a coarser model mesh size of 5\*5 degrees and 10 km in the x, y, and z direction (model size of 20\*20 degrees in x and y and 50 km in z; 4\*4\*5 model), respectively. However, it was unknown whether the method was efficient for large-scale modelling with a high spatial resolution, which needs further improvement and testing of the method to be able to increase the model's resolution in realistic applications.

During this study, the joint inversion approach was updated to calculate the surface wave Jacobian in a 1D using a finite difference scheme over 2D grid points of the 3D cube as explained in subsection 3.1.1.2. As a result, instead of iterating through every cell of the 3D cube, it goes through in 1D over the 2D grid points, which significantly reduces the computational cost and increases the efficiency of the method to calculate the sensitivity kernel of the 3D Earth cube. Therefore, in this study, an evaluation and method testing were conducted using the simple synthetic model tested in this chapter by scaling up the resolution of the mesh size to 1\*1 degree in the x and y directions and 5 km in the z-direction, respectively, for a model size of 0–

16 degree E-W, 0-16 degree N-S, and 0-50 km depth (16\*16\*10 model). The synthetic test performed on a Dell Tower 7910 machine with 196 RAM and 48 processors proved that the method significantly improved computationally since it took approximately 10-15 minutes to complete the inversion of the simple synthetic model, which previously took more than 24 hours using the same configuration of test conducted before method improvement.

Due to the difficulty of conducting the inversion with a high resolution before method improvement, which takes a long period of time (more than 24 hr) to complete the inversion, a simple model of 20\*20 degrees with 5 degrees cell size in the x and y directions and 50 km depth with 10 km cell size in z direction (4\*4\*5 model size) containing two anomalies at the centre was used to compare the efficiency of the method before and after improvement. Figure 4.13 a & b show the computational cost comparison for the inversion needed with respect to the number of CPUs used for the inversion. From the figure, we can see that the performance of the method greatly improved to complete the inversion processes with respect to the number of CPUs. The maximum time required to complete the inversion using 5 CPUs was 10 and 2 minutes before and after improvement, respectively. Therefore, the simple method test conducted here proved that the computational cost of the method was reduced by ~80 % after the method performance improvement and can tell us the potential of the method to apply for large-scale continental and high-resolution modelling.



## 5. SYNTHETIC COMPLEX MODEL MIMICKING BOTSWANA GEOLOGY

### 5.1. Introduction

In the previous chapter, the potential of the joint inversion approach was assessed using a simple synthetic model consisting of two anomalies with positive and negative values from the background. The inversions conducted using synthetic data sets from gravity and surface wave data in different scenarios of data combinations showed the efficiency of the method in retrieving the subsurface information. The analysis conducted also showed that the joint inversion approach performance has improved in terms of computational cost and scalability and proved that the joint inversion of gravity with surface wave data improved the resolving power of the approach than single data inversion. Furthermore, the synthetic test showed the capability of the method to be implemented on regional case studies with the available computational resources. However, the simple synthetic model tested in the previous chapter represents a simplified geology that does not represent the complex geological settings in a region like Botswana, which is the main research area of this study. Therefore, following the conclusion made from the previous analysis, this chapter presents a second-phase synthetic test of the method application using a new model that mimics Botswana's geology. In the following sections, I present the synthetic model set up generated for the inversion mimicking the geology of Botswana, followed by the inversion result analysis and discussion.

### 5.2. Model Setup

The 3D starting model (Figure 7.14 in Appendix 2) is constructed from the 1D average velocity model (Figure 5.1) based on the AK135 global reference model (Kennett et al., 1995) using linear interpolation techniques. The model has dimensions of 18-32 degrees east-west, -30 to -16 degrees north-south, and 0 to 200 km vertically, with 1\*1 degree and 5 km cell sizes in the x, y, and z directions, respectively. Then, the so-called true Earth models (velocity and coupled density model) shown in Figure 5.2 were constructed by mimicking the geology of Botswana (Figure 2.2). The approximated velocity deviation of the anomalies from the average 3D starting model is depicted from the previous nationwide shear wave velocity model of Botswana (Fadel et al., 2020). Therefore, the cratons, sedimentary basins, Okavango rift zone (ORZ), and EARS extension (ER) are shown as homogenous blocks with positive and negative density and velocity anomalies (Figure 5.2). For example, the shallow sedimentary layer depicting the Passarge (PB) and Nosop basin (NB) is shown by negative velocity and density values in the central and western parts of the study area down to depths of 10 and 15 km, respectively. Below the Nosop basin is the buried Maltahohe micro-craton (MC) at a depth of 50 - 200 km, represented by positive velocity and density values. The Congo Craton (CC) in the northwest and Kalahari Craton (KC) in the south and eastern part of the study area are also depicted by high velocity and density values from 5-

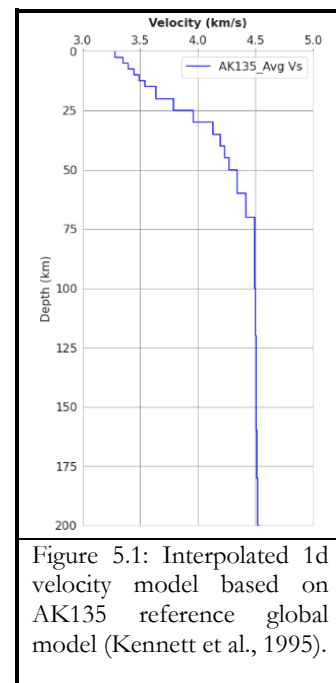


Figure 5.1: Interpolated 1d velocity model based on AK135 reference global model (Kennett et al., 1995).

200 km depths. The ORV and the EARS extension are indicated by negative velocity and density at depths between 5 and 50 km and 70 and 200 km, respectively. The cratons were given a 10 % positive and the Nosop basin and the EARS extension were given a 10 % negative deviation of velocity contrast per layer from the background. On the other hand, the Passarge basin and the shallow OKV rift were given an 8 % negative deviation of velocity contrast per layer from the background. Therefore, the true Earth models described in this paragraph are used to generate the data set of gravity and surface wave data using the gravity and surface wave data forward modeling.

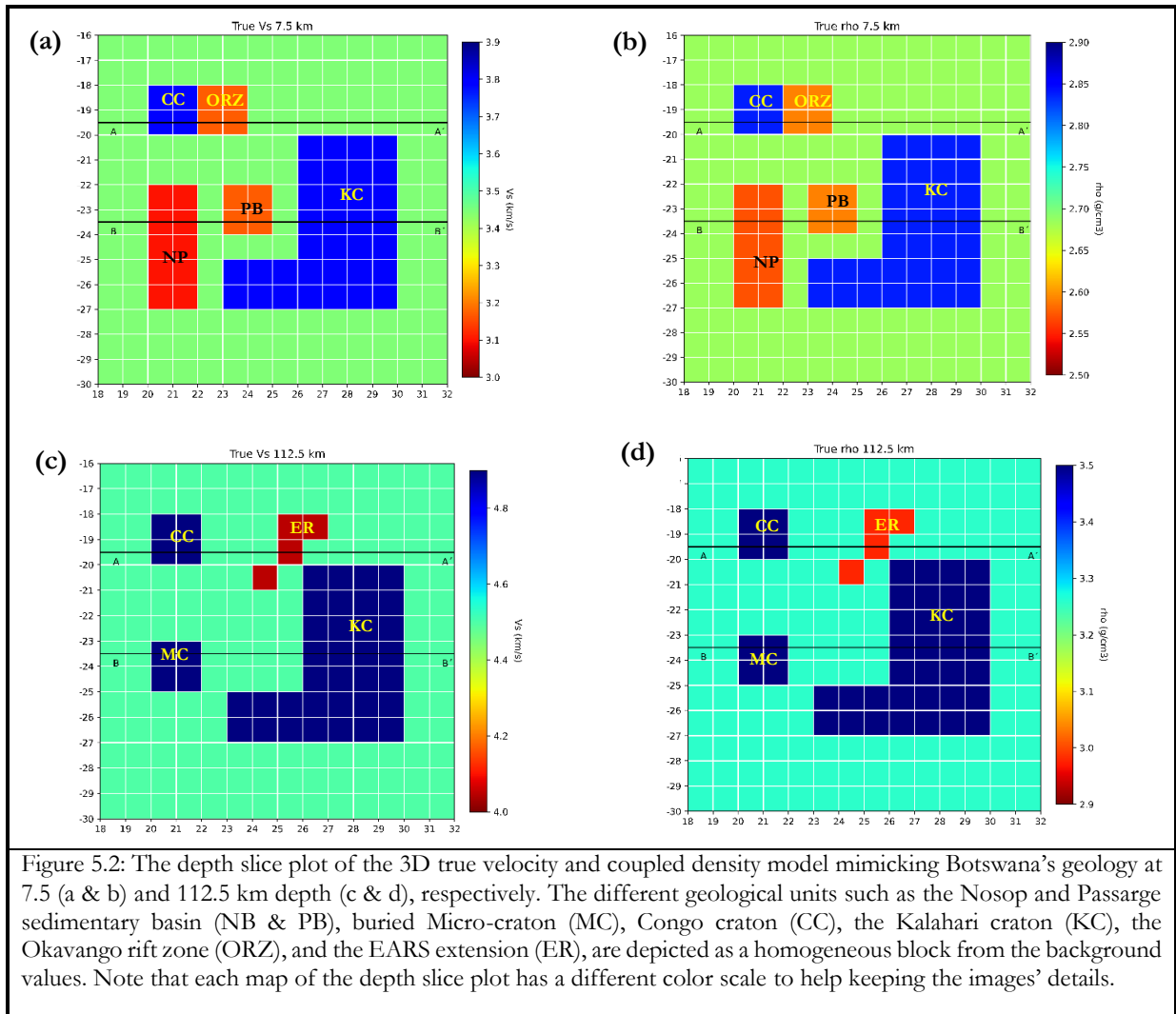
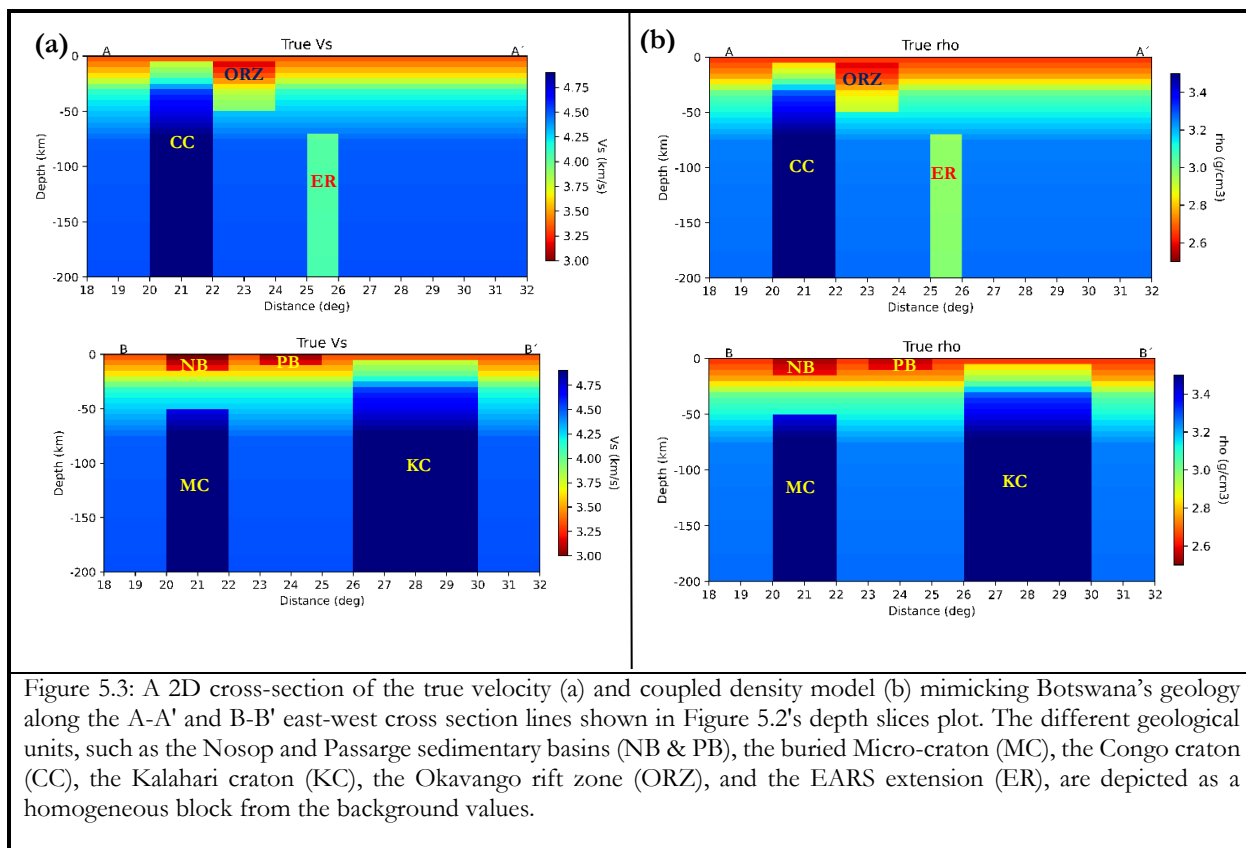


Figure 5.2: The depth slice plot of the 3D true velocity and coupled density model mimicking Botswana's geology at 7.5 (a & b) and 112.5 km depth (c & d), respectively. The different geological units such as the Nosop and Passarge sedimentary basin (NB & PB), buried Micro-craton (MC), Congo craton (CC), the Kalahari craton (KC), the Okavango rift zone (ORZ), and the EARS extension (ER), are depicted as a homogeneous block from the background values. Note that each map of the depth slice plot has a different color scale to help keeping the images' details.



### 5.3. Forward Modelling Results (Data sets)

The data set used in this synthetic test is generated from the synthetic model mimicking Botswana geology using the gravity and fundamental mode Rayleigh wave group and phase velocity forward solver. In the following section, both the gravity and surface wave data are presented.

#### 5.3.1. Gravity Data

Figure 5.4 shows the gravity field and six-component gravity gradient data. The density anomaly model expressed in  $\text{kg}/\text{m}^3$ , shown in Figure 7 in Appendix 2, was used for the gravity forward solver to generate the gravity signals. In order to simulate GOCE satellite gravity data, the gravity signals are calculated at an altitude of 225 km using a computational grid of 20–30 degrees longitude and -27-to-17 degrees latitude with a sample interval of one degree in each direction. To simulate a real case, random noise with a normal distribution, zero mean, and a standard deviation of 5% of the amplitude ranges of the different components was added to the measured signals.

The different gravity component data have different directional sensitivity. The vertical gravity field and vertical component gradient data contain most of the information since they can sense vertically downward to the center of mass (Bouman et al., 2016; J. Ebbing et al., 2014). Therefore, the  $g_z$  and  $g_{zz}$  signal shows a high gravity signal at the eastern edge where the Kalahari craton is located and a low gravity signal at the

northern and western parts where the rift system and sedimentary basin are located, respectively (Figure 5.4). The other non-vertical gravity gradient data have different directional sensitivity, as mentioned in section 4.2.2.1.

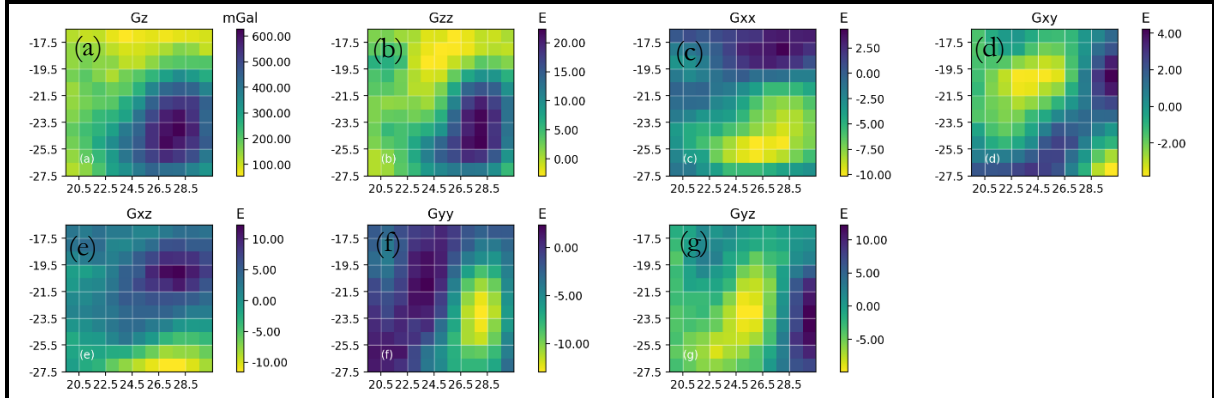


Figure 5.4: Random noise-contaminated gravity signal calculated at a satellite altitude of 225 km from the density contrast model shown in Figure 7, Appendix 2. The gravity component includes the vertical gravity field (a) and the other six-components gradient data (b-g), and the color scale indicates the high and low values of the gravity signals for each component.

### 5.3.2. Surface Wave Data

The true velocity and density model shown in Figure 5.2 was the input for the calculation of the fundamental mode Rayleigh wave group and phase dispersion velocity synthetic data using the surface wave 3D forward solver. The dispersion data are calculated at 40 s periods between 3 and 120 s at 3 s intervals to simulate the real data observation we have for Botswana real data application (3 – 120 s, Fadel et al., 2020). Random noise with a normal distribution, zero mean, and standard deviation of 5 % of the amplitude values was added to simulate real-case observation uncertainty. Figure 5.5 shows the period slices, and 2D cross-sections view of the dispersion measurements cube after they are contaminated with noise. The shallow sedimentary basins (NB & PB), ORZ, depicted by low-velocity values, and the Kalahari craton, depicted by its high-velocity values, are shown at a 7.5 s dispersion map. The deep cratonic root (KC and MC) and EARS extension are shown at the 112.5 s dispersion maps with high and low-velocity values, respectively. The data set was then inverted separately and jointly with the different component gravity data to retrieve the velocity and density information depicted in the true model (Figure 5.2 & Figure 5.3).

To understand the maximum depth extent that can be sampled by the dispersion curve, sensitivity analysis of the group and phase velocity data are conducted. The sensitivity kernel was approximated by approximating the Jacobian using a finite difference scheme. The global AK135 reference velocity model was used as a reference model for sensitivity calculations. Figure 5.6 a-c shows the fundamental mode Rayleigh wave group and phase velocity contaminated average dispersion curve of the true model, the interpolated global AK135 reference model, and the sensitivity for the group and phase velocity dispersion curve. The maximum dispersion curve measured at 120 s has its maximum sensitivity at a depth of 115-135, and it starts to decrease gradually till a depth of 200 km.

JOINT INVERSION OF SATELLITE GRAVITY AND SEISMIC SURFACE WAVE DATA: A SYNTHETIC TEST AND ITS APPLICATION FOR BOTSWANA CRUST AND UPPER MOST MANTLE VELOCITY AND DENSITY MODELING

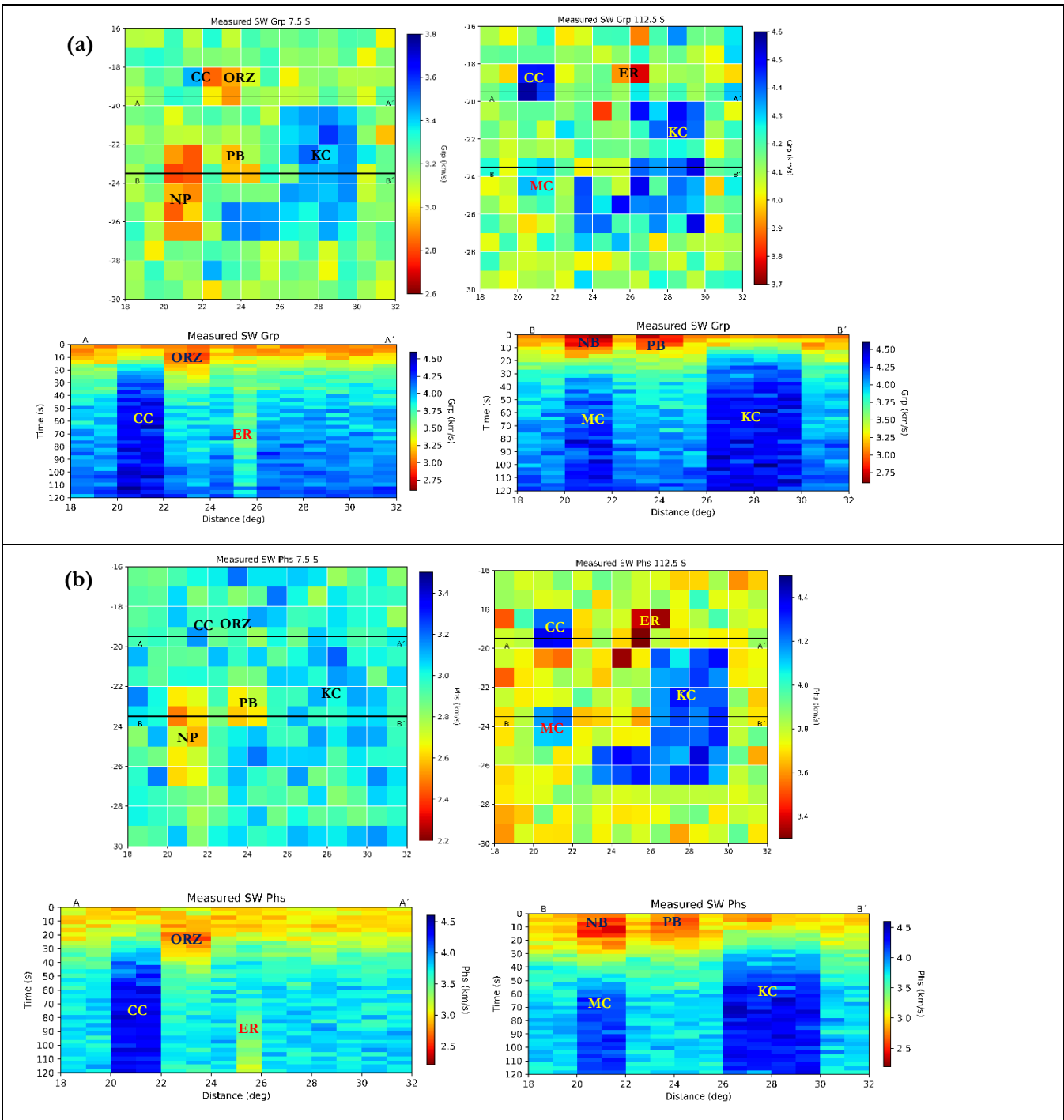


Figure 5.5: Random noise-contaminated Rayleigh wave group (A) and Phase (B) velocity at 7.5, and 112.5 s calculated from the synthetic model shown in Figure 5.3. A-A' & B-B' cross-sections show the group and phase velocity measurements calculated for the same locations as in the depths slice subplot.

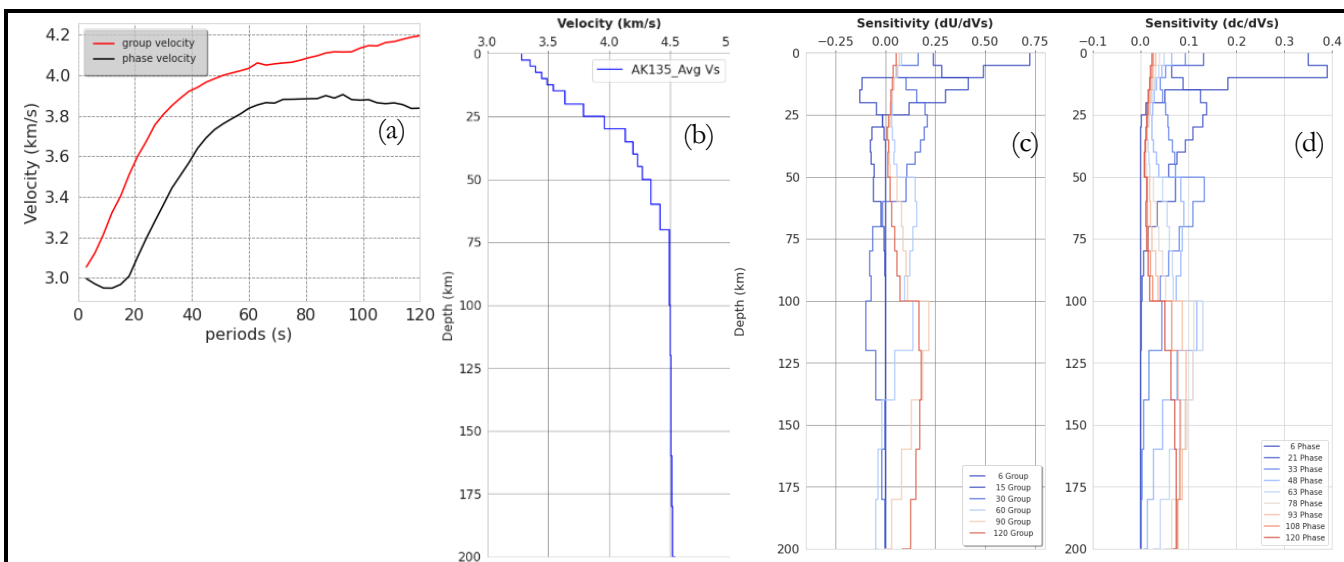


Figure 5.6: The calculated average group and phase velocity dispersion curves over period 3-120s after noise contamination (a). (b) shows the global shear wave velocity model interpolated from AK135 (Kennett et al., 1995) which is used as a reference model., as well as the sensitivity analysis of the group and phase velocity period used, which demonstrates that the group and phase velocity up to 120s can depths up to 200 km (c and d, respectively).

#### 5.4. Inversion

The gravity (total field and gradient data) and the surface wave components (Rayleigh wave group and phase velocity dispersion data) described in section 0 are then used in the inversion processes targeting the velocity and density structure described in section 5.2 (Figure 5.2 & Figure 5.3). As described in section 3.2.2, the inversion was conducted in three different scenarios: firstly, gravity only inversion, secondly, surface wave only inversion and thirdly, joint inversion of gravity and surface wave data. The maximum number of iterations was defined as 150, and the termination threshold was defined as 0.01 % of the starting misfit to let the inversion minimize the objective function as low as possible within the available number of iterations. An error floor of 5% was considered as acceptable, given the 5% random noise added to the data and mimicking the difficulty of estimating the uncertainty level of the geophysical inversion (Julià et al., 2000). In the following section, the joint inversion results and discussions are presented.

#### 5.5. Result and Discussion

This section presents the findings and discussions of the individual and joint inversions conducted in three different scenarios of using the data set described in section 5.4. The first section presents the comparison of the density model derived when gravity data only are used and when they are jointly inverted with the surface wave data (scenarios 1 & 3). The second section presents the comparison of the retrieved velocity model when surface wave data are used independently and jointly with gravity data (scenarios 2 & 3).

### 5.5.1. Recovered density model

Figure 5.7 shows the true density model, recovered density model from scenario-1 of gravity data only inversion, and scenario-3 of joint inversion of gravity with surface wave data (from left to right, respectively). The result demonstrates that the density model generated by inverting the gravity data only (scenario 1, Figure 5.7 c & d) deviates significantly from the true density model structure. This is to be expected because the sensitivity of the gravity field weakens with depth (Capriotti and Li, 2021; J. Ebbing et al., 2014). Despite some of the retrieved features of the Kalahari in the east and Congo craton in the northeast, they produce a low-resolution model with fuzzy boundaries in which the shape and location of the anomalies were not appropriately recovered. The shallow sedimentary basin, the deeper EARS extension, and the buried Maltahohe micro-craton are less resolved from the gravity inversion results and are quite far from the true density model structure.

The 2D cross-section plot along lines A-A' and B-B' shown on the depth slice plot is presented in Figure 5.8. The Cross-section plot from the gravity data inversion (Figure 5.8 b) shows a fuzzy boundary that failed to delineate the boundary of the anomalies and produced a model that is far from the true model (Figure 5.8 a). Cross-section A-A' shows the location of the Congo craton (CC) but with less well-resolved sharp boundaries at the top and also as it goes deeper below 150 km. Similarly, the boundary and location of the ORZ and the EARS extension at the right side of the Congo craton are not clearly resolved. Cross-section B-B' also shows less resolved buried micro-craton and artifacts at the boundary of the Kalahari craton. Furthermore, the location of the shallow sedimentary basin is indicated by fuzzy boundaries from the background (Figure 5.8 b). Generally, gravity data-only inversion does not recover the shape of the anomalies and shows artifacts around the boundary of the anomalies, which is resolved by integrating with surface wave data as described below.

The joint inversion of gravity with surface wave data improved the inversion's resolving power to resolve the anomalies' amplitude and shape. For example, from the joint inversion density model (Figure 5.7 e & f), we can find that the problem raised in the gravity-only inversion is well solved. The shapes and amplitudes of the anomalies are close to the true model and reveal a higher resolution in characterizing geological units. From the result (Figure 5.7 e & d), the shallow central sedimentary basin (PB) and the northern ORZ are resolved, which was not shown in the gravity-only inversion. Similarly, the shape and anomalies of the Congo Craton (CC) and Maltahohe micro-craton (MC) are well resolved despite its less amplitude retrieved at the bottom boundary of the anomalies, which are inherently unresolved in the gravity-only inversion. This is due to the complementary sensitivity of the surface wave and gravity data to resolve the anomalies extent of deep subsurface structure. The Kalahari craton (KC) covering a large part of the area is also clearly resolved. Therefore, the joint inversion of gravity with the surface wave data increases the resolution of the model and reduces the non-uniqueness property of gravity data inversion.

The depth extent of the recovered geological structure is also shown in the 2D cross-section plot depicted in Figure 5.8-c. Cross-section A-A' shows the recovered Congo Craton (CC) at the western, the shallow Okavango Rift Zone (ORZ) and the East African Rift extension (ER). The Congo cratons are depicted by their high-density values, while the ORZ and ER systems are depicted by their low-density values. Despite smearing characteristics at the bottom and top boundaries of the ORZ and ER, the geological units' location, depth, and amplitude are close to the true model structures. The ER system, believed to extend to a depth of 200 km, is retrieved as a long elongated low-velocity zone. However, the top boundary of the ER from

the background is not resolved (Figure 5.8 c, A-A'). This might be to the limited sensitivity of gravity and surface wave data to detect discontinuities (Kaban et al., 2016; Roux et al., 2011; Shen et al., 2013; Victor et al., 2020).

The second cross-section B-B' that passes through the E-W direction shows the easterly Nosop Basin (NB) and the expected location of the buried Maltahohe micro-craton (MC) beneath the Nosop Basin (NB) at a depth of 50 km till 200 km characterized by its low and high density, respectively. The Passarge basin (PB) is also retrieved at a depth of 0-10 km, characterized by its low-density anomaly. The Kalahari Craton is also retrieved in the eastern part of the map, characterized by high-density values.

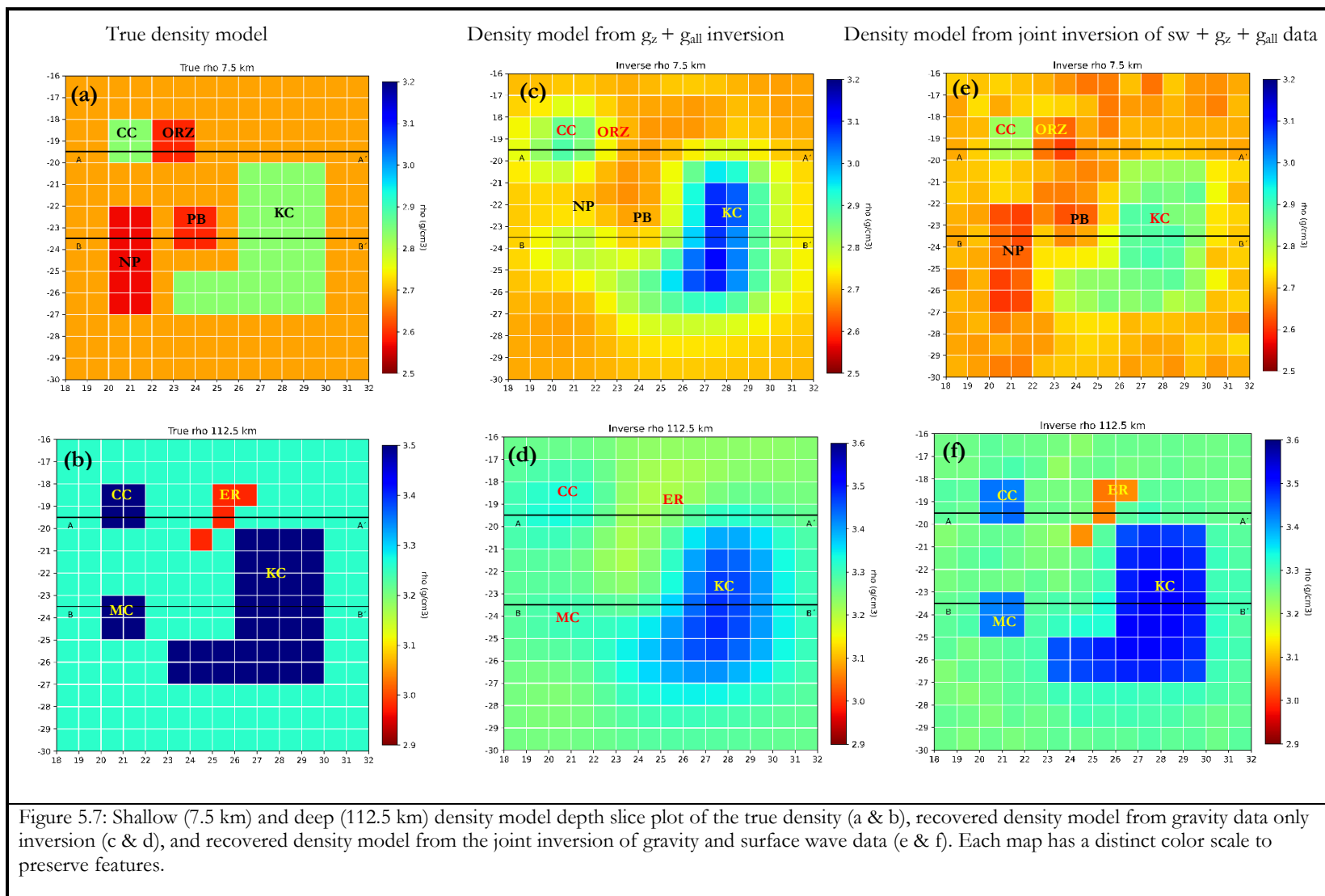
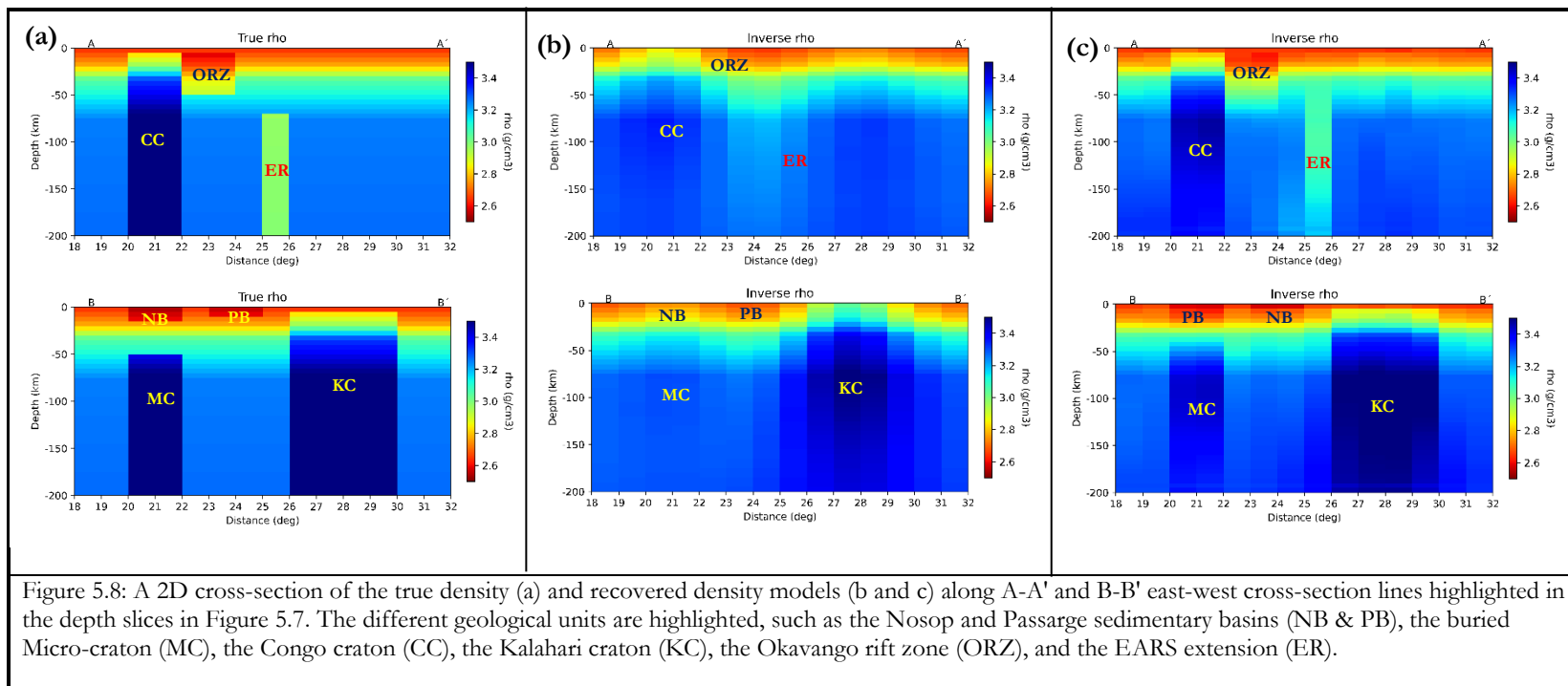
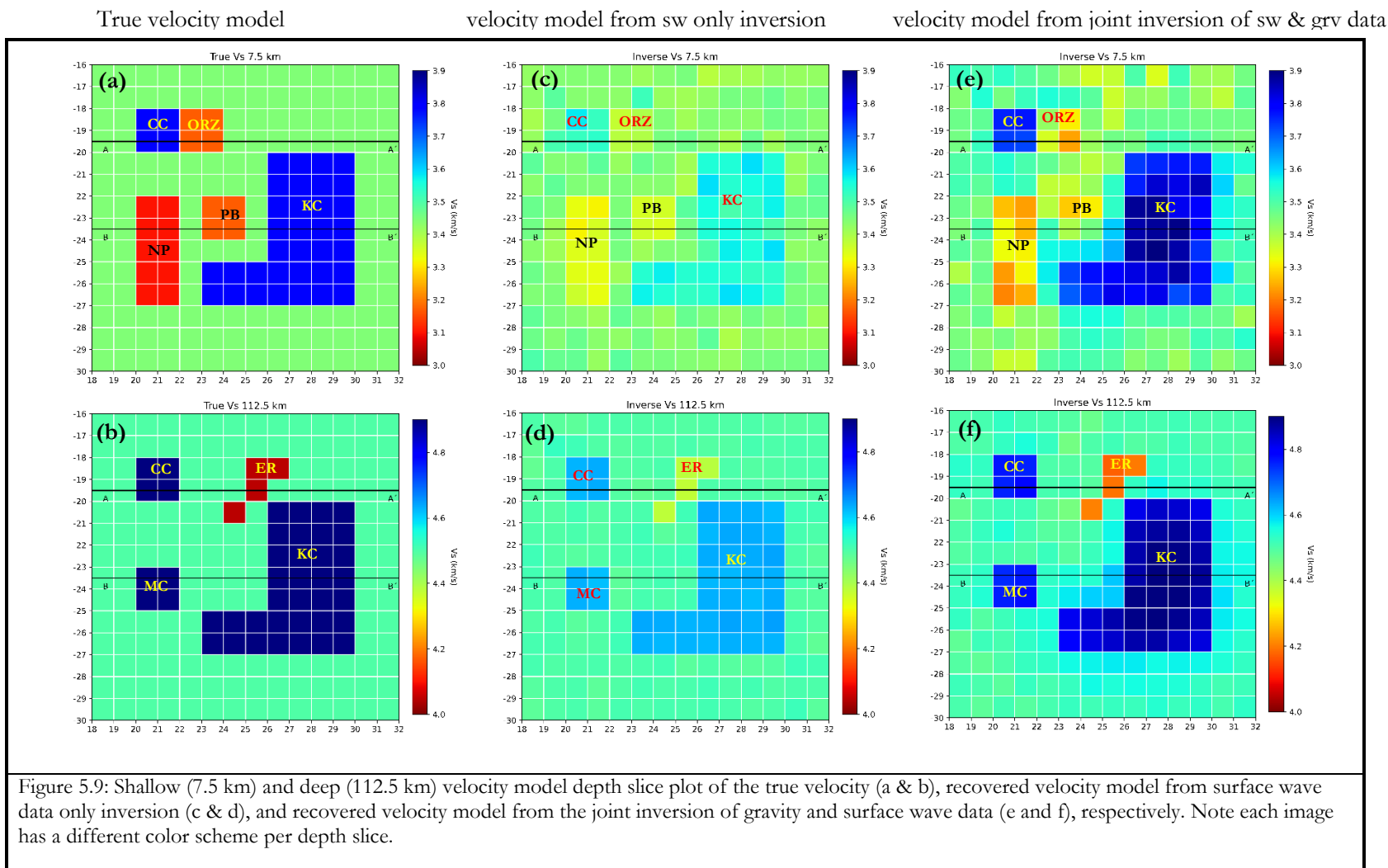


Figure 5.7: Shallow (7.5 km) and deep (112.5 km) density model depth slice plot of the true density (a & b), recovered density model from gravity data only inversion (c & d), and recovered density model from the joint inversion of gravity and surface wave data (e & f). Each map has a distinct color scale to preserve features.



### 5.5.2. Recovered velocity model

In a manner similar to the inversion conducted to retrieve the density model, the surface wave data only and the joint inversion with the gravity data are conducted to retrieve the velocity structure of the true model. The surface wave-only inversion was conducted jointly using the group and phase velocity data. The joint inversion was conducted using all the gravity ( $g_z$  and the six components gradient) data with the group and phase velocity data. Figure 5.9 shows the comparison of the true velocity model (Figure 5.9 a & b) and recovered velocity model from the surface wave only (Figure 5.9 c & d) and joint inversion of the surface wave with gravity data (Figure 5.9 e & f). From the result, it can be seen that the true model's basic features are well resolved from both types of inversion. The depth slices in Figure 5.9 at 7.5 km and 112.5 km shows the location and boundary of all the geological units. However, the recovered velocity model from the joint inversion showed an improvement in recovering the amplitude of the anomaly than the velocity model obtained from the surface wave-only inversion, which will be quantified in the following section 5.5.3. This is due to the complementary advantage of using both data sets over a single data inversion.



The cross-section plot, Figure 5.10 at the A-A' and B-B' lines highlighted in Figure 5.9, also shows the depth extent of the geologic units. From the figure, we can see that the surface wave-only inversion (Figure 5.10 b) and joint inversion result from the surface wave with gravity data (Figure 5.10 c) resolve the boundaries of the anomalous bodies despite the fact that the amplitude of the anomalies is more saturated when conducting the joint inversion of the two data sets. Furthermore, the vertical boundary of the anomalies are delineated more accurately from the background when both

data set are inverted together. However, the top and bottom boundary of the anomalies is smeared toward the background, which might be due to the limited sensitivity of surface wave data to detect discontinuities (Shen et al., 2013). For example, the top-bottom boundaries of the shallow sedimentary basin (NB and PB, OKV, and the EARS extension) are not delineated clearly (Figure 5.10, b & c).

Generally, the synthetic test conducted in this chapter also revealed the efficiency of the method in retrieving the information given in the true model (Figure 5.2 & its cross-section Figure 5.3). Therefore, the velocity and density models obtained from the joint inversion demonstrate that the retrieved structures are more accurately recovered and are closer to the true model values. A more numerical comparison of the overall inversion result was conducted by estimating the RMSE of the model misfit and data misfit, as shown in the following section (section 5.5.3, Table 5.1 & Table 5.2).

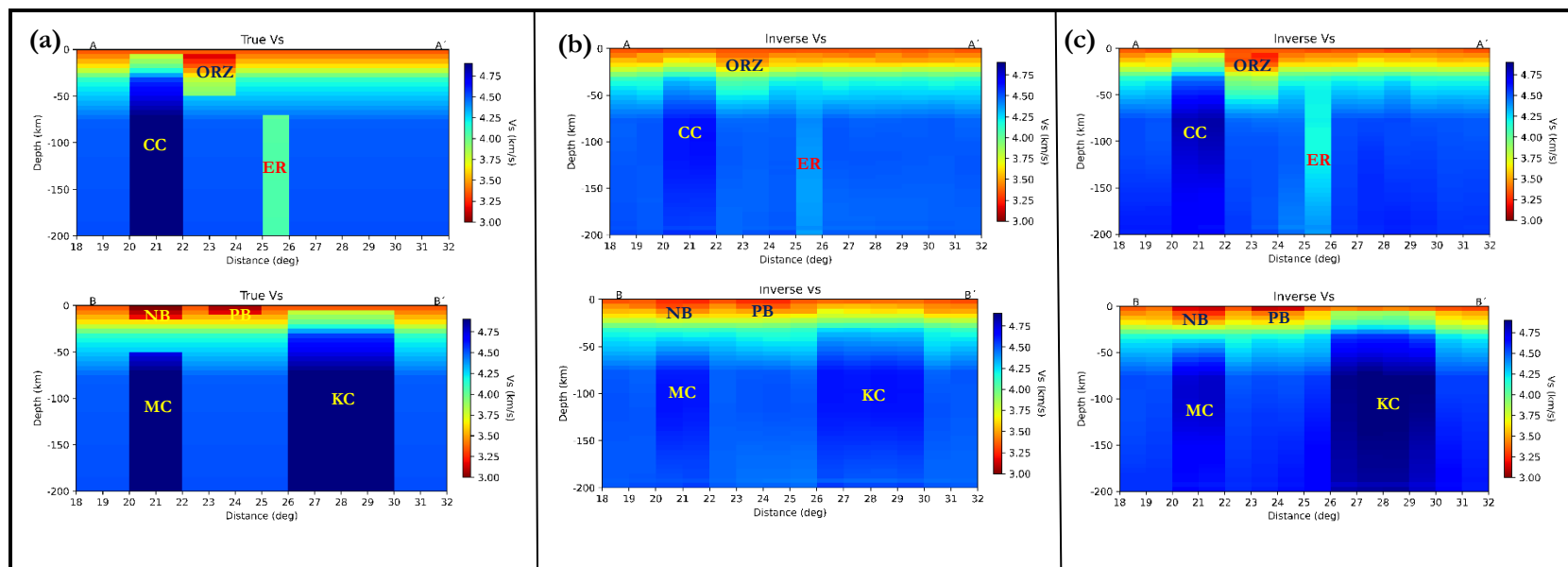


Figure 5.10: A 2D cross-section of the true density (A) and recovered density models (B and C) along A-A' and B-B' east-west cross-section lines. The different geological units are highlighted, such as the Nosop and Passarge sedimentary basins (NB & PB), the buried Micro-craton (MC), the Congo craton (cc), the Kalahari craton (KC), the Okavango rift zone (ORZ), and the East African Rift system (ER).

### 5.5.3. Model misfit analysis

The model misfit is the residual between the true model and the inverted model. Table 5.1 shows the RMSE of the velocity and density residuals after each scenario of inversion. Comparing the RMSE of the velocity and density residuals, it is possible to see that the joint inversion has low RMSE values than the individual data inversion.

Table 5.1: RMSE of the recovered density and velocity model from the single data inversions scenario-1 & -2 and joint inversion of both data sets scenario-3.

Model misfit RMSE analysis table for different inversion scenarios			
Inversion scenarios	Data used for the inversions	Model misfit RMSE	
		Model	Values
Scenario 1: Gravity data only inversion	$g_z + g_{all}$	Density	0.099
Scenario 2: Surface-wave data only inversion	group + phase velocity	velocity	0.168
Scenario 3: Joint inversion of gravity and Surface-wave data	$g_z + g_{all} +$ group and phase velocity surface wave data	Density	0.062
		Velocity	0.109

#### 5.5.4. Data misfit analysis

The data misfit obtained from the misfit function is the data residual between the observed and model response from the individual and joint inversion of the data set. Similar to the model misfit shown in Table 5.1 above, the RMSE of the data misfit for the joint inversion is lower than the RMSE of the individual data inversion. This signifies the importance of the joint inversion that produces a model that simultaneously fits the data set than the single data inversion. The data misfit plot is presented in Figure 7.16 - Figure 7.19 in Appendix 2.

Table 5.2: Data misfit RMSE for each of the inversions conducted using the single data and joint inversion of the data set.

Data misfit RMSE analysis table for different inversion scenarios			
Inversion scenarios	Data used for the inversions	Data misfit RMSE	
		Variables	Values
Scenario 1: Gravity data only inversion	$g_z + g_{all}$	$g_z$	0.9019
		$g_{zz}$	0.061
		$g_{xx}$	0.016
		$g_{yy}$	0.029
		$g_{xy}$	0.041
		$g_{xz}$	0.020
		$g_{yz}$	0.056
Scenario 2: Surface-wave data only inversion	group velocity	grp	0.027
	phase velocity	phs	0.034
Scenario 3: Joint inversion of gravity and Surface-wave data	$g_z + g_{all}$	$g_z$	0.872
		$g_{zz}$	0.054
		$g_{xx}$	0.013
		$g_{yy}$	0.023
		$g_{xy}$	0.032
		$g_{xz}$	0.017
		$g_{yz}$	0.053
	group velocity	grp	0.009
	phase velocity	phs	0.010

## 6. REAL DATA APPLICATIONS

In this chapter, the application of the joint inversion approach to study the crustal and upper mantle structure beneath Botswana is presented. As it is described in chapter 1, Botswana is a subject of disputed hypotheses where different research papers have presented divergent views about the tectonics and geodynamics of the country. Those are the hypothesis about the existence of buried Maltahohe micro-craton and its linkage with the neighboring Kaapvaal cratons and rifting in central Botswana and its connection with the 2017 earthquake. Moreover, most of the research in Botswana applied a single-data approach to understand the nature of the subsurface. However, in this section, the joint inversion approach introduced in the preceding chapters is applied using real data observation of satellite gravity and seismic surface wave data. Therefore, in the following section, a brief overview of the data set used and sensitivity analysis (section 6.1), the 3D inversion processes conducted and the influence of starting model and model parameters (section 6.2), and finally followed by the result and discussion (section 6.3) is being presented.

### 6.1. Data sets

In this phase of real data application of the joint inversion approach, satellite gravity and seismic surface wave data described in section 2.2 were used jointly to model Botswana's 3D velocity and density structure. The data includes the vertical gravity field, GOCE gravity gradient measurements, and Rayleigh wave group and phase velocity measurements of Botswana. The free air gravity observations were used because the joint inversion method can consider the topography in the vertical resolution. We implemented the topography with 1 km resolution in the vertical direction to reduce computational costs. The following section presents the sensitivity analysis result of the surface wave dispersion data and the inversion process conducted below.

### 6.2. Surface wave Group and Phase velocity Dispersion Sensitivity Analysis

The sensitivity of the Rayleigh wave group and phase velocity to depth depends on the measured periods (Fadel et al., 2020; Julià et al., 2000). A short period dispersion (e.g., 3-20s) can provide information about the shallow part of the subsurface (e.g., crustal depths), while a longer period measurement (e.g., > 20s) can provide information about deeper Earth subsurface (lower crust - upper mantle depths). Therefore, the sensitivity test can help us give information about the extent to which we can see the subsurface from the inversion based on the used measured periods. Figure 6.1 below shows the sensitivity test for the average group and phase velocity curve of Botswana. The sensitivity analysis was conducted till a depth of 200 km using the 1D interpolated AK135 (Figure 5.1) which is used to derive the 1D average shear wave velocity model of Botswana shown in Figure 6.2 as a reference model. From the sensitivity test, we can see that the group velocity dispersion curve measured till 30 s can sample the subsurface information up to 60 km depth but with decreasing sensitivity after 30 km (Figure 6.1 b). On the other hand, the longer period (120 s) phase

velocity measurement can give information up to 200 km but also has a decreasing sensitivity after 150 km depth (Figure 6.1, c).

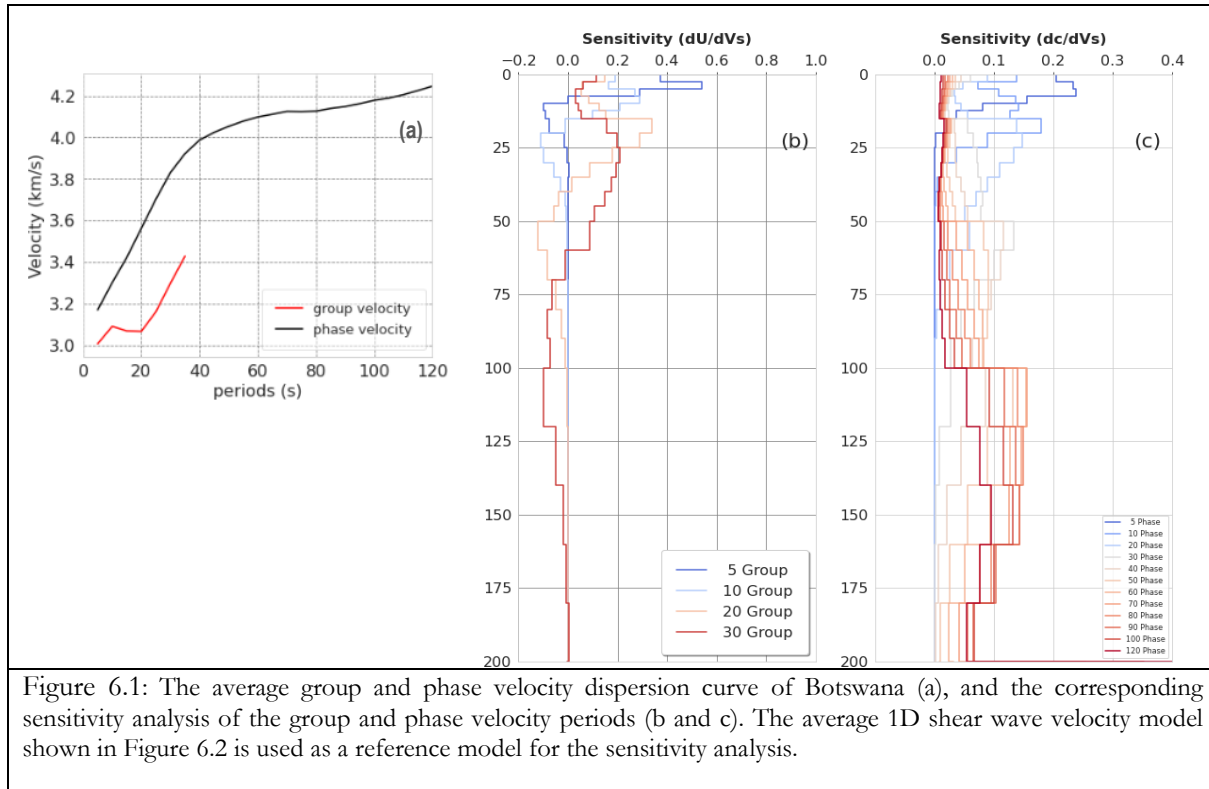


Figure 6.1: The average group and phase velocity dispersion curve of Botswana (a), and the corresponding sensitivity analysis of the group and phase velocity periods (b and c). The average 1D shear wave velocity model shown in Figure 6.2 is used as a reference model for the sensitivity analysis.

### 6.3. 3-D Joint inversion of surface wave and gravity data

#### 6.3.1. Model discretization

For the joint inversion conducted in this chapter, we have two tesseroïd models called the Earth and surface wave dispersion tesseroïd models. Both have a similar geographical extent of 18 to 32 degrees longitude and -30 to -16 degrees latitude discretized at one-degree intervals laterally and 5 km intervals vertically, yielding 7840 cubic cells. The surface wave dispersion tesseroïd model ranges from 3-120s periods with 3s discretization, while the Earth's tesseroïd model has a depth extent of 200 km. To avoid edge effect in the gravity inversion (e.g., sudden drop in the gravity signal at the boundaries of the model due to empty density neighbouring space), both Earth and surface wave models were padded by 2 degrees by giving the average velocity and surface wave dispersion curve values for the padded cells, respectively. In contrast, the Earth tesseroïd model is used to build the starting model for the inversion processes using a pre-defined velocity model that will be further discussed in subsection 6.3.2.1.

### 6.3.2. 3D inversion

#### 6.3.2.1. The influence of starting model and model parameters

In this phase of real data application, it was found that the inversion scheme was highly influenced by the starting model and inversion parameters used. Therefore, three types of starting models were tested to develop a suitable starting model that could fit the inversion process. Firstly, the previously conducted 3d shear wave velocity model determined from the surface wave data of Botswana, developed by Fadel et al. (2020), with a 1-degree resolution, was used as starting model of the inversion. However, it was found that this starting model would not allow the inversion process to proceed, due to the instability of the surface wave forward solver, unless using high damping weight and smoothness constraints. Even though high damping and smoothness constraints were added to improve the result, the inversion produced a model that resembled the starting model, fitting the surface wave only but could not fit the gravity data.

Another attempt was conducted using the global AK135 reference global shear wave velocity model as a starting model. This scenario was conducted considering the consistency of the density values of the model as background values for the satellite gravity data global coverage with the satellite gravity data used in the inversion. However, similar to the first attempt conducted, the inversion process could not proceed due to instability unless high damping and smoothness parameters were considered. This didn't improve the inversion result but damped to the background model that does not fit the data set.

Finally, the average 1D shear wave velocity model of the study area from Fadel et al. (2020) was used as a starting model (Figure 6.2). The 1D average shear wave velocity was produced by the joint inversion of the average 1D group and phase velocity curve of the study area using the Levenberg-Marquardt least square algorithm and the average global AK135 reference velocity model as a starting model. They parametrized the Earth into 22 layers from the surface until 410 km mantle discontinuity. They used a variable step size for depth interval: 2.5 km for the first 15 km, 5km for the depth from 15 – 50 km, 10 km for the depth from 50 – 100 km, and finally, a 20 km depth interval till the end of the model. However, in this research, we used an interpolated version of the model using the spline interpolation scheme with a constant 5 km step size from the surface to 200km depth as a starting model for our joint inversion (Figure 6.2). After a systematic trial and error test of

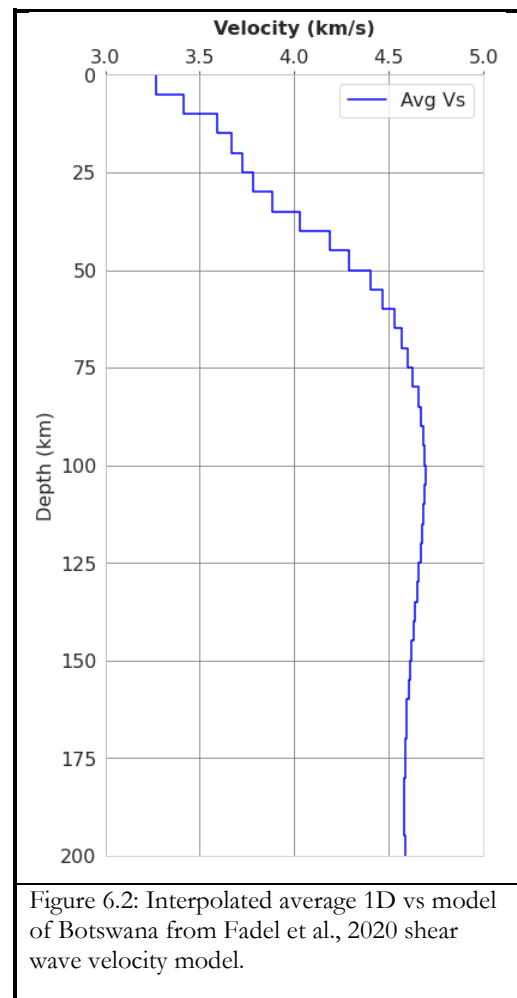


Figure 6.2: Interpolated average 1D vs model of Botswana from Fadel et al., 2020 shear wave velocity model.

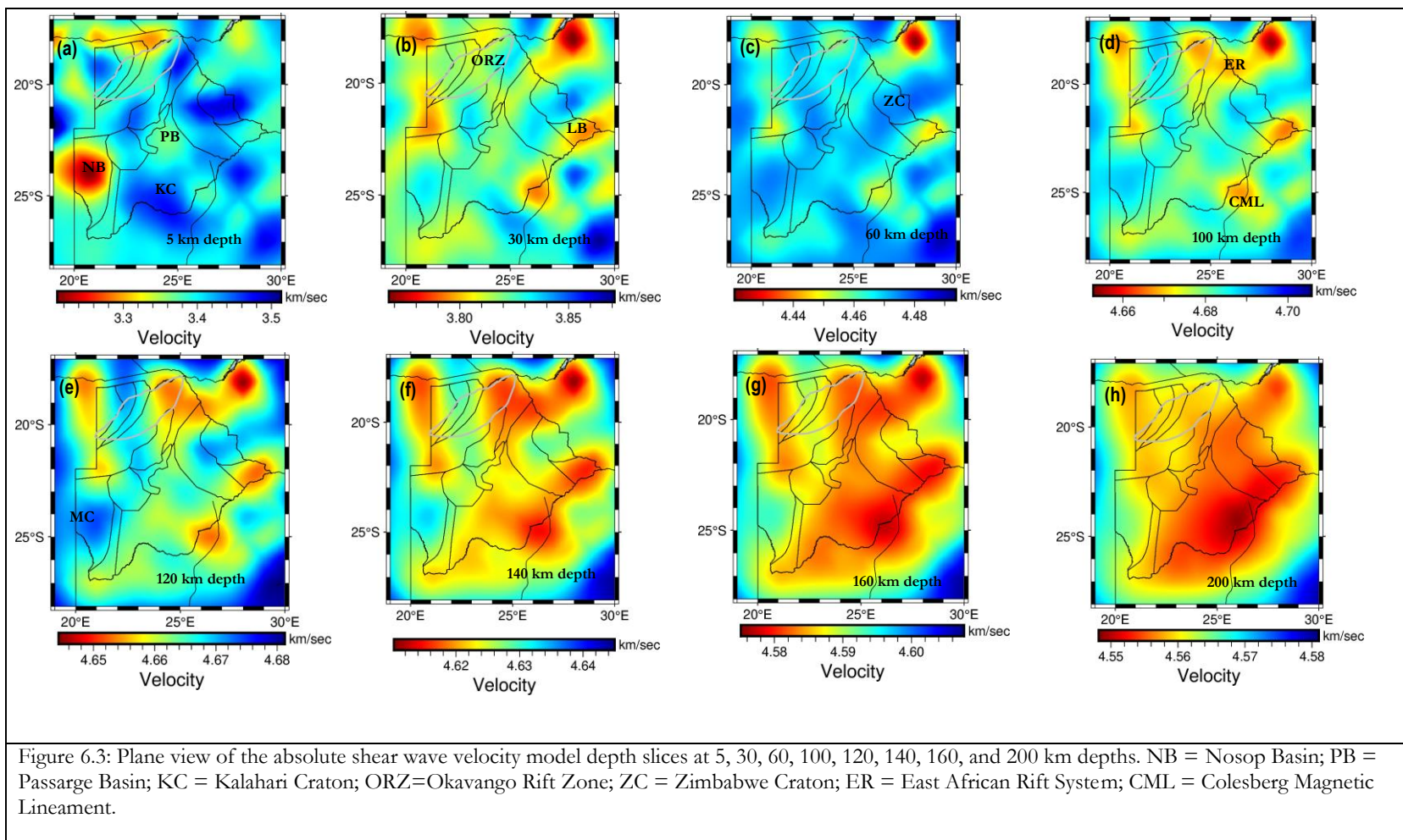
different values of data weighting, background model damping, and smoothness parameters, the inversion was conducted with a data weight of 1.3, 0.04, 0.02, 0.03, 0.03, 0.09 0.06 for gravity data components ( $g_z$ ,  $g_{xx}$ ,  $g_{yy}$ ,  $g_{xy}$ ,  $g_{xz}$ ,  $g_{yz}$ ,  $g_{zz}$ , respectively) and 0.08 and 0.09 for group and phase velocity dispersion data, background damping weight of 0.2 and smoothness constraints of 0.1, 0.1 & 0.2 in x, y & z directions, respectively.

The inversion result from this scenario of using the 1D average shear wave velocity model of the study area as starting model has interpretable features. However, the result has weak variation of velocity and density values that deviates from the previously conducted 3D shear wave velocity model of Botswana (Fadel et al., 2022). As a result, an attempt to explain some of the subsurface information was conducted till a depth of 120 km; information obtained beyond this depth was not considered reliable for interpretation. In the following section, the result of the joint inversion is presented and discussed below.

## 6.4. Result and Discussion

### 6.4.1. Overview of the 3D velocity and density model of Botswana

The final 3D shear wave velocity and density model are shown as depth slices shown in Figure 6.3 and Figure 6.4, respectively. Both the shear wave velocity and density model have complementary information about the subsurface structure that can be recognized and interpreted as the same tectonic features. High velocity and density anomalies is visible in the Kaapvaal and Zimbabwe cratons in the south and east, as well as the Congo craton in the northeast and beneath the Rehoboth province, where it is believed to be the location of the Micro-Craton (A. Wright and Hall, 1990; Begg et al., 2009; Fadel et al., 2020). On the other hand, low velocity and density anomalies were observed in the sedimentary basins of eastern and central Botswana, at the mobile belts and the ORZ, which are thought to be the terminus of the EARS (Kinabo et al., 2007; Kolawole et al., 2017; Leseane et al., 2015; Modisi, 2000; Ortiz et al., 2019; Yu et al., 2015). Generally, some patterns of the observed velocity anomalies agree with the known tectonic units. However, the magnitude of the relative velocity and density variation is significantly smaller than the reported shear wave velocity anomalies using the surface wave dispersion data in Fadel et al., 2018. This is mainly due to the strong damping and smoothness constraints used in the inversion to prevent the inversion process from being stopped due to the instability of the 1D surface wave forward solver when inconsistent or unrealistic,  $V_p$ , and density values are exceeded during the updating of the inverted model during the joint inversion process. In the following section, I will present the interpretation of some of the velocity and density structures observed from the 3D inverted velocity and density models using the depth slice plot. However, because of the modest change in velocity and density, the cross-section map does not reveal a clear variation in tectonic features and is therefore less likely to be utilized for interpretation.



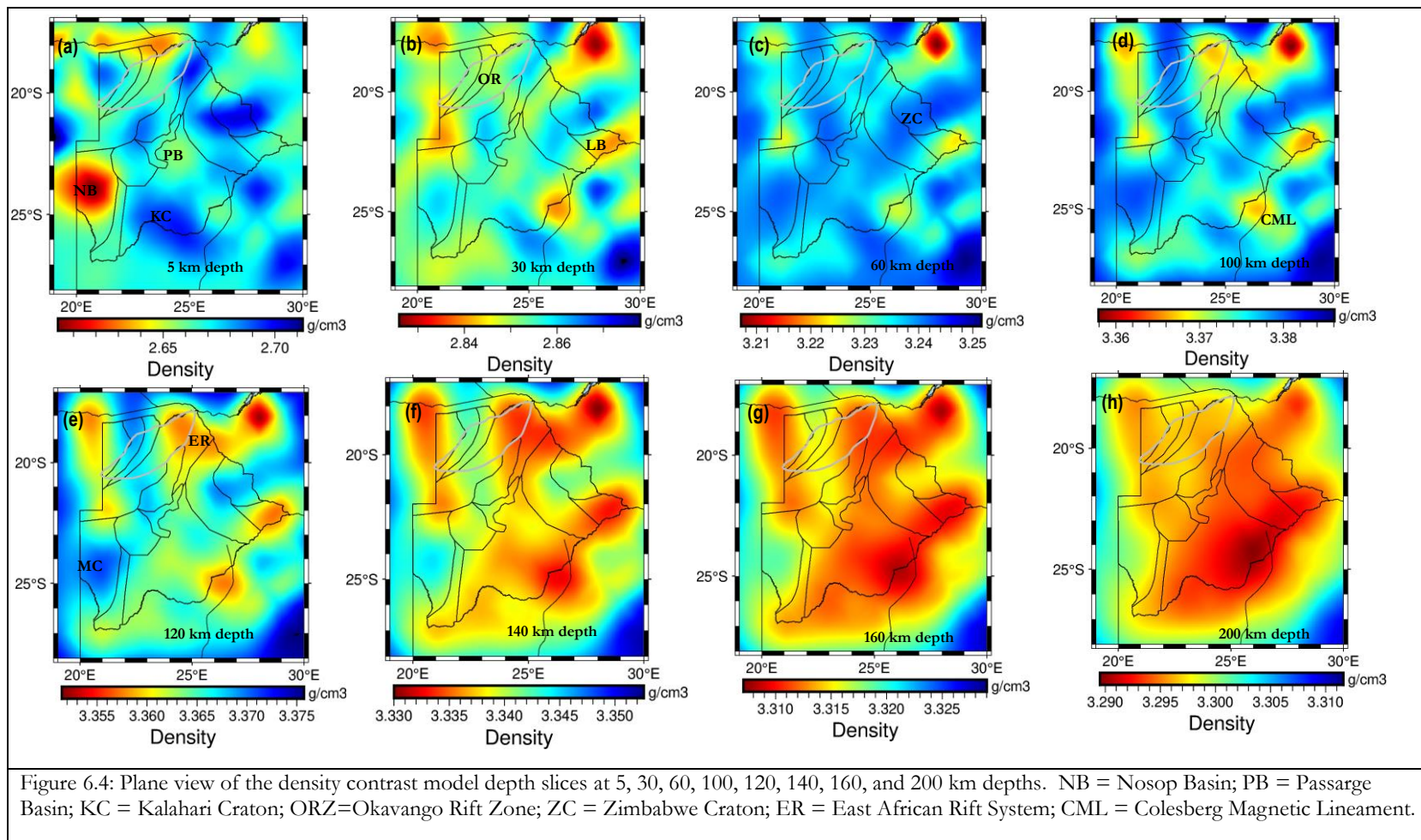


Figure 6.4: Plane view of the density contrast model depth slices at 5, 30, 60, 100, 120, 140, 160, and 200 km depths. NB = Nosop Basin; PB = Passarge Basin; KC = Kalahari Craton; ORZ=Okavango Rift Zone; ZC = Zimbabwe Craton; ER = East African Rift System; CML = Colesberg Magnetic Lineament.

### 6.4.2. Sedimentary Basins

The first noticeable contrasting feature observed in the crust are the low velocity and density anomalies of the thick Nosop (NB) in the west and Passarge (PB) sedimentary basins in central Botswana ( Figure 6.5 and Figure 6.6, a). The observable signature of relatively low velocity and density anomaly of the Nosope sedimentary basin is observed till a depth of  $\sim 15$  km (Figure 6.5 a, & cross-section B-B' highlighted in red circle). The depth extent of the Nosop sedimentary basins coincides with the early studies of aeromagnetic data (Pretorius, 1984) and the recent shear wave velocity model Botswana (Fadel et al., 2020).

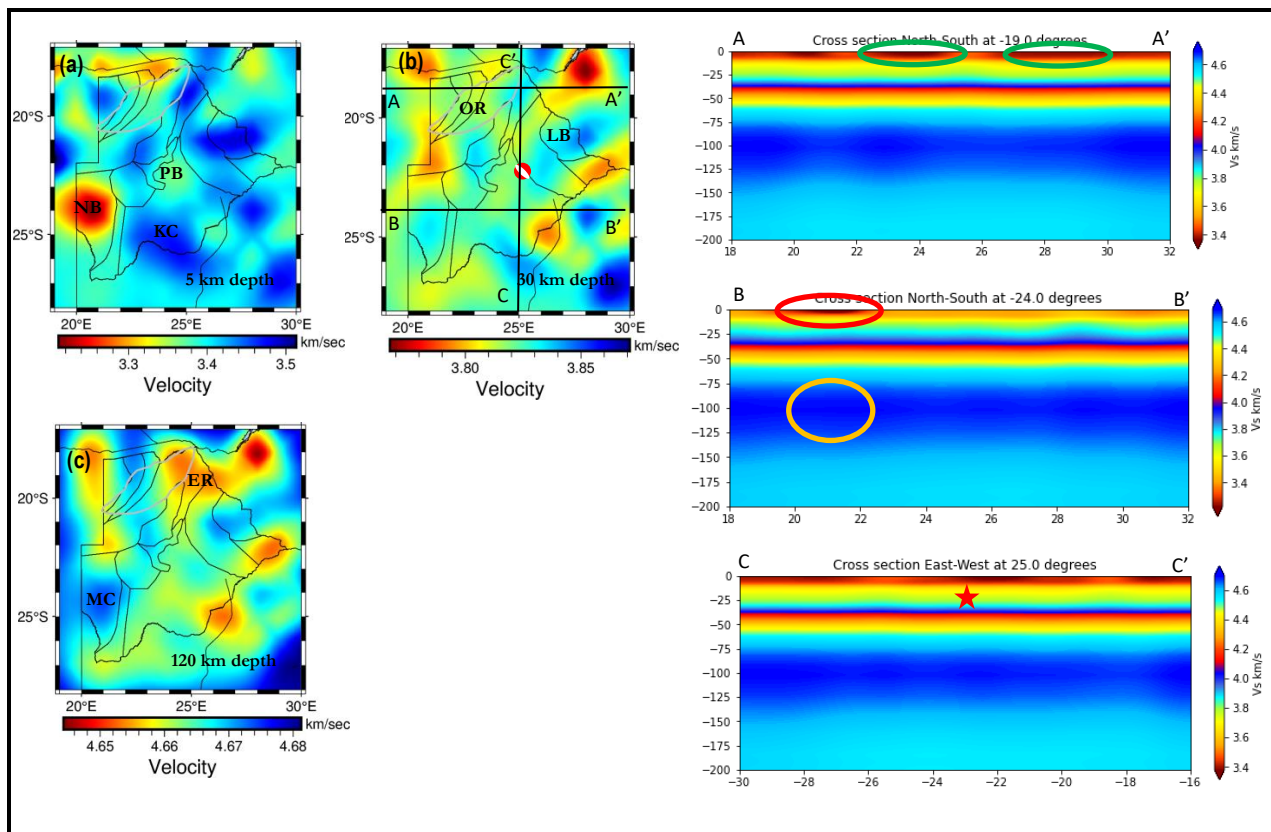


Figure 6.5: The 3D shear wave velocity model of Botswana. The location of the cross-section line is indicated in plot c. The location of the 3 April 2017 earthquake is indicated on the depth slice map. The shear wave velocity model shown here are the velocity contrast for crustal and upper mantle part. The green circle at A-A' shows the expected location of ORZ and surface expression of the EARS. The red circle shows at B-B' shows a low velocity anomaly seen at the Nosop basin. The orange circle shows the expected location of the MC craton. However, the depth extent is not clearly resolved. The red star indicates the location of the 2017, 3rd April earthquake epicentre. NB = Nosop Basin; PB = Passarge Basin; KC = Kalahari Craton; ORZ=Okavango Rift Zone; ZC = Zimbabwe Craton; LB = Limpopo Belt; ER = East African Rift System; CML = Colesberg Magnetic Lineament.

### 6.4.3. Malatahohe Micro-Craton (MC)

Below the Nosop sedimentary basin, a relatively positive shear wave velocity and density anomaly is observed (Figure 6.5 & Figure 6.6). The high shear wave velocity and density anomaly shown in the upper mantle below the Nosope Basin is observed as a separate structure from the western side of the Kaapvaal craton at the 30 & 120 km depth slices of Figure 6.5 & 6.6 b & c and cross-section B-B'. This finding contradicts one of the earliest investigations of the Nosop basin by write and Hall (1991), which proposed the existence of the micro-craton as the western extension of the Kaapvaal craton. From the depth slice and cross-section plot, the Kaapvaal craton is imaged as a positive shear wave velocity and density anomalies (Figure 6.5 & 6.6, a, and cross-section B-B').

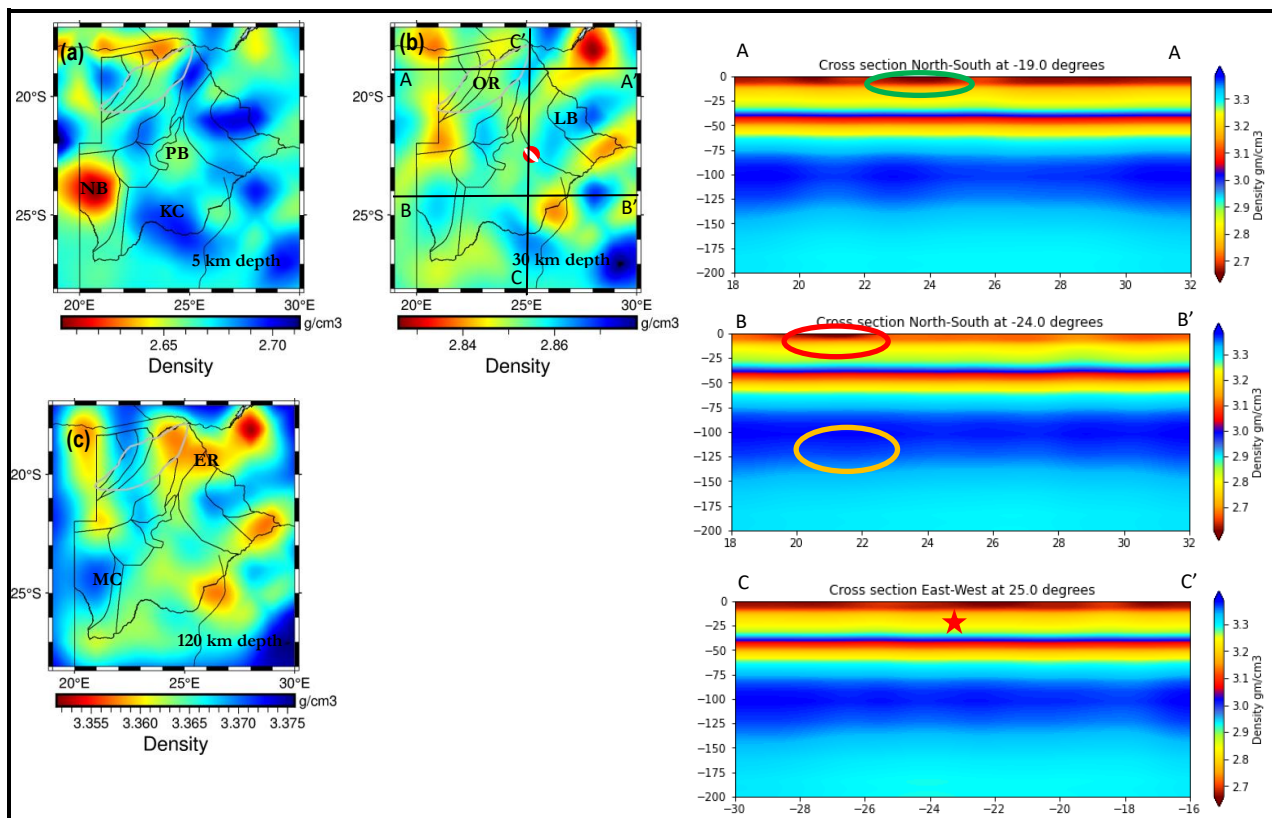


Figure 6.6: The 3D density contrast model of Botswana. The location of the cross-section line is indicated in plot b. The density contrast model shown here are the density contrast model plotted for crustal and upper mantle. The green circle at A-A' shows the expected location of ORZ and surface expression of the EARS. The red circle shows at B-B' shows a low velocity anomaly seen at the Nosop basin. The orange circle shows the expected location of the MC craton. However, the depth extent is not clearly resolved. The red star indicates the location of the 2017, 3rd April earthquake epicentre. NB = Nosop Basin; PB = Passarge Basin; KC = Kalahari Craton; ORZ=Okavango Rift Zone; ZC = Zimbabwe Craton; LB = Limpopo Belt; ER = East African Rift System; CML = Colesberg Magnetic Lineament.

The presence of high velocity and density structure below the Nosop sedimentary basin (Figure 6.6 c) coincides with some of the previous studies conducted in Botswana, suggesting the presence of a buried Micro-craton (Akinremi et al., 2022; Chisenga et al., 2020a; Fadel et al., 2020). This study also shows the presence of the micro-craton as a separate block from the Kaapvaal craton at depth slices 30 & 120 km in Figure 6.5 & Figure 6.6. This supports the idea that suggests the presence of buried micro-craton beneath the Nosop sedimentary basin that coincides with the shear wave velocity model from Fadel et al. (2020) and the recent MT studies of Akinremi et al. (2022). However, there is disagreement about the depth location of the micro-cratons in the literature. For example, the high shear wave velocity and density signature observed in this study does not coincide with the recently conducted shear wave velocity and MT study of Botswana. The MT study showed a highly conductive structure beneath the Nosop Basin at a depth of 10 - 100 km. On the other hand, the previously conducted shear wave velocity model also showed a high-velocity signature at a depth of 50 - 200 km. This study, on the other hand, revealed a high velocity and density structure at a depth of 30 - 150 km beneath the Rehoboth province. Beyond this, the true structure of the cratonic root was not resolved well. This discrepancy about the depth extent of the micro-craton could be associated with the thick sediment cover of the Nosope sedimentary basin at the top and the sparse coverage of seismic station and MT data that hinders the potential of the geophysical data to resolve the structure of the Maltahohe micro-craton. Moreover, the complex synthetic test presented in chapter 5 showed the smearing in retrieving the Maltahohe micro-craton, even within a synthetic setup. Therefore, despite some discrepancies about the depth extent of the cratonic root, this study confirms the existence of high velocity and density anomalies that support the existence of the buried Maltahohe micro craton beneath the sedimentary basin but reveal its depth between 30-150 km depth.

#### **6.4.4. ORZ and the Extension of EARS in Central Botswana and its Relationship with the Epicenter of the 2017 April 3<sup>rd</sup> 6.5 Mw Earthquake**

Another prominent feature that we can see is the extension of EARS in the northeastern tip of Botswana. The southward extension of EARS is interpreted to have its last surface expression near the northern tip of Botswana at Lake Kariba (e.g., Figure 1.1). According to the velocity and density model obtained from this study, low shear wave velocity and density signatures at 30 and 120 km are indicated, showing the shallower and deeper part of the possible extension of the EARS (depth slices 30 and 120 km in Figure 6.5 & Figure 6.6, b, c). This shallower low shear wave velocity and density anomaly coincides with the surface expression of the EARS extension around Lake Kariba (Figure 1.1) and is also linked with the low velocity and density anomalies at ORZ in Botswana at 120 kilometers depth slice as shown in Figure 6.5 & Figure 6.6, plot c. The low shear wave velocity and density anomaly at crustal depths are in agreement with the previous shear wave velocity and MT studies showing low shear wave velocity and conductivity structure (Akinremi et al., 2022 & Fadel et al., 2020, respectively). According to their finding, the migration of mantle fluids towards the surface is the cause of rifting in ORZ. Therefore, this study showed the connection of EARS surface expression at lake Kariba with the low-velocity anomaly at ORZ, contradicting the hypothesis argued by Pastier et al. (2017) as there is no rifting in ORZ.

The low velocity and density characteristics in northeastern Botswana, albeit being weak variations, show a connection with the central part of Botswana, where the 2017 earthquake of 6.5 Mw occurred (Figure 6.5 & Figure 6.6 b, c). This is also demonstrated by the recent work of the shear wave velocity model from single data inversion of the surface wave data (Fadel et al., 2020) and  $V_p/V_s$  ratio from the receiver function analysis (Fadel et al., 2018; Y. Yu et al., 2015). Furthermore, this hypothesis of rifting in the central part of Botswana was also supported by the recent crustal thickness map of Botswana derived from gravity data that shows a relatively thin crust beneath the epicenter of the 6.5 Mw earthquake (Chisenga et al., 2020b). According to their findings, the flow of hot fluids from the EARS extension eroded the lower crust, resulting in a thin crust compared to the neighboring Kaapvaal craton. Therefore, this consistent signature, albeit weakly, of low velocity and density anomaly derived from the joint inversion of gravity and surface wave data provides more convincing evidence supporting the extension of the EARS to central Botswana.

#### **6.4.5. Bushveld Complex and Colesberg Magnetic Lineament**

An interesting feature seen in the shear wave velocity and density model is the small blobs of low shear wave velocity and density anomalies in the southeastern part of the Kaapvaal craton around the Colesberg magnetic lineament shown in the 120 km depth slice map (120 km depth slices in Figure 6.5 & Figure 6.6). The location of the low-velocity anomaly beneath the Kaapvaal was also highlighted by previous research of the P and S wave velocity structure of the upper mantle of southern Africa (Fouch et al., 2004; Youssof et al., 2015). Further, Ortiz et al. (2019) & White-Gaynor et al. (2020), in their recent seismic studies, suggested the presence of low-velocity anomaly beneath the Kaapvaal craton attributed to the thermal or compositional modification of 2.05 Ga bushveld complex and /or magmatic events in the upper mantle. The highly conductive zone of the Bushveld complex was also observed in more recent MT studies of Botswana, corroborating the interpretation attributed to iron saturation of the mantle material from the Bushveld complex (Akinremi et al., 2022). The result from this study is in agreement with the location of the low velocity and high conductive zone around the Colesberg Magnetic Anomaly in the southeastern part of Botswana, showing low shear wave velocity and density anomaly in the joint inversion results. Therefore, remnant material from magma intrusion around the Bushveld complex beneath the Kaapvaal near the Colesberg magnetic lineament might explain the low velocity and density anomaly beneath the Kaapvaal craton.

#### **6.5. Data misfit**

Table 6.1 shows the RMSE of the data misfit between the observed data and model response after the joint inversion. From the table, the gravity data component has the highest RMSE values signifies the inversion result was less likely fitting the gravity data set than the surface wave data. Especially, the inversion result was not able to reproduce the gravity gradient data leading to high misfit values. The data misfit plot obtained from the joint inversion of the real data set are presented in Appendix 3, Figure 7.20 - Figure 7.22.

Table 6.1 RMSE of the data misfit for the real data joint inversion of gravity and surface wave data.

Inversions	Data used for the inversions	Data misfit RMSE	
		Variables	Values
Joint inversion of gravity and Surface-wave data	$g_z + g_{all}$	$g_z$	4.70
		$g_{zz}$	0.40
		$g_{xx}$	0.21
		$g_{yy}$	0.67
		$g_{xy}$	1.59
		$g_{xz}$	0.68
		$g_{yz}$	2.05
	group velocity	grp	0.37
	phase velocity	phs	0.36

In general, the inversion results reported in this chapter are incomplete and require additional trials of the joint inversion with varying weights of the data set and model parameters to determine the appropriate model parameters for the inversion. Only a few trials of the joint inversion were conducted due to time constraints, and further trials of the inversion might give us a more detailed and interpretable features. From the inversion result presented above and data misfit analysis, the effect of model damping and smoothness constraints was significant for the inversion result. Therefore, the absolute shear wave velocity model presented above showed a weak variation of velocity values and unrealistic velocity variation specially at deeper depths after 120 km in comparison with the previously conducted shear wave velocity model of Botswana (Fadel et al., 2020). The weak resolving power of the inversion seen at deeper depths could be associated with the combined effect of decreasing sensitivity of the measured surface wave data at deeper depths and the damping effect applied in the joint inversion. Furthermore, the variable model discretization and depth extent conducted in the previous research of Fadel et al. (2020) (410 km inversion with 2.5 km depth discretization in the uppermost part 0-15 km, 5 km depth discretization for depth range between 15 – 50 km, 10 km for the depth from 50 – 100 km, and finally, a 20 km depth interval till 410 km ) and the constant 5 km depth discretization conducted in this inversion might be the possible cause of weak variation of the shear wave velocity and density values at a deeper depths after 125 km. According to Fadel et al. (2020) the variable discretization of the model till 410 km helps to prevent leakage of the deeper structure artifacts to shallower depths. However, the discretization of the Earth model till 200 km only conducted in this research might be the cause of the unrealistic shear wave velocity and density values after 120 km. Furthermore, Fadel et al. (2020) used the velocity density conversion of Brochure (2005) for crustal part of the model for velocity < 4.1 km/sec only. They kept fixed ratio of the density and  $V_p$  to AK135 global reference shear wave velocity model for  $V_s > 4.1$  km/s in the upper mantle part of the model. In this research, however, the joint inversion approach was designed using the Brocher (2005) relation of velocity and density for the crustal and upper mantle part of the Earth, which might have led to unrealistic density and  $V_p$  conversion in the upper mantle part.

## 7. CONCLUSIONS AND RECOMMENDATION

In this chapter, the conclusion and recommendations for future work are presented based on the author's perspective of the study and the limitations of the research.

### 7.1. Conclusions

In this research, a new method that jointly integrates gravity and seismic surface wave data are implemented. The joint inversion approach is used to model the velocity and density structure of the subsurface model simultaneously. The method uses a Levenberg-Marquardt algorithm, also called damped least square algorithm to minimize the objective function. During the method's development, a 3D finite difference approach was employed to approximate the Jacobian in the misfit function. However, the 3D finite difference scheme that iterates through each cell of the 3D cube was computationally expensive which made the method less effective to apply for high-resolution regional or continental modelling. However, the research used an updated version of the joint inversion method to approximate the Jacobian using the 1D finite difference scheme over the grid points instead of the 3D finite difference scheme, which significantly accelerated the algorithm. Therefore, a synthetic test of the method was conducted to test and understand how efficient the method is in terms of computational cost with the available computing machine and its scalability. Thus, the research conducted two phases of synthetic tests simulating the GOCE satellite gravity data and the fundamental mode Rayleigh wave group and phase velocity dispersion. The first phase used a simple model that contains two positive and negative anomalies at the center of the model. The second phase of the synthetic test on the other hand, was a more complicated model that mimics Botswana geology considering the real data application of the method in Botswana.

During both phases of the method test, three scenarios of inversion were conducted: the gravity data only inversion for density, the surface wave only inversion for velocity and the joint inversion of gravity and surface wave data for density and velocity modelling. Both synthetic method tests help us understand the efficiency of the joint inversion approach and how it is affected by the inversion parameters. Furthermore, the added value of the different data sets used was evaluated during single data and joint data inversion. Therefore, using the complementary advantage of the two data sets, the joint inversion approach obtained a single model with different physical properties that simultaneously fit the two geophysical data sets. The joint inversion of all data sets solved a number of issues brought on by the individual inversion of the data set and then enhance the inversion resolving power. As a result, the ambiguity or non-uniqueness typical of geophysical inversion was greatly reduced by the joint inversion of the two data sets.

At the later stage of this research, the joint inversion approach was applied using real data measurements of satellite gravity and seismic surface wave data to model the velocity and density distribution of Botswana's crust and uppermost mantle. The results and observations presented in this chapter are the first step and need additional work to be able to improve the inversion process and understand the influences of the used parameters on the real data implementation in a more detailed manner. However, in this study, an attempt to explain some of the observed features in the inverted velocity and density model were explained about some of the debated tectonic questions of Botswana for the first time using a nation-wide joint inversion

approach of satellite gravity and seismic surface wave data. Those are the presence of MC and its linkage with the adjacent Kaapvaal cratons, the presence and southward extension of EARS in ORZ and to central Botswana and its linkage with the 2017 6.5 Mw earthquake epicenter. Below are the research questions answered by this study are presented:

**Research questions: -**

- How efficient is the existing inversion approach to model the subsurface velocity and density distribution at different resolutions?

The two phases of the method test help us to understand how efficient the method was in terms of integrating both gravity and surface wave data. The result from the two phases of method test proves that the surface wave Jacobian calculation using the 1D finite difference scheme significantly improves the performance of the method to apply for high-resolution modelling. The first phase of the method test using a simple model took a maximum of 15 minutes to complete the inversion, which was taking more than 24 hours before method improvement using the available computing machine. The second phases of method test using complicated model was completed after 60 iteration that took an approximately of 8 hrs. Therefore, the result from the synthetic test suggests that the method is efficient in terms of computational cost to conduct regional case studies and also retrieving the subsurface information.

- How the model parameters affect the inversion result and how to adjust them efficiently?

The inversion model parameter was an important controlling factor that governs the inversion process. Data weighting and model regularization parameter were defined to get an optimal inversion result. The data weighting was defined based on trial and error of using a weighted normalization scheme to select an appropriate value for each data set. Therefore, from the inversion, large values of one data weighting contribute to the poor fitting of the data set over another data set. The other model parameter, regularization parameter (i.e., the smoothness parameter and damping weight) affects the inversion result. Large values of the smoothness parameter and damping weight produce a very smooth model that resembles almost the starting model without retrieving the basic structure of the true model. This results also poor data fit. On the other hand, small smoothness and damping parameter produces a rough model with some artifacts in the inversion result but produces a good quality of data fit. Therefore, after trial and error of several numbers a value that results a model close to the true model and that simultaneously fit the two data set was considered in the inversion. Therefore, a number of inversions with trial and error was conducted to define each parameter.

- What is the added value of GOCE gravity gradient data on the developed density model?

In this thesis, individual and joint inversion of the data set was conducted to understand the added values of each data set in the inversion. During the first phase of the method test, the added values of the unique GOCE gravity gradient data was evaluated. From the analysis of the gravity only and joint inversion of gravity and surface wave data, it was possible to suggested that the gradient data might contain an additional information for subsurface density modelling (especially for the crustal and uppermost mantle part). Because the RMSE analysis from the inversion result demonstrates that the resolving power of the density structure was improved till a depth of 30 km and remains constant or increases at some depths.

- Can the inverted velocity and density model help to confirm the existence of buried micro-craton?

Yes, the inverted velocity and density model revealed a high velocity and density signature beneath the Nosop basin at the Rehoboth province, which indicated the possible existence of the buried Maltahohe micro-craton.

- If the existence of the micro-craton is confirmed, what are the depth and spatial extent of the boundaries?

The spatial extent of the MC is found as a separate structure from the Kaapvaal craton. However, the inversion result does not accurately determine the depth extent of the MC below the Nosop Basin. The results from the complex synthetic test that mimics Botswana geology also suggested that retrieving the accurate depth extent of MC is uncertain using the existing datasets.

- Can the inverted velocity-density model indicate and map the presence of rifting along the Okavango zone?

Yes, the 3-D inverted velocity and density model showed the presence of rifting at the ORZ, showing low velocity and density signature.

- Can the inverted velocity-density model indicate the extension of EARS to central Botswana?

Yes, the 3-D velocity and density model from the joint inversion approach conducted in this study showed an indication of low velocity and density below the epicenter of the April 3<sup>rd</sup> earthquake. This supports the linkage of the EARS extension towards central Botswana, as indicated from the previously conducted seismic studies.

## 7.2. Recommendations

In this section, some of the recommendations for future studies is suggested.:

1. Even though the synthetic tests prove that the joint inversion works and is efficient with the available computing machine, there is room for further development of the method. For example, the Brocher (2005) relation of velocity and density works for crustal materials. However, the relation can be violated for deep subsurface in the upper mantle e.g., in the existing molten material where there is a very low-velocity zone. Therefore, to increase the reliability of the information that we retrieve, mineral physics and thermochemical relation of subsurface material could be applied.
2. Finding an optimum data weighting for the different components of data types was the most difficult part of the inversion. The method applied a weight normalization scheme based on the difference between the maximum and minimum values of the data. However, this approach needs several steps of trial and error to adjust them efficiently. Therefore, a weighting scheme based on the number of data points, as implemented by Julià et al. (2000) will be an ideal solution to efficiently weight the data set in least-square inversion. Moreover, exploration for automatic techniques could be very useful and accelerate the whole joint inversion workflow significantly.

3. The gravity data lack inherent depth resolution, which makes it difficult to determine the source of the signals. Surface wave tomography or surface wave inversion, on the other hand, suffers from vertical trade-off (only sensitive to average Vs at some depth range). To address the aforementioned issues with the two data sets, additional geophysical data, e.g., receiver function results or magnetotelluric data, can be added to the joint inversion scheme to increase the resolving power of the inversion approach using a direct parameter density-velocity-resistivity coupling or cross gradient coupling techniques.
  
4. Finally, for the real data implementation of the joint inversion to study the crustal and uppermost mantle of Botswana, further study is needed to use the full capabilities of the two data set used. The inversion was highly dependent on the starting model used. In this study, I used the average shear wave velocity model of the study area that could fit only the surface wave data but not the global satellite gravity data. As a result, fitting the gravity data was the major problem of the inversion processes. To solve this issues, further testing of the real data application could be done and conducted using the new global reference model of LithoRef18 from Afonso et al. (2019b) as a starting model for the inversion that is at a coarser (depth) resolution but is both gravity and seismological consistent Earth model.

## LIST OF REFERENCES

---

- A. Wright, J., Hall, J., 1990. Deep Seismic profiling in the Nosop Basin, Botswana: cratons, mobile belts and sedimentary basins. *Tectonophysics* 173, 333–343. [https://doi.org/10.1016/0040-1951\(90\)90228-Z](https://doi.org/10.1016/0040-1951(90)90228-Z)
- Afonso, J.C., Moorkamp, M., Fullea, J., 2016. Imaging the Lithosphere and Upper Mantle: Where We Are At and Where We Are Going, in: *Integrated Imaging of the Earth: Theory and Applications*. American Geophysical Union (AGU) and John Wiley and Sons .Inc, Washington, D.C., pp. 191–218. <https://doi.org/10.1002/9781118929063.CH10>
- Afonso, J.C., Salajegheh, F., Szwillus, W., Ebbing, J., Gaina, C., 2019a. A global reference model of the lithosphere and upper mantle from joint inversion and analysis of multiple data sets. *Geophys. J. Int.* 217, 1602–1628. <https://doi.org/10.1093/gji/ggz094>
- Afonso, J.C., Salajegheh, F., Szwillus, W., Ebbing, J., Gaina, C., 2019b. A global reference model of the lithosphere and upper mantle from joint inversion and analysis of multiple data sets. *Geophys. J. Int.* 217, 1602–1628. <https://doi.org/10.1093/gji/ggz094>
- Akinremi, S., Fadel, I., Van Der Meijde, M., 2022. Crustal and upper mantle imaging of Botswana using magnetotelluric method.
- Begg, G.C., Griffin, W.L., Natapov, L.M., O'Reilly, S.Y., Grand, S.P., O'Neill, C.J., Hronsky, J.M.A., Djomani, Y.P., Swain, C.J., Deen, T., Bowden, P., 2009. The lithospheric architecture of Africa: Seismic tomography, mantle petrology, and tectonic evolution. *Geosphere* 5, 23–50. <https://doi.org/10.1130/GES00179.1>
- Black, R., Liegeois, J.P., 1993. Cratons, mobile belts, alkaline rocks and continental lithospheric mantle: the Pan-African testimony. *J. - Geol. Soc.* 150, 89–98. <https://doi.org/10.1144/gsjgs.150.1.0088>
- Blom, N., Boehm, C., Fichtner, A., 2017. Synthetic inversions for density using seismic and gravity data. *Geophys. J. Int.* 209, 1204–1220. <https://doi.org/10.1093/gji/ggx076>
- Bouman, J., Ebbing, J., Fuchs, M., Sebera, J., Lieb, V., Szwillus, W., Haagmans, R., Novak, P., 2016. Satellite gravity gradient grids for geophysics. *Sci. Rep.* 6, 1–11. <https://doi.org/10.1038/srep21050>
- Bouman, J., Ebbing, J., Meekes, S., Fattah, R.A., Fuchs, M., Gradmann, S., Haagmans, R., Lieb, V., Schmidt, M., Dettmering, D., Bosch, W., 2015. GOCE gravity gradient data for lithospheric modeling. *Int. J. Appl. Earth Obs. Geoinf.* 35, 16–30. <https://doi.org/10.1016/j.jag.2013.11.001>
- Brocher, T.M., 2005. Empirical relations between elastic wavespeeds and density in the Earth's crust. *Bull. Seismol. Soc. Am.* 95, 2081–2092. <https://doi.org/10.1785/0120050077>
- Capriotti, J., Li, Y., 2021. Joint inversion of gravity and gravity gradient data: A systematic evaluation. *Geophysics* 87, 326–329. <https://doi.org/10.1190/geo2020-0729.1>
- Chisenga, C., Jianguo, Y., Fadel, I., van der Meijde, M., Atekwana, E.A., 2020a. Updated tectonic terrane boundaries of Botswana determined from gravity and aeromagnetic data. *Episodes* 43, 919–933. <https://doi.org/10.18814/EPIUGS/2020/020054>

- Chisenga, C., Van der Meijde, M., Yan, J., Fadel, I., Atekwana, E.A., Steffen, R., Ramotoroko, C., 2020b. Gravity derived crustal thickness model of Botswana: Its implication for the Mw 6.5 April 3, 2017, Botswana earthquake. *Tectonophysics* 787. <https://doi.org/10.1016/j.tecto.2020.228479>
- Cockett, R., Kang, S., Heagy, L.J., Pidlisecky, A., Oldenburg, D.W., 2015. SimPEG: An open source framework for simulation and gradient based parameter estimation in geophysical applications. *Comput. Geosci.* 85, 142–154. <https://doi.org/10.1016/j.cageo.2015.09.015>
- Corner, B., Durrheim, R.J., 2018. *An Integrated Geophysical and Geological Interpretation of the Southern African Lithosphere, Geology of Southwest Gondwana.* Springer International Publishing. [https://doi.org/10.1007/978-3-319-68920-3\\_2](https://doi.org/10.1007/978-3-319-68920-3_2)
- Fadel, I., 2018. Crustal and upper mantle structure of Botswana : is Botswana rifting? Islam Fadel.
- Fadel, I., Paulssen, H., van der Meijde, M., Kwadiba, M., Ntibinyane, O., Nyblade, A., Durrheim, R., 2020. Crustal and Upper Mantle Shear Wave Velocity Structure of Botswana: The 3 April 2017 Central Botswana Earthquake Linked to the East African Rift System. *Geophys. Res. Lett.* 47. <https://doi.org/10.1029/2019GL085598>
- Fadel, I., van der Meijde, M., Paulssen, H., 2018. Crustal Structure and Dynamics of Botswana. *J. Geophys. Res. Solid Earth* 123, 10,659-10,671. <https://doi.org/10.1029/2018JB016190>
- Förste, C., Bruinsma, S.L., Abrikosov, O., Lemoine, J.-M., Schaller, T., Götze, H.-J., Ebbing, J., Marty, J.C., Flechtner, F., Balmino, G., Biancale, R., 2015. EIGEN-6C4 The latest combined global gravity field model including GOCE data up to degree and order 2190 of GFZ Postdam and GRGS Toulouse. 5th GOCE User Work.
- Fouch, M.J., James, D.E., VanDecar, J.C., van der Lee, S., 2004. Mantle seismic structure beneath the Kaapvaal and Zimbabwe Cratons. *South African J. Geol.* 107, 33–44. <https://doi.org/10.2113/107.1-2.33>
- Haddon, I.G., 2005. *The Sub-Kalahari Geology and Tectonic Evolution of the Kalahari Basin, Southern Africa.* PhD Thesis, Fac. Sci. Univ. Witwatersrand, Johannesburg. 1–360.
- J. Ebbing, J. Bouman, M. Fuchs, S. Gradmann, and R.H., 2014. Sensitivity of GOCE Gravity Gradients to Crustal Thickness and Density Variations: Case Study for the Northeast Atlantic Region. *Int. Assoc. Geod. Symp.* 141, vii–viii. <https://doi.org/10.1007/978-3-319-10837-7>
- Jelsma, H.A., Dirks, P.H.G.M., 2002. Neoarchaean tectonic evolution of the Zimbabwe Craton. *Geol. Soc. Spec. Publ.* 199, 183–211. <https://doi.org/10.1144/GSL.SP.2002.199.01.10>
- Julià, J., Ammon, C.J., Herrmann, R.B., Correig, A.M., 2000. Joint inversion of receiver function and surface wave dispersion observations. *Geophys. J. Int.* 143, 99–112. <https://doi.org/10.1046/j.1365-246X.2000.00217.x>
- Kaban, M.K., Mooney, W.D., 2001. Density structure of the lithosphere in the southwestern United States and its tectonic significance. *J. Geophys. Res. Solid Earth* 106, 721–739.

<https://doi.org/10.1029/2000jb900235>

- Kaban, M.K., Stolk, W., Tesauro, M., El Khrepy, S., Al-Arifi, N., Beekman, F., Cloetingh, S.A.P.L., 2016. 3D density model of the upper mantle of Asia based on inversion of gravity and seismic tomography data. *Geochemistry, Geophys. Geosystems* 17, 4457–4477. <https://doi.org/10.1002/2016GC006458>
- Ke, X., Tian, M., Guan, D., Wang, Y., Shi, H., 2019. Gravitational gradients derived from GOCE and density structures beneath the North China Craton. *J. Asian Earth Sci.* 174, 152–166. <https://doi.org/10.1016/j.jseas.2018.12.002>
- Kennett, B.L.N., Engdahl, E.R., Buland, R., 1995. Constraints on seismic velocities in the Earth from traveltimes. *Geophys. J. Int.* 122, 108–124. <https://doi.org/10.1111/j.1365-246X.1995.tb03540.x>
- Key, R.M., Ayres, N., 2000. The 1998 edition of the National Geological Map of Botswana. *J. African Earth Sci.* 30, 427–451. [https://doi.org/10.1016/S0899-5362\(00\)00030-0](https://doi.org/10.1016/S0899-5362(00)00030-0)
- Khoza, D., Jones, A., Muller, M., Evans, R., Miensopust, M., Webb, S., 2013. Lithospheric structure of an Archean craton and adjacent mobile belt revealed from 2-D and 3-D inversion of magnetotelluric data: Example from southern Congo craton in northern Namibia. *J. Geophys. Res. Solid Earth* 118, 4378–4397. <https://doi.org/10.1002/jgrb.50258>
- Kinabo, B.D., Atekwana, E.A., Hogan, J.P., Modisi, M.P., Wheaton, D.D., Kampunzu, A.B., 2007. Early structural development of the Okavango rift zone, NW Botswana. *J. African Earth Sci.* 48, 125–136. <https://doi.org/10.1016/j.jafrearsci.2007.02.005>
- Kolawole, F., Atekwana, E.A., Malloy, S., Stamps, D.S., Grandin, R., Abdelsalam, M.G., Leseane, K., Shemang, E.M., 2017. Aeromagnetic, gravity, and Differential Interferometric Synthetic Aperture Radar analyses reveal the causative fault of the 3 April 2017 Mw 6.5 Moyabana, Botswana, earthquake. *Geophys. Res. Lett.* 44, 8837–8846. <https://doi.org/10.1002/2017GL074620>
- Koslovskaya, E., Elo, S., Hjelt, S.E., Yliniemi, J., Pirttijärvi, M., 2004. 3-D density model of the crust of southern and central Finland obtained from joint interpretation of the SVEKALAPKO crustal P-wave velocity models and gravity data. *Geophys. J. Int.* 158, 827–848. <https://doi.org/10.1111/j.1365-246X.2004.02363.x>
- Lenczuk, A., Bogusz, J., Olszak, T., Barlik, M., 2019. Studying the sensitivity of GOCE gravity gradients to the crustal structure: case study of Central Europe. *Acta Geod. Geophys.* 54, 19–34. <https://doi.org/10.1007/S40328-019-00250-Y>
- Leseane, K., Atekwana, Estella A., Mickus, K.L., Abdelsalam, M.G., Shemang, E.M., Atekwana, Eliot A., 2015. Thermal perturbations beneath the incipient Okavango Rift Zone, northwest Botswana. *J. Geophys. Res. Solid Earth* 3782–3803. <https://doi.org/10.1002/2015JB012608>.Received
- Li, Y., Oldenburg, D.W., 1995. 3-D inversion of Gravity Data. 1995 SEG Annu. Meet. 63, 264–267. <https://doi.org/10.1190/1.1887478>
- Liao, C., Hu, X., Zhang, S., Li, X., Yin, Q., Zhang, Z., Zhang, L., 2021. Joint inversion of gravity, magnetotelluric and seismic data using the alternating direction method of multipliers. *Geophys. J. Int.* 229, 203–218. <https://doi.org/10.1093/gji/ggab463>

- Lintern, D.G., Hill, P.R., Stacey, C., 2016. Total of 10 pages only may be xeroxed, *Sedimentology*.
- Maccira, M., Ammon, C.J., 2009. Joint inversion of surface wave velocity and gravity observations and its application to central Asian basins shear velocity structure. *J. Geophys. Res. Solid Earth* 114, 1–18. <https://doi.org/10.1029/2007JB005157>
- Macgregor, D., 2015. History of the development of the East African Rift System: A series of interpreted maps through time. *J. African Earth Sci.* 101, 232–252. <https://doi.org/10.1016/j.jafrearsci.2014.09.016>
- Magrini, F., Diaferia, G., Fadel, I., Cammarano, F., Van Der Meijde, M., Boschi, L., 2020. 3-D shear wave velocity model of the lithosphere below the Sardinia-Corsica continental block based on Rayleigh-wave phase velocities. *Geophys. J. Int.* 220, 2119–2130. <https://doi.org/10.1093/gji/ggz555>
- Meneghini, F., Fagereng, Å., Kisters, A., 2017. The matchless amphibolite of the Damara Belt, Namibia: Unique preservation of a late neoproterozoic ophiolitic suture. *Ophioliti* 42, 129–145. <https://doi.org/10.4454/phioliti.v42i2.452>
- Midzi, V., Saunders, I., Manzunzu, B., Kwadiba, M.T., Jele, V., Mantsha, R., Marimira, K.T., Mulabisana, T.F., Ntibinyane, O., Pule, T., Rathod, G.W., Sitali, M., Tabane, L., van Aswegen, G., Zulu, B.S., 2018. The 03 April 2017 Botswana M6.5 earthquake: Preliminary results. *J. African Earth Sci.* 143, 187–194. <https://doi.org/10.1016/j.jafrearsci.2018.03.027>
- Modie, B.N., 2000. Geology and mineralisation in the Meso- to Neoproterozoic Ghanzi-Chobe Belt of northwest Botswana. *J. African Earth Sci.* 30. [https://doi.org/10.1016/S0899-5362\(00\)00032-4](https://doi.org/10.1016/S0899-5362(00)00032-4)
- Modisi, M.P., 2000. Fault system at the southeastern boundary of the Okavango Rift, Botswana. *J. African Earth Sci.* 30, 569–578. [https://doi.org/10.1016/S0899-5362\(00\)00039-7](https://doi.org/10.1016/S0899-5362(00)00039-7)
- More, J.J., 1978. The levenberg-marquardt algorithm: implementation and theory. *Springer* 105–116.
- Oriolo, S., Becker, T., 2018. The Kalahari Craton, Southern Africa: From Archean Crustal Evolution to Gondwana Amalgamation, *Geology of Southwest Gondwana*. Springer International Publishing. [https://doi.org/10.1007/978-3-319-68920-3\\_6](https://doi.org/10.1007/978-3-319-68920-3_6)
- Ortiz, K., Nyblade, A., van der Meijde, M., Paulssen, H., Kwadiba, M., Ntibinyane, O., Durrheim, R., Fadel, I., Homman, K., 2019. Upper Mantle P and S Wave Velocity Structure of the Kalahari Craton and Surrounding Proterozoic Terranes, Southern Africa. *Geophys. Res. Lett.* 46, 9509–9518. <https://doi.org/10.1029/2019GL084053>
- Panet, I., Pajot-Métivier, G., Greff-Lefftz, M., Métivier, L., Diament, M., Manda, M., 2014. Mapping the mass distribution of Earth's mantle using satellite-derived gravity gradients. *Nat. Geosci.* 7, 131–135. <https://doi.org/10.1038/ngeo2063>
- Paoletti, V., Fedi, M., Italiano, F., Florio, G., Ialongo, S., 2016. Inversion of gravity gradient tensor data: Does it provide better resolution? *Geophys. J. Int.* 205, 192–202. <https://doi.org/10.1093/gji/ggw003>

- Pastier, A.M., Dauteuil, O., Murray-Hudson, M., Moreau, F., Walpersdorf, A., Makati, K., 2017. Is the Okavango Delta the terminus of the East African Rift System? Towards a new geodynamic model: Geodetic study and geophysical review. *Tectonophysics* 712–713, 469–481. <https://doi.org/10.1016/j.tecto.2017.05.035>
- Paulssen, H., Micallef, T., Bouwman, D.R., Ruigrok, E., Herman, M.W., Fadel, I., van der Meijde, M., Kwadiba, M., Maritinkole, J., Ntibinyane, O., 2022. Rifting of the Kalahari Craton Through Botswana? New Seismic Evidence. *J. Geophys. Res. Solid Earth* 127, 1–17. <https://doi.org/10.1029/2021JB023524>
- Reeves, C. V., Hutchins, D.G., 1982. A progress report on the geophysical exploration the kalahari in botswana of Botswana is a land-locked country whose immediate neighbours - South Africa , Namibia , Zambia and Zimbabwe - all enjoy a considerable degree of mineral wealth , derived in large 20, 209–224.
- Roecker, S., Ebinger, C., Tiberi, C., Mulibo, G., Ferdinand-Wambura, R., Mtelela, K., Kianji, G., Muzuka, A., Gautier, S., Albaric, J., Peyrat, S., 2017. Subsurface images of the Eastern Rift, Africa, from the joint inversion of body waves, surface waves and gravity: Investigating the role of fluids in early-stage continental rifting. *Geophys. J. Int.* 210, 931–950. <https://doi.org/10.1093/gji/ggx220>
- Roux, E., Moorkamp, M., Jones, A.G., Bischoff, M., Endrun, B., Lebedev, S., Meier, T., 2011. Joint inversion of long-period magnetotelluric data and surface-wave dispersion curves for anisotropic structure: Application to data from Central Germany. *Geophys. Res. Lett.* 38. <https://doi.org/10.1029/2010GL046358>
- Shen, W., Ritzwoller, M.H., Schulte-Pelkum, V., Lin, F.C., 2013. Joint inversion of surface wave dispersion and receiver functions: A Bayesianmonte-Carlo approach. *Geophys. J. Int.* 192, 807–836. <https://doi.org/10.1093/gji/ggs050>
- Simon, R.E., O, K.M.T., Moidaki, M., 2012. A History of Botswana ' s Seismic Network Author ( s ): RE Simon , MTO Kwadiba , JG King and M Moidaki Source : Botswana Notes and Records , 2012 , Vol . 44 ( 2012 ) , pp . 184-192 Published by: Botswana Society Stable URL : <http://www.jstor.com/stable/43>. *Botsw. Notes Rec.* 44, 184–192.
- Syracuse, E.M., Zhang, H., Maceira, M., 2017. Joint inversion of seismic and gravity data for imaging seismic velocity structure of the crust and upper mantle beneath Utah, United States. *Tectonophysics* 718, 105–117. <https://doi.org/10.1016/j.tecto.2017.07.005>
- Thomas, R.J., von Veh, M.W., McCourt, S., 1993. The tectonic evolution of southern Africa: an overview. *J. African Earth Sci.* 16, 5–24. [https://doi.org/10.1016/0899-5362\(93\)90159-N](https://doi.org/10.1016/0899-5362(93)90159-N)
- Tinker, J.H., de Wit, M.J., Royden, L.H., 2004. Old, strong continental lithosphere with weak Archaean margin at ~1.8 Ga, Kaapvaal Craton, South Africa. *South African J. Geol.* 107, 255–260. <https://doi.org/10.2113/107.1-2.255>
- Uieda, L., Barbosa, V.C.F., Braitenberg, C., 2016. Tesseroids: Forward-modeling gravitational fields in spherical coordinates. *Geophysics* 81, F41–F48. <https://doi.org/10.1190/GEO2015-0204.1>
- Uieda, L., Wessel, P., 2019. PyGMT: Accessing the Generic Mapping Tools from Python. AGU Fall Meet.

2019 NS21B-0813.

- van der Meijde, M., Pail, R., Bingham, R., Floberghagen, R., 2015. GOCE data, models, and applications: A review. *Int. J. Appl. Earth Obs. Geoinf.* 35, 4–15. <https://doi.org/10.1016/j.jag.2013.10.001>
- Van Schijndel, V., 2013. Precambrian Crustal Evolution of the Rehoboth Province, Southern Africa. Ale Tryckteam AB, Bohus.
- Van Schijndel, V., Cornell, D.H., Frei, D., Simonsen, S.L., Whitehouse, M.J., 2014. Crustal evolution of the rehoboth province from archaean to mesoproterozoic times: Insights from the rehoboth basement inlier. *Precambrian Res.* 240, 22–36. <https://doi.org/10.1016/j.precamres.2013.10.014>
- Van Schijndel, V., Cornell, D.H., Hoffmann, K.H., Frei, D., 2011. Three episodes of crustal development in the Rehoboth Province, Namibia. *Geol. Soc. Spec. Publ.* 357, 27–47. <https://doi.org/10.1144/SP357.3>
- Victor, T., Julià, J., White, N.J., Rodríguez-Tribaldos, V., 2020. Joint inversion of high-frequency receiver functions and surface-wave dispersion: Case study in the parnaíba basin of Northeast Brazil. *Bull. Seismol. Soc. Am.* 110, 1372–1386. <https://doi.org/10.1785/0120190203>
- White-Gaynor, A.L., Nyblade, A.A., Durrheim, R., Raveloson, R., van der Meijde, M., Fadel, I., Paulssen, H., Kwadiba, M., Ntibinyane, O., Titus, N., Sitali, M., 2020. Lithospheric Boundaries and Upper Mantle Structure Beneath Southern Africa Imaged by P and S Wave Velocity Models. *Geochemistry, Geophys. Geosystems* 21, 1–20. <https://doi.org/10.1029/2020GC008925>
- Wu, P., Tan, H., Ding, Z., Kong, W., Peng, M., Wang, X., Xu, L., 2022. Joint inversion of 3-D magnetotelluric and ambient noise dispersion data sets with cross-gradient constraints: methodology and application. *Geophys. J. Int.* 230, 714–732. <https://doi.org/10.1093/gji/ggac049>
- Youssof, M., Thybo, H., Artemieva, I.M., Levander, A., 2015. Upper mantle structure beneath southern African cratons from seismic finite-frequency P- and S-body wave tomography. *Earth Planet. Sci. Lett.* 420, 174–186. <https://doi.org/10.1016/j.epsl.2015.01.034>
- Yu, Y., Liu, K.H., Huang, Z., Zhao, D., Reed, C.A., Moidaki, M., Lei, J., Gao, S.S., 2017. Mantle structure beneath the incipient Okavango rift zone in southern Africa. *Geosphere* 13, 102–111. <https://doi.org/10.1130/GES01331.1>
- Yu, Y., Liu, K.H., Reed, C.A., Moidaki, M., Mickus, K., Atekwana, E.A., Gao, S.S., 2015. A joint receiver function and gravity study of crustal structure beneath the incipient Okavango Rift, Botswana. *Geophys. Res. Lett.* 42, 8398–8405. <https://doi.org/10.1002/2015GL065811>
- Yu, Youqiang, Liu, K.H., Reed, C.A., Moidaki, M., Mickus, K., Atekwana, E.A., Gao, S.S., 2015. A joint receiver function and gravity study of crustal structure beneath the incipient Okavango Rift, Botswana. *Geophys. Res. Lett.* 42, 8398–8405. <https://doi.org/10.1002/2015GL065811>

JOINT INVERSION OF SATELLITE GRAVITY AND SEISMIC SURFACE WAVE DATA: A SYNTHETIC TEST AND ITS APPLICATION FOR BOTSWANA CRUST AND UPPER  
MOST MANTLE VELOCITY AND DENSITY MODELING

## APPENDIX:

### Appendix 1: First phase synthetic method test using simple geologic model

1.1. A 3D starting model constructed from the interpolated AKA135 global reference velocity (A) and couple density (B) model used for the first phase of method test.

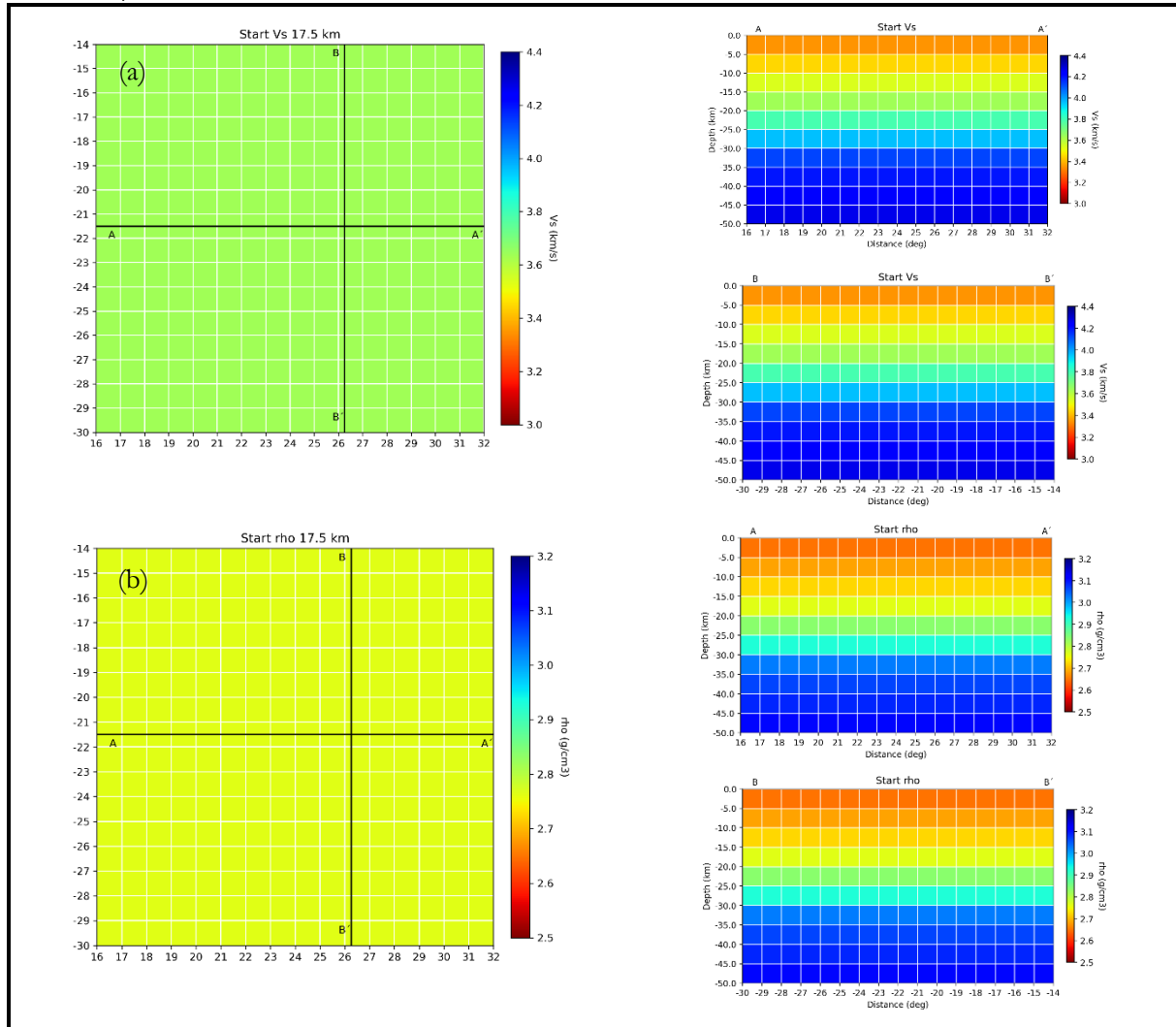


Figure 7.1: Starting model used for the inversion. Plot (a) shows the interpolated velocity model from the global AKA135 with the cross-section along the profile lines A-A' and B-B'. Plot (b) shows the derived density model from the velocity model using the Brocher relation of density and velocity with the corresponding cross-section of lines A-A' and B-B'.

## 1.2. Density contrast model expressed in Kg/m<sup>3</sup> used for the gravity signal calculations

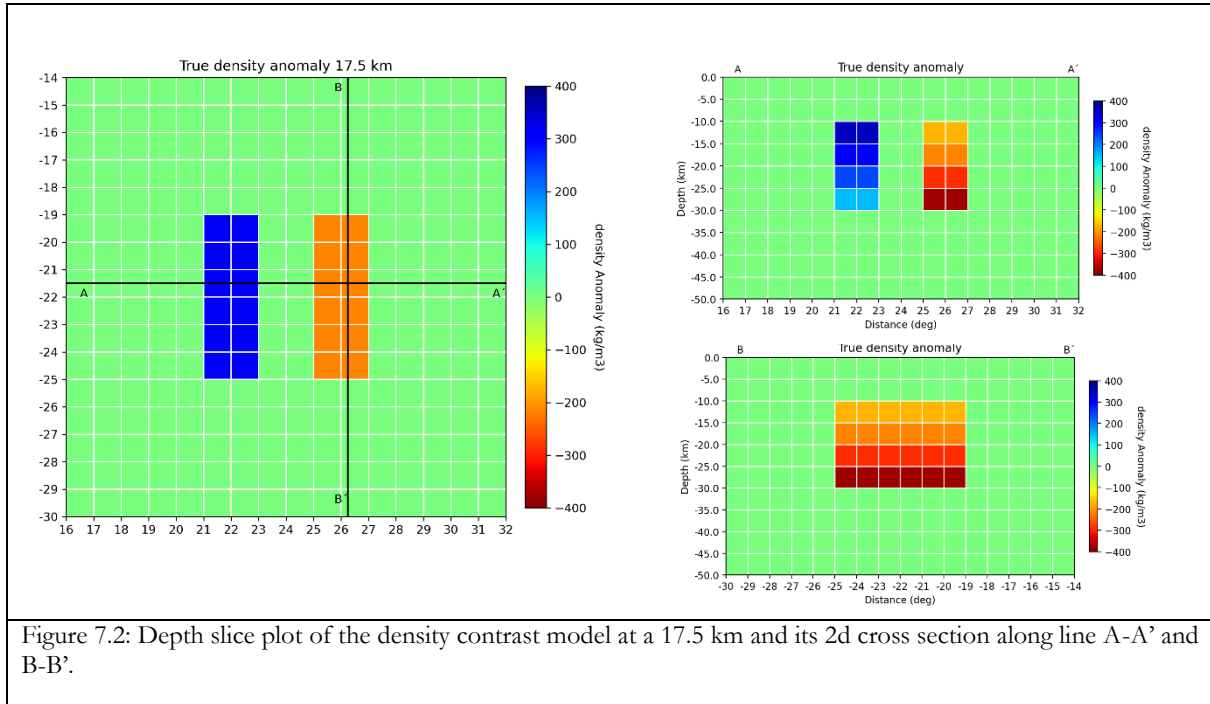


Figure 7.2: Depth slice plot of the density contrast model at a 17.5 km and its 2d cross section along line A-A' and B-B'.

### 1.3. Inversion parameters

Table 7.1 shows the inversion parameters used during the first phase of synthetic method test using a simple geologic model. Each inversion scenario has its own parameters adjusted based the different types of data integration.

Table 7.1: Parameters used during the first phase of synthetic method test.

Summary of the data weighting and model regularization parameters used during the different inversion scenarios					
inversion scenarios	Data used for the inversions	parameters			
		Variables	data weight	damping weight	smoothness weight
Scenario 1: Gravity data only inversion	gz	gz	0.050	0.2	0.1, 0.1, 0.1
	gz + gzz	gz	0.050	0.2	0.1, 0.1, 0.1
		gzz	0.020		
	gall (gzz + gxx + gyy + gxy + gxz + gyz)	gxx	0.080	0.2	0.1, 0.1, 0.1
		gyy	0.020		
		gxy	0.050		
		gxz	0.030		
		gyz	0.035		
		gzz	0.080		
	gz + gall	gz	0.050	0.2	0.1, 0.1, 0.1
		gzz	0.080		
		gxx	0.020		
		gyy	0.050		
		gxy	0.030		
gxz		0.035			
gyz		0.080			
Scenario 2: Surface-wave data only inversion	sw (group + phase)	grp	0.250	0.5	0.1, 0.1, 0.1
		phs	0.250		
Scenario 3: Joint inversion of gravity and Surface-wave data	sw + gz	grp	0.200	0.5	0.1, 0.1, 0.1
		phs	0.200		
		gz	2.000		
	sw + gz + gall	grp	0.250	0.5	0.2, 0.2, 0.2
		phs	0.250		
		gz	0.250		
		gxx	0.250		
		gyy	0.250		
		gxy	0.250		
gyz		0.250			

JOINT INVERSION OF SATELLITE GRAVITY AND SEISMIC SURFACE WAVE DATA: A SYNTHETIC TEST AND ITS APPLICATION FOR BOTSWANA CRUST AND UPPER  
MOST MANTLE VELOCITY AND DENSITY MODELING

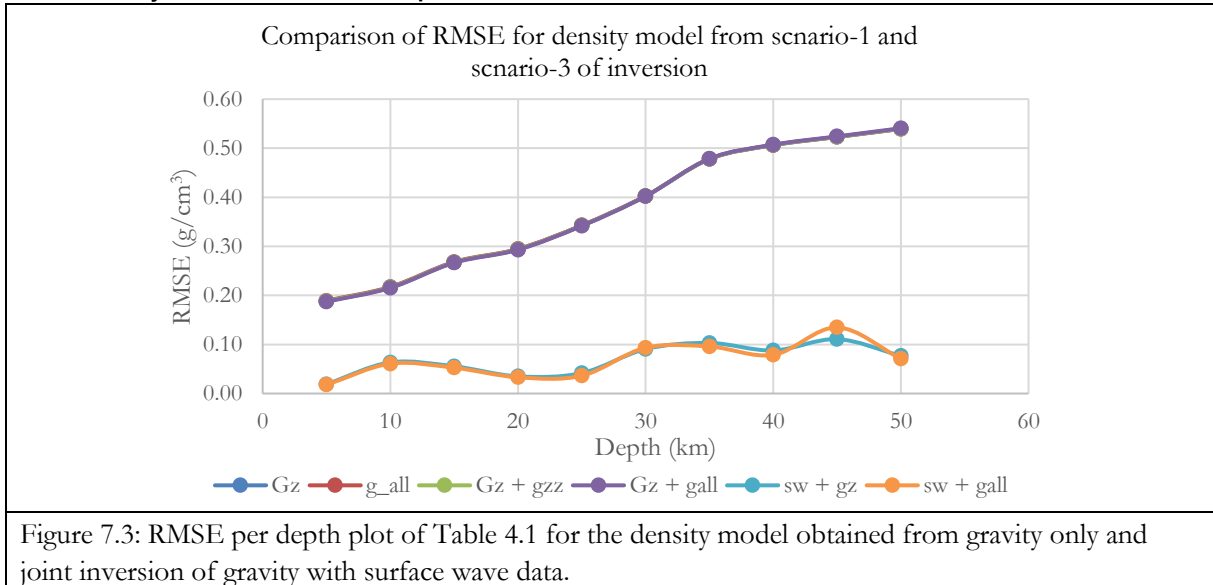
		gzz	0.250		
--	--	-----	-------	--	--

## 1.4. Misfit plot

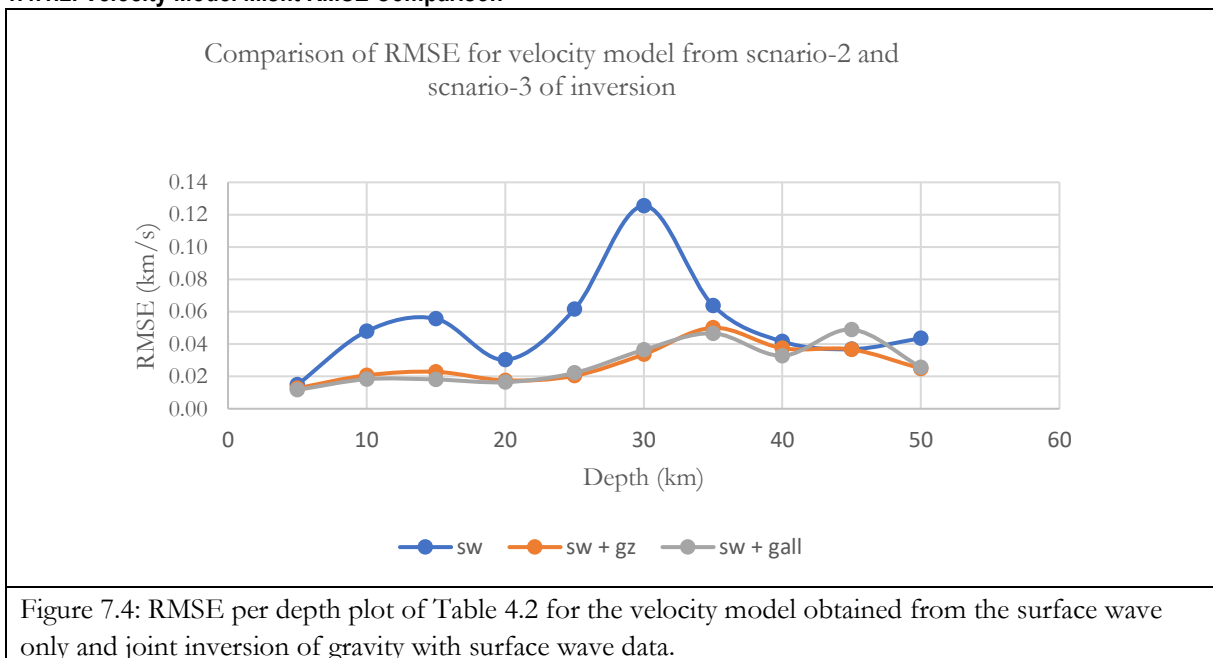
### 1.4.1. Model Misfit

RMSE of the recovered velocity and density model misfit obtained from the different inversion scenarios are presented below.

#### 1.4.1.1. Density model misfit RMSE comparison



#### 1.4.1.2. Velocity Model Misfit RMSE Comparison



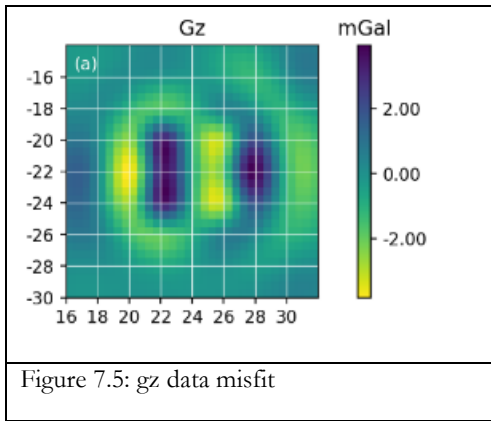
### 1.4.2. Data Misfit

The data misfit plot obtained from the first phase of method test using a synthetic data. The data misfit from the different scenario of data inversion that includes gravity-only inversion, surface-wave data only inversion and joint inversion of gravity and surface wave data.

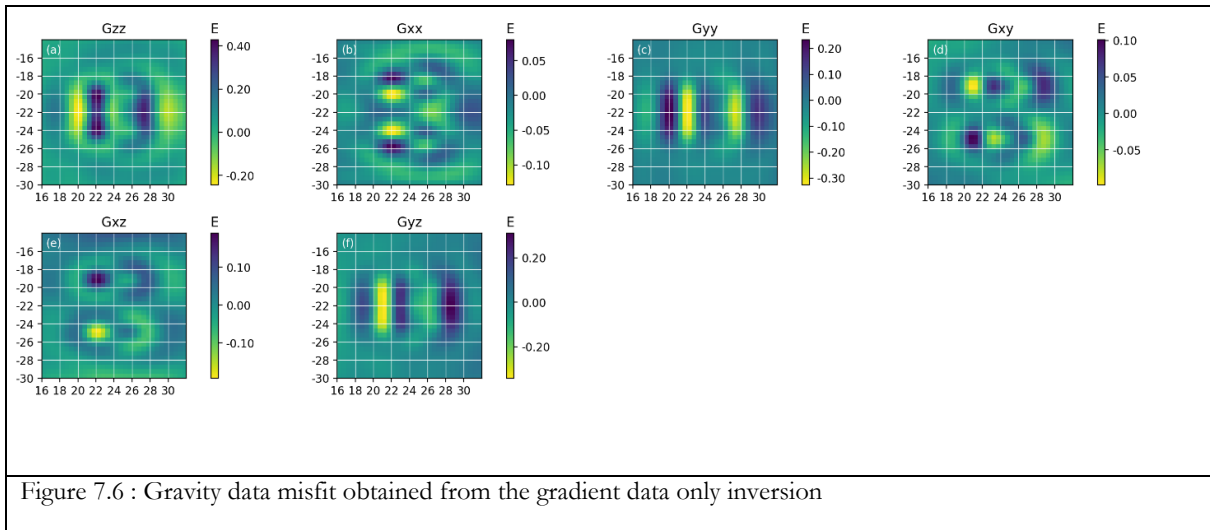
#### 1.4.2.1. Scenario-1: Gravity-only inversion data misfit

The misfit plots shown below are the gravity data misfit for the gravity only inversion for density modelling. The misfit is obtained after subtracting the observed data from the calculated data of the model response after the inversion.

#### $g_z$ only data inversion data misfit



#### $g_{all}$ inversion data misfit



$g_z + g_{zz}$  inversion data misfit

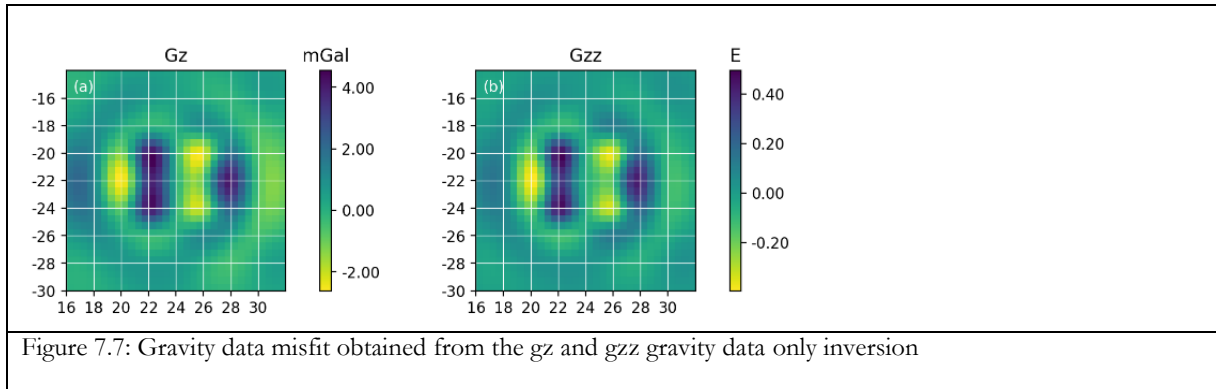


Figure 7.7: Gravity data misfit obtained from the  $g_z$  and  $g_{zz}$  gravity data only inversion

$g_z + g_{all}$  inversion misfit

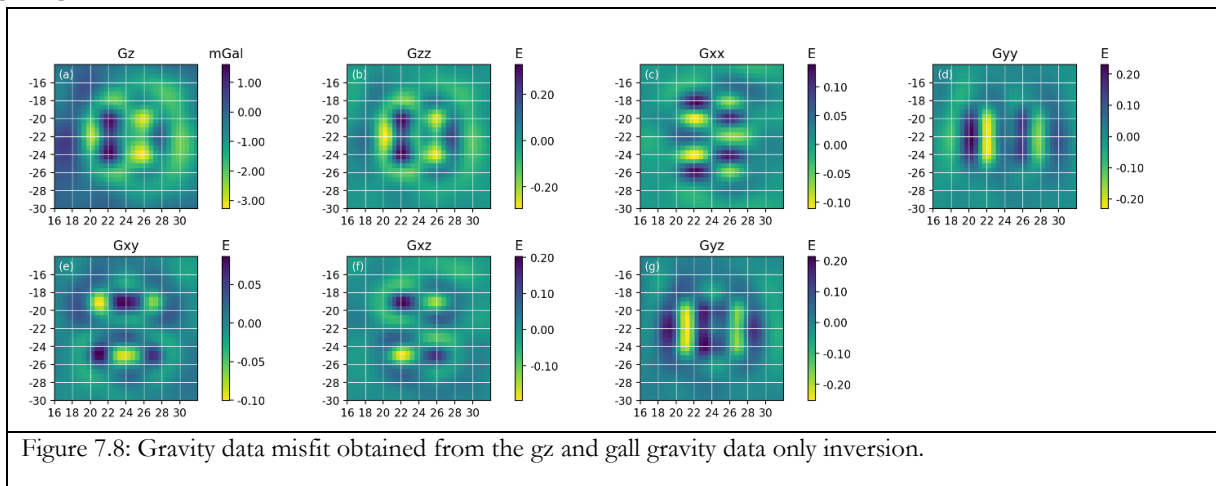


Figure 7.8: Gravity data misfit obtained from the  $g_z$  and  $g_{all}$  gravity data only inversion.

1.4.2.2. Scenario-2: surface wave only inversion data misfit

The plot shown below is the misfit plot for the group and phase velocity dispersion data obtained from scenario-2 (surface wave only inversion) for velocity modelling.

Group and Phase velocity misfit from surface wave only inversion

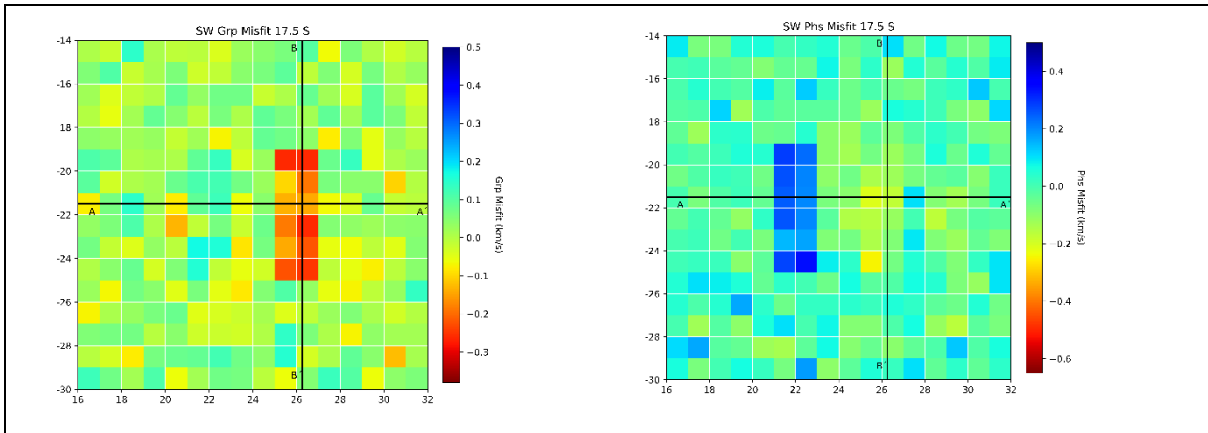


Figure 7.9: Rayleigh wave group and phase velocity data misfit obtained from cenario-2 of surface wave only inversion.

1.4.2.3. Scenario-3: Joint inversion of gravity and surface wave data

Data misfit obtained dafter the joint inversion of gravity and surface wave data.

$g_z$  + sw (group and phase velocity) inversion

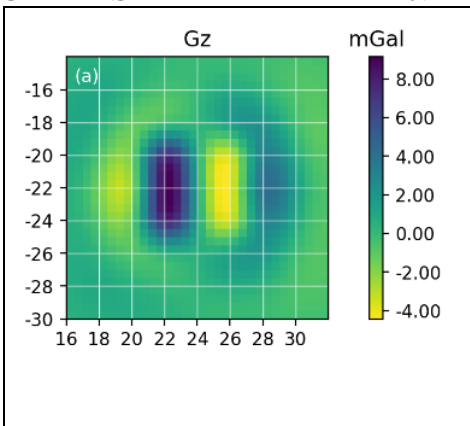


Figure 7.10: The gravity field data ( $g_z$ ) misfit after the joint inversion with the surface wave data.

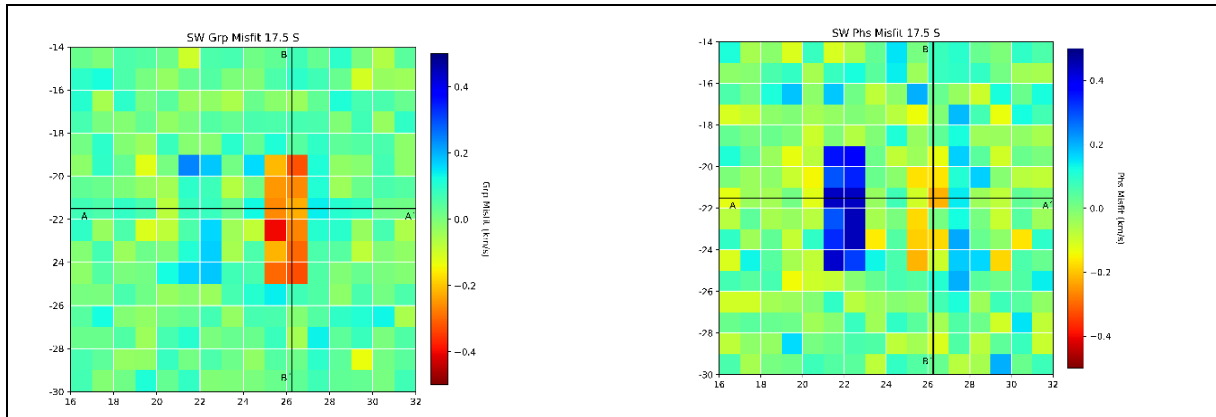


Figure 7.11: The fundamental mode Rayleigh wave group and phase velocity misfit after the joint inversion with the gravity field data only.

### Gall + sw (group and phase velocity) inversion

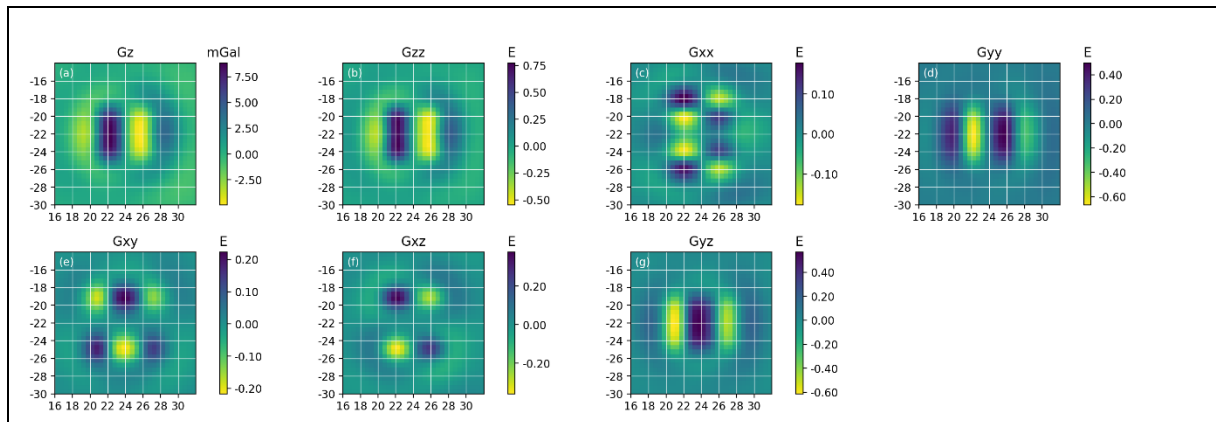
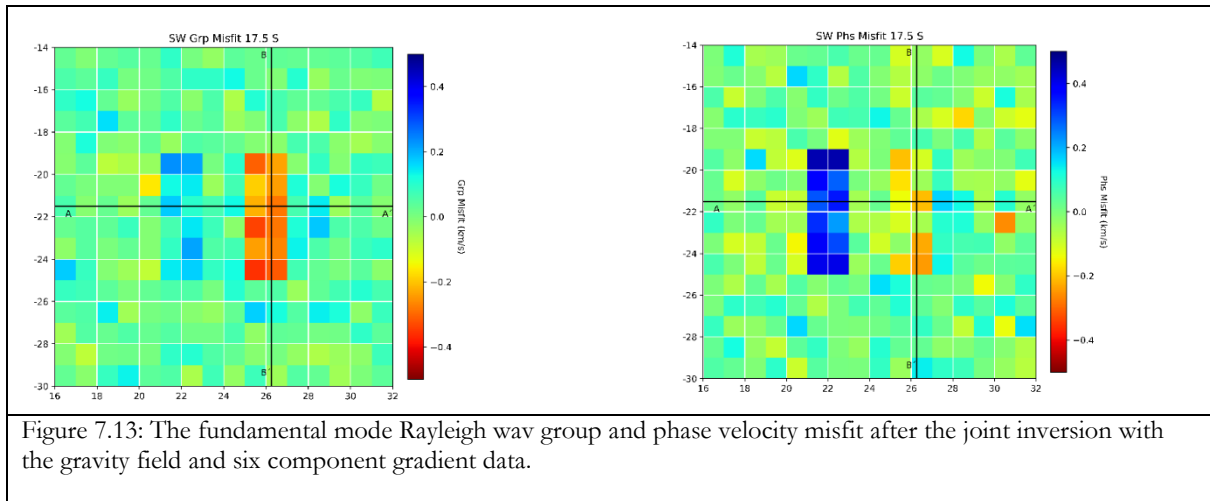


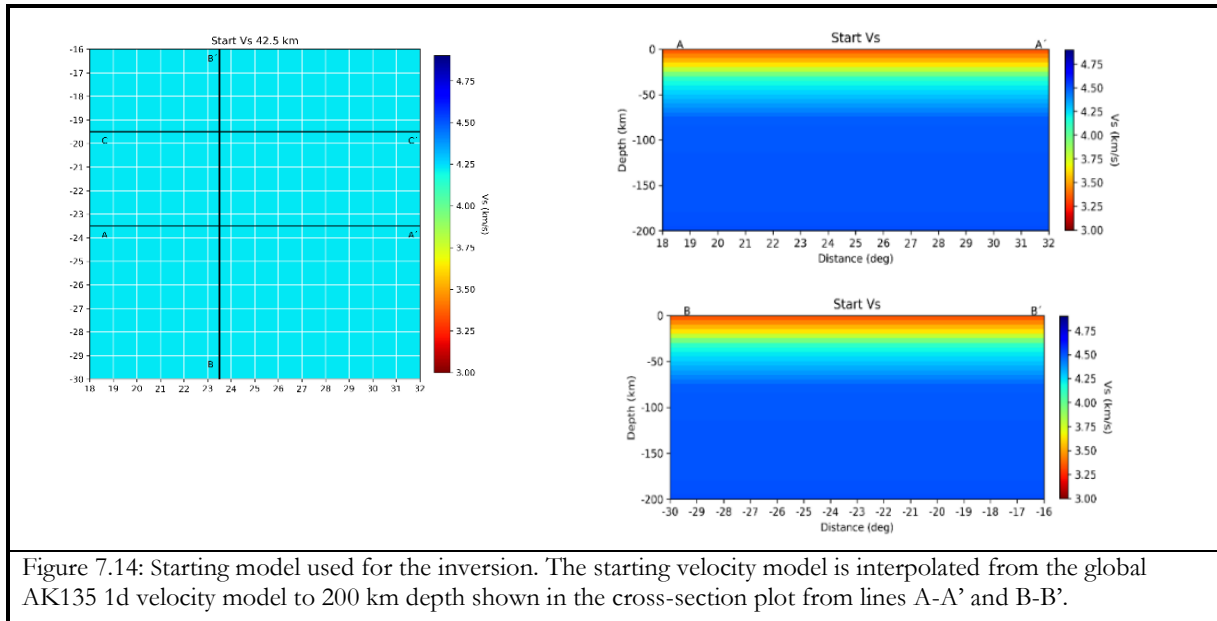
Figure 7.12: The gravity data (gravity field and six component of gradient data) misfit after jointly inverted with the surface wave data (group and phase velocity data).

JOINT INVERSION OF SATELLITE GRAVITY AND SEISMIC SURFACE WAVE DATA: A SYNTHETIC TEST AND ITS APPLICATION FOR BOTSWANA CRUST AND UPPER MOST MANTLE VELOCITY AND DENSITY MODELING



## Appendix-2: Second phase of method test that mimics Botswana geology

### 2.1. starting model for the second phase of method test



2.2. The density contrast model obtained expressed in Kg/m<sup>3</sup> that was used for the forward modelling of the gravity signal

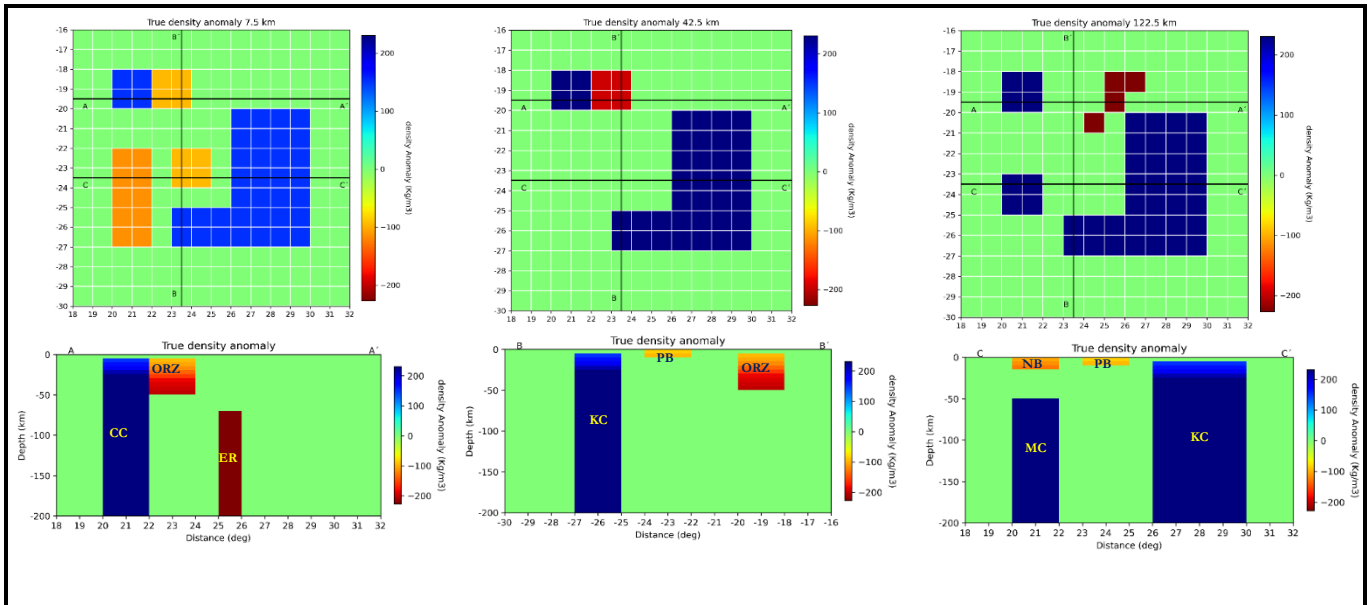


Figure 7.15: 3D true density contrast model (expressed in kg/m<sup>3</sup>). Top panel, the depth slice plot at different depths of 7.5, 42.5, and 122.5 km. The bottom panel is the cross-section plot obtained using the profile lines A-A', B-B', and C-C'. The different geological units such as the Nosope and Passarge sedimentary basin (NB & PB), buried Maltahohe micro-craton (MC), Congo craton (CC), the Kalahari craton (KC), the Okavango rift zone (ORZ), and the East African Rift system (ER), are depicted as a homogeneous block from the background values.

### 2.3. Inversion parameters

Table 7.2: Parameters used during the second phase of complex synthetic method test.

Phase 2: complex model synthetic test of the method					
Summary of the data weighting and model regularization parameters used during the different inversion scenarios					
inversion scenarios	Data used for the inversions	parameters			
		Variables	data weight	damping weight	smoothness weight
Scenario 1: Gravity data only inversion	gz + gall	gz	2.00	0.25	0.01, 0.01, 0.01
		gxx	0.08		
		gyy	0.02		
		gxy	0.05		
		gxz	0.03		
		gyz	0.04		
		gzz	0.08		
Scenario 2: Surface-wave data only inversion	sw (group + phase)	grp	0.15	0.25	0.02, 0.02, 0.02
		phs	0.15		
Scenario 3: Joint inversion of gravity and Surface-wave data	sw + gz + gall	grp	0.10	0.25	0.1, 0.1, 0.2
		phs	0.10		
		gz	2.00		
		gxx	0.08		
		gyy	0.02		
		gxy	0.05		
		gxz	0.03		
		gyz	0.04		
		gzz	0.08		

### 2.3. Misfit plot

The misfit plot obtained from the second phase of method test using a synthetic data. The data misfit from the different scenario of data inversion that includes scenario-1: gravity-only inversion, scenario-2: surface-wave data only inversion and scenario-3: joint inversion of gravity and surface wave data.

2.3.1. Scenario-1: Gravity only inversion misfit (gz + gall inversion):

JOINT INVERSION OF SATELLITE GRAVITY AND SEISMIC SURFACE WAVE DATA: A SYNTHETIC TEST AND ITS APPLICATION FOR BOTSWANA CRUST AND UPPER MOST MANTLE VELOCITY AND DENSITY MODELING

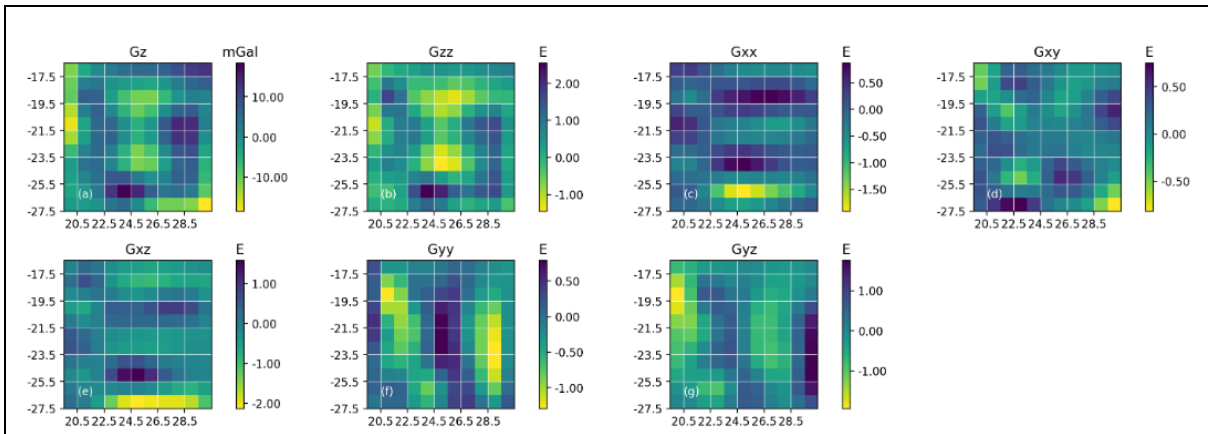


Figure 7.16: Gravity data misfit obtained from the gz and gall gravity data only inversion.

2.3.2. Scenario-2: surface wave only inversion misfit: sw (grp + phs) velocity inversion)

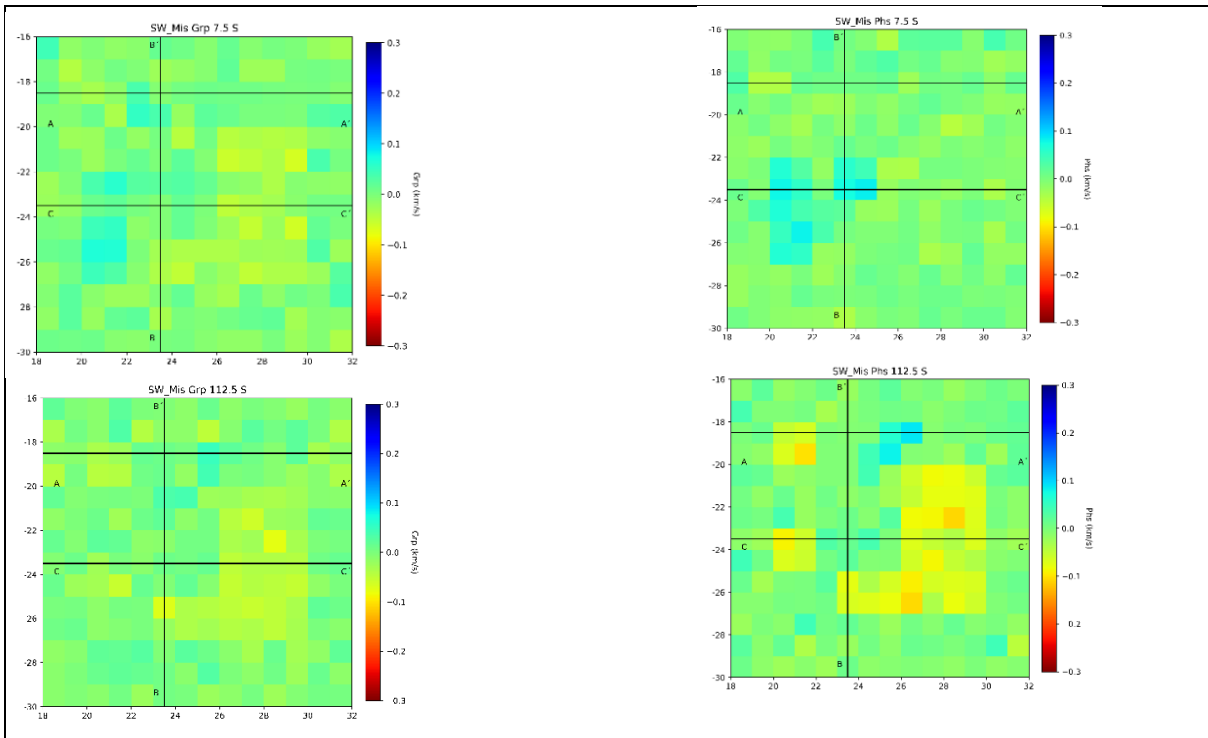


Figure 7.17: The fundamental mode Rayleigh wave group and phase velocity misfit after the joint inversion with the gravity field and six component gradient data.

2.3.3. Joint inversion of gravity and surface wave misfit (gz + gall + sw)

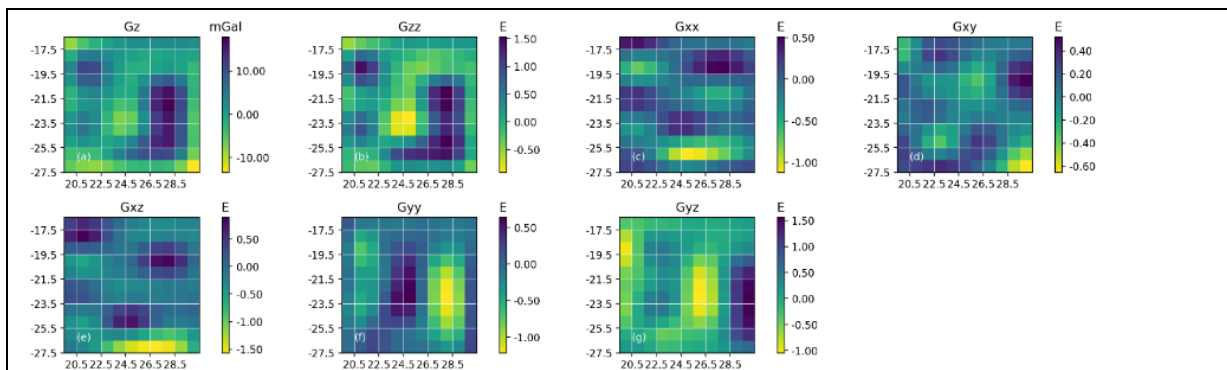


Figure 7.18: The gravity data (gravity field and six component of gradient data) misfit after jointly inverted with the surface wave data (group and phase velocity data).

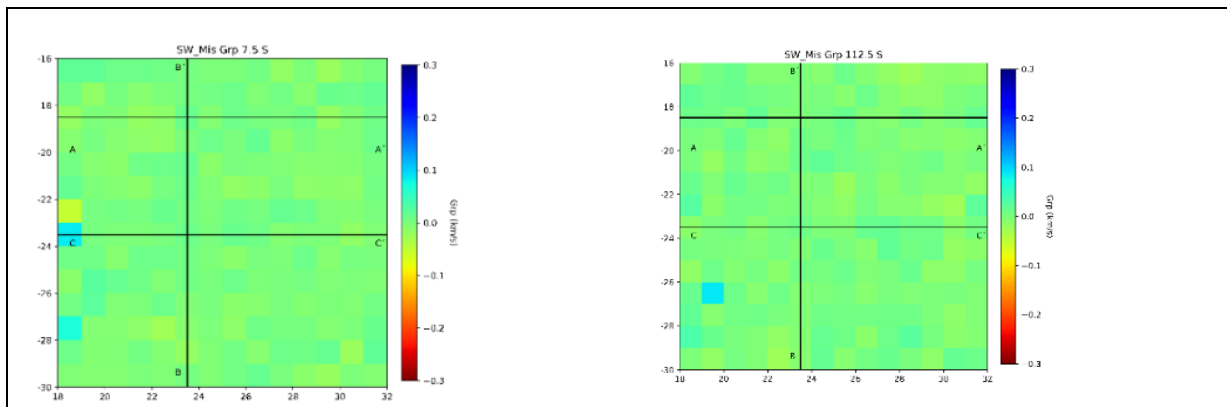


Figure 7.19: The group and phase velocity dispersion velocity misfit plot after jointly inverted with the gravity field and six component gradient data.

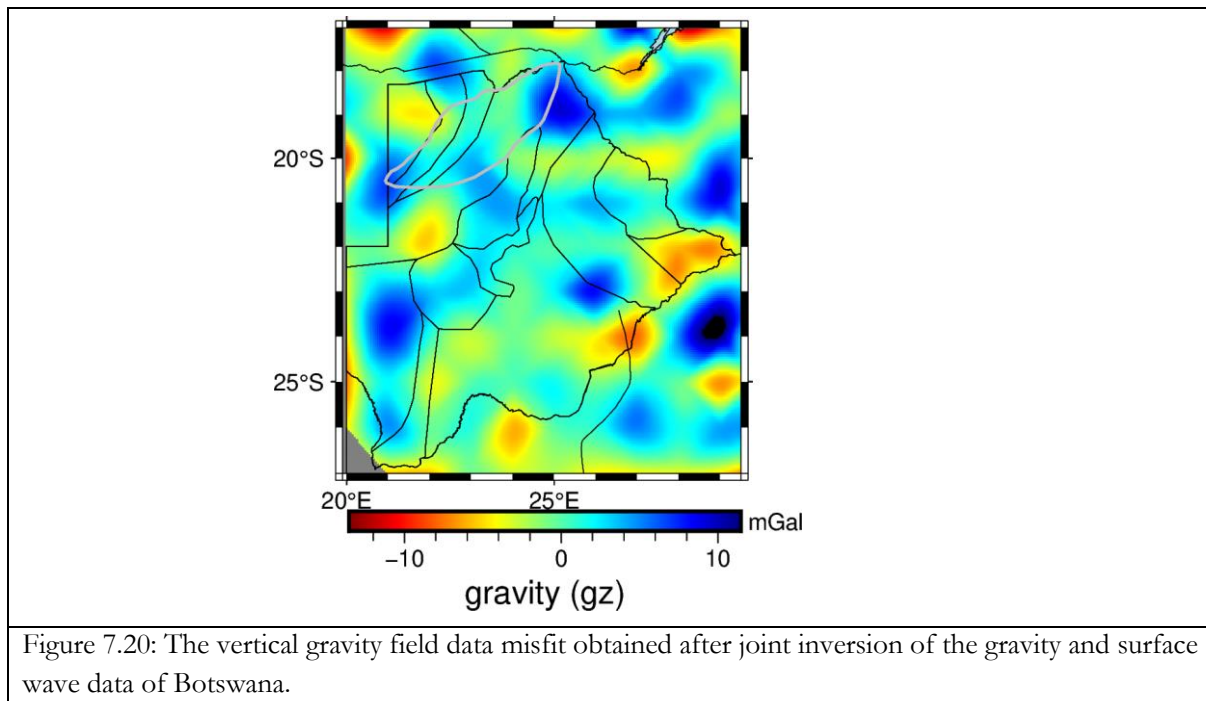
**Appendix-3:** Real data application of the joint inversion approach

3.1. Inversion parameters

Table 7.3: Inversion parameters used for the real data application.

Real data inversion	Data used for the inversions	parameters			
		Variables	data weight	damping weight	smoothness weight
Joint inversion of gravity and Surface-wave data	sw + gz + gall	grp	0.08	0.2	0.1, 0.1, 0.2
		pht	0.09		
		gz	1.30		
		gxx	0.04		
		gyy	0.02		
		gxy	0.03		
		gxz	0.03		
		gyz	0.09		
		gzz	0.06		

3.2. Data misfit plot



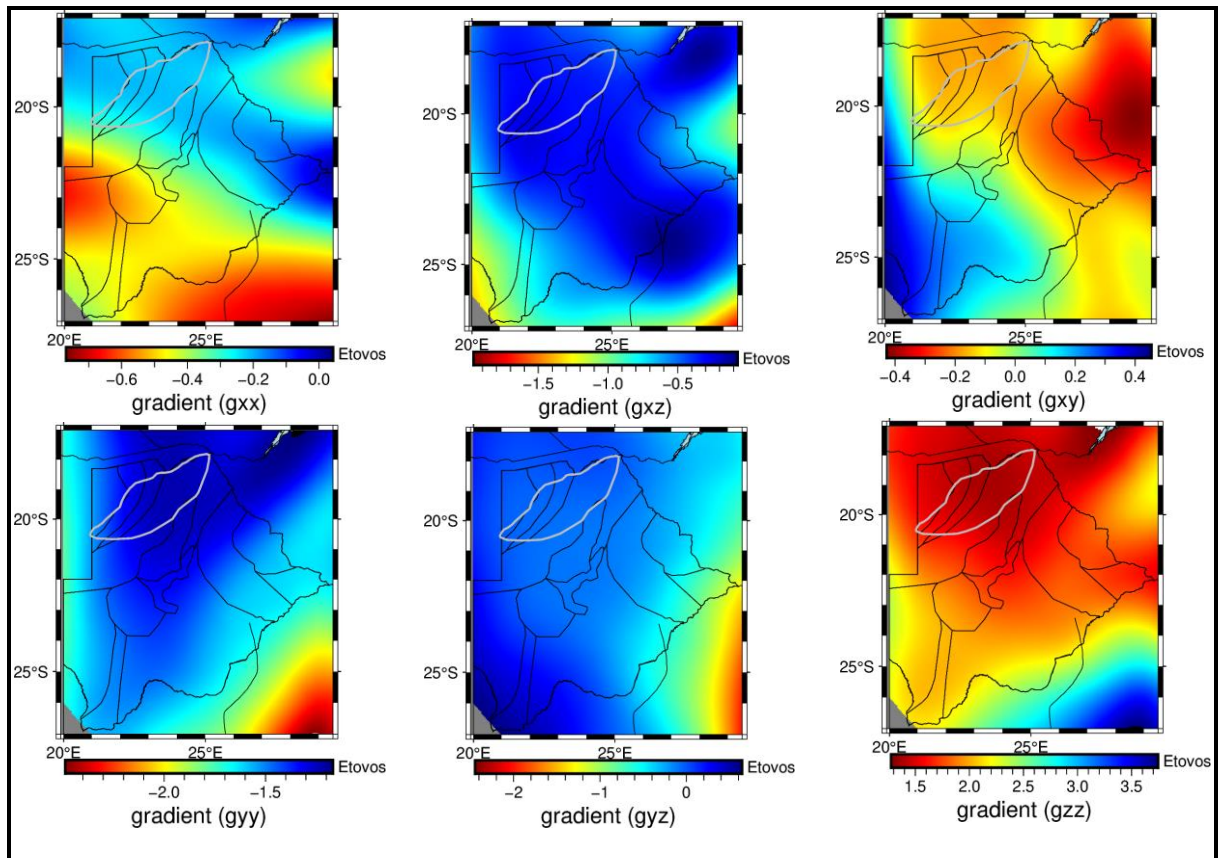


Figure 7.21: The data misfit plot for the six-component gravity gradient data obtained after joint inversion of the gravity and surface wave data of Botswana.

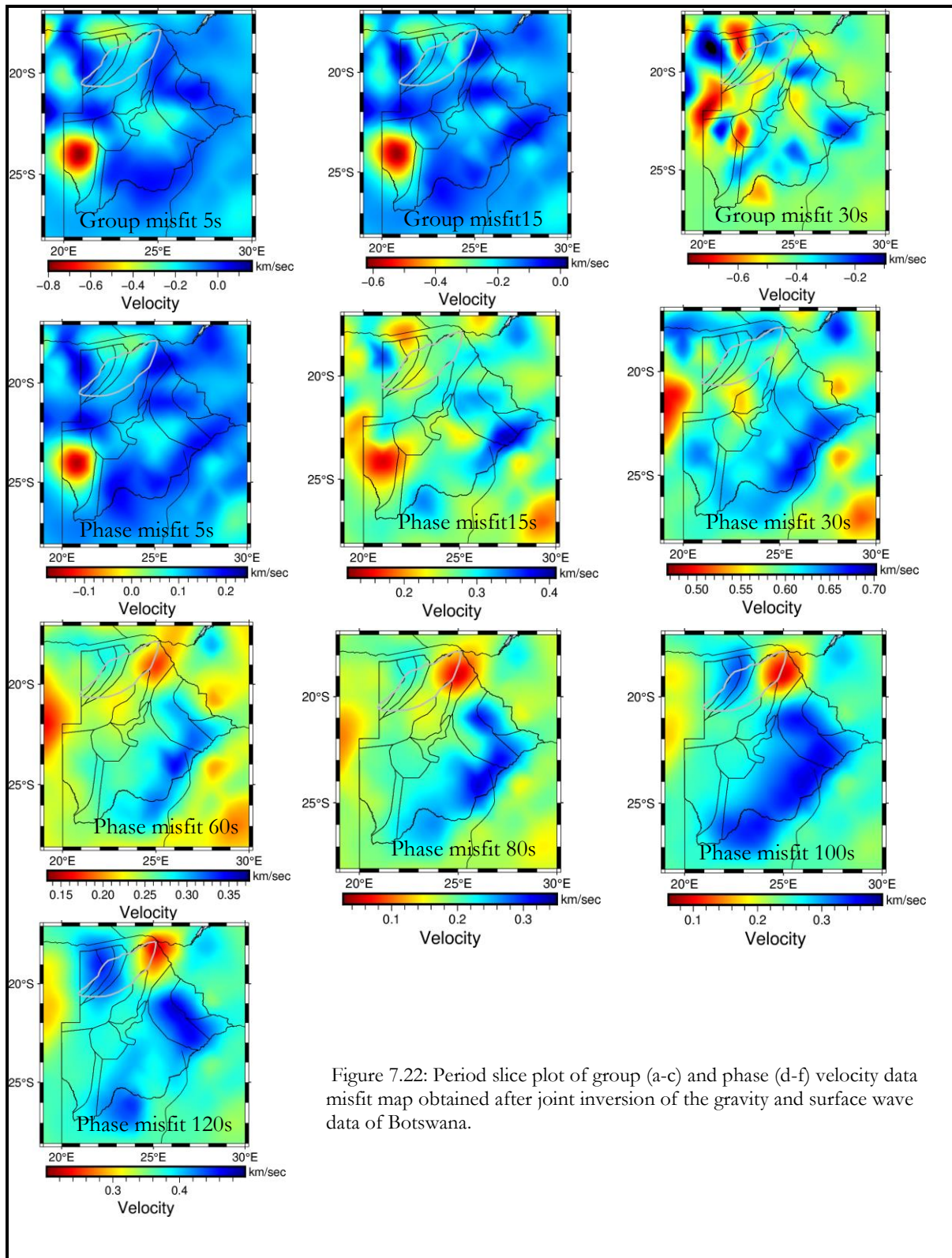


Figure 7.22: Period slice plot of group (a-c) and phase (d-f) velocity data misfit map obtained after joint inversion of the gravity and surface wave data of Botswana.

